



Strål  
säkerhets  
myndigheten

Swedish Radiation Safety Authority

Authors:

Tobias Backers  
Tobias Meier  
Peter Gipper  
Ove Stephansson

Technical Note

2015:30

Rock Mechanics - Assessing the likelihood and extent of fracture growth in the KBS-3 repository at Forsmark  
Main Review Phase



## SSM perspektiv

### Bakgrund

Strålsäkerhetsmyndigheten (SSM) granskar Svensk Kärnbränslehantering AB:s (SKB) ansökningar enligt lagen (1984:3) om kärnteknisk verksamhet om uppförande, innehav och drift av ett slutförvar för använt kärnbränsle och av en inkapslingsanläggning. Som en del i granskningen ger SSM konsulter uppdrag för att inhämta information och göra expertbedömningar i avgränsade frågor. I SSM:s Technical Note-serie rapporteras resultaten från dessa konsultuppdrag.

### Projektets syfte

Det övergripande syftet med projektet är att ta fram synpunkter på SKB:s säkerhetsanalys SR-Site för den långsiktiga strålsäkerheten för det planerade slutförvaret i Forsmark. Projektet syftar till att kvantifiera sannolikhet och utbredning av spricktillväxt i bergmassan runt deponeringstunnlar och deponeringshåll i det planerade KBS-3 slutförvaret. Den förväntade utvecklingen av storlek, sammanlänkning, rörelser samt transmissivitet hos sprickorna i berget bedöms baserat på resultat från numerisk modellering som explicit kan ta hänsyn till sprickpropagering. Relevanta scenarier samt materialegenskaper från SR-Site används i analyserna.

### Författarnas sammanfattning

Denna rapport dokumenterar SSM:s externa experters granskning av SKB:s säkerhetsanalys SR-Site för ett slutförvar för använt kärnbränsle i Forsmark. Granskningen, som är en del i SSM:s huvudgranskningsfas, fokuserar på frågor kring sannolikhet och storlek av spricktillväxt i bergmassan kring slutförvarets deponeringstunnlar och deponeringshåll.

Spricknätverkets stabilitet och utveckling i bergmassan runt slutförvaret studeras med hänsyn till termiska, glaciala och jordskalvslaster. Syftet är att förstå och kvantifiera betydelsen av sprickutvecklingen för integriteten av slutförvarets barriärer och bergmassans hydro-mekaniska egenskaper. Rapporten behandlar inte spjälkning eller andra skademekanismer som kan uppstå i berget i närheten av deponeringshålen.

Rapporten studerar hur förändringar i bergspänningsfältet i olika scenarier påverkar stabiliteten samt utvecklingen av spricknätverket. Detta görs inledningsvis genom en analytisk utvärdering och sedan genom numerisk modellering av scenariernas konsekvenser. Resultaten från de olika angreppssätten har jämförts med slutsatsen att de stödjer varandra.

Författarna anser att dagens in-situ spänningstillstånd, som ligger till grund för alla sprickstabilitetsanalyser, har stor inflytande på analysresultaten. Det är därför viktigt att det antagna in-situ spänningstillståndet verifieras på plats eller att sensitivitetsanalyser genomförs för att bedöma hur mycket olika möjliga spänningstillstånd påverkar modellerna.

Under den termiska fasen kan sprickutveckling förväntas till följd av de termiska lasterna. Detta medför en ökning av bergmassans hydrauliska konduktivitet.

Under den glaciala fasen har tiderna med det tjockaste istäcket en stabiliserande effekt på spricknätverket. Det förväntas endast liten sprickutveckling, i jämförelse med dagens förhållanden, i samband med tider då isen smälter. Förhöjda horisontella spänningar föreligger dock i berget efter varje glacialt maximum. Den mest kritiska tidpunkten under den glaciala fasen kan förväntas i samband med utbuktningen som föregår isfronten.

En simulering av ett jordskalv med magnitud 7,0 pekar på en förhöjd risk för sprickpropagering och sammanlänkning. Ett skalv med så stor magnitud förväntas påverka spricknätverket och ge ökad sprickdensitet och hydraulisk konduktivitet.

**Projektinformation**

Kontaktperson på SSM: Flavio Lanaro

Diarienummer ramavtal: SSM2011-3630

Diarienummer avrop: SSM2013-3841

Aktivitetsnummer: 3030012-4083

## **SSM perspective**

### **Background**

The Swedish Radiation Safety Authority (SSM) reviews the Swedish Nuclear Fuel Company's (SKB) applications under the Act on Nuclear Activities (SFS 1984:3) for the construction and operation of a repository for spent nuclear fuel and for an encapsulation facility. As part of the review, SSM commissions consultants to carry out work in order to obtain information and provide expert opinion on specific issues. The results from the consultants' tasks are reported in SSM's Technical Note series.

### **Objectives of the project**

The general objective of the project is to provide review comments on SKB's post-closure safety analysis, SR-Site, for the proposed repository at Forsmark. The project concerns the evaluation of the likelihood and extent of fracture growth around the deposition tunnels and holes of the planned KBS-3 repository. The expected evolution of the size, interlink, displacements and transmissivity of the fractures should be evaluated by means of numerical modelling that can quantify fracture growth. For this purpose, relevant scenarios and material properties in SR-Site should be considered.

### **Summary by the authors**

This report documents external review work in the context of SSM's Main Review Phase of SKB's safety assessment SR-Site of the KBS-3 repository for spent nuclear fuel at Forsmark. This review work concerns the evaluation of the likelihood and extent of fracture growth around deposition tunnels and holes in the repository.

The issues of the thermal, seismic and glacial loading concerning the stability and evolution of fracture networks (DFN) in the rock around the repository are addressed. The likelihood and extent of fracture growth is analysed considering the implications for the integrity of the repository barriers and the changes of hydro-mechanical properties of the rock mass around deposition holes. This report does not address the issue of spalling and other rock failure near deposition holes and tunnels.

In this report it is examined how the changes of the rock stresses that occur during different scenarios affect the stability and the evolution of the fracture network in the target volume of the planned repository. Thereby, an analytical evaluation precedes the detailed numerical simulation of the different scenarios. The results of both approaches are compared and found to support each other.

It was found that the present-day in-situ stress regime, which builds the base for all analyses of fracture stability, has a significant influence on the results. It is therefore vital to either verify the current model of the in-situ stress field or to conduct the sensitivity analyses for different stress models.

During the phase of thermally induced stresses, fracture propagation can be expected. This implies that an increase of hydraulic connectivity might occur.

During the glacial cycle, the stages of maximum thickness of an ice sheet above the repository have a stabilising effect on the fracture network. Compared to the present-day stress conditions, slightly increased fracture propagation would take place when the ice cover is removed but horizontal stresses are still elevated, after the glacial maxima. The most critical state of stress during glaciation with respect to fracture growth evokes from a glacial forebulge.

During a simulated earthquake of magnitude 7.0, elevated potential for fracture propagation and coalescence was identified. It can be expected that a seismic event of this magnitude initiated on a deformation zone of the Forsmark tectonic lens affects the fracture network, increasing fracture density and hydraulic connectivity.

**Project information**

Contact person SSM: Flavio Lanaro

**Authors:** Tobias Backers, Tobias Meier, Peter Gipper, Ove Stephansson  
Geomecon GmbH, Potsdam, Germany

## Technical Note 81

# 2015:30

Rock Mechanics - Assessing the likelihood and extent of fracture growth in the KBS-3 repository at Forsmark  
Main Review Phase

This report was commissioned by the Swedish Radiation Safety Authority (SSM). The conclusions and viewpoints presented in the report are those of the author(s) and do not necessarily coincide with those of SSM.

# Contents

<b>1. Introduction .....</b>	<b>3</b>
1.1. Comment on the nomenclature for faults and fractures used by SKB .....	3
1.2. Comments on criteria for judgment of the fracture and fault stability .....	4
<b>2. Stability of the structural inventory at Forsmark .....</b>	<b>7</b>
2.1. SKB's presentation of the stability of the structural inventory .....	7
2.1.1. Summary of the stress fields .....	7
2.1.2. Discrete fracture networks .....	7
2.1.3. SKB's assessment of the stability at present-day .....	8
2.1.4. SKB's assessment of the stability during the thermal phase .....	8
2.1.5. SKB's assessment of the stability during the glacial phase .....	11
2.2. Independent analyses of the stability of fracture sets in this study .....	13
2.2.1. Motivation of the assessment .....	13
2.2.2. Analyses of the stability of fracture sets .....	14
2.3. The Consultants' assessment on the stability of fracture sets .....	20
<b>3. Influence of thermal loading on fracture growth .....</b>	<b>23</b>
3.1. SKB's presentation of fracture growth .....	23
3.2. Independent modelling of the influence of thermal loading on fracture growth .....	24
3.2.1. Motivation of the assessment .....	24
3.2.2. Modelling setup .....	24
3.2.3. Results from simulation of increased stresses due to thermal loading .....	25
3.3. The Consultants' assessment on the influence of thermal loading on fracture growth .....	31
<b>4. Influence of the glacial cycle on fracture growth .....</b>	<b>33</b>
4.1. SKB's presentation of fracture growth .....	33
4.2. Independent analyses on the influence of the glacial cycle on fracture growth .....	33
4.2.1. Motivation of the assessment .....	33
4.2.2. Modelling setup .....	34
4.2.3. Results of modelling of a glacial cycle .....	34
4.3. The Consultants' assessment on the influence of the glacial cycle on fracture growth .....	44
<b>5. Influence of time dependent fracture growth .....</b>	<b>47</b>
5.1. SKB's presentation of time dependent fracture growth .....	47
5.2. The Consultants' assessment of time dependent fracture growth .....	47
5.2.1. Motivation of the analyses of time dependent deformation fracture growth .....	47
5.2.2. Discussion of the time dependent fracture growth .....	48
5.3. The Consultants' assessment on time dependent fracture growth .....	50
<b>6. Influence of an earthquake on fracture growth .....</b>	<b>53</b>
6.1. SKB's presentation .....	53

6.2. The consultants' assessment of the influence of an earthquake on fracture growth .....	54
6.2.1. Motivation of the assessment .....	54
6.2.2. Analyses.....	54
6.2.3. Magnitude 7.0 earthquake .....	57
6.2.4. Magnitude 6.0 proximal earthquake .....	66
6.2.5. Magnitude 6.0 distal earthquake .....	67
6.2.6. Analysis of fault jump potential .....	68
6.3. The Consultants' assessment of the influence of an earthquake on fracture growth .....	71
<b>7. The Consultants' overall assessment on the likelihood and extent of fracture growth in the KBS-3 repository at Forsmark.....</b>	<b>73</b>
<b>8. References.....</b>	<b>77</b>
<b>Appendix 1 Coverage of SKB reports .....</b>	<b>81</b>
<b>Appendix 2 Description of the Discrete Fracture Network used in this study .....</b>	<b>83</b>
<b>Appendix 3 Discrete fracture network realisations .....</b>	<b>101</b>
<b>Appendix 4 Numerical approach and models .....</b>	<b>117</b>
A4.1 The fracture network evolution simulator roxol™ .....	118
A4.2. Geomechanical models.....	119
A4.3 Numerical model .....	119
A4.5 Confirmation of the stability of the DFNs at present .....	120
A4.6 Results of roxol simulations .....	120
A4.7 References .....	121
<b>Appendix 5 Numerical results .....</b>	<b>123</b>
A5.1 Results of the thermal analyses .....	123
A5.2 Results of the thermal analyses with increased $K_{IIC}$ . ....	124
A5.3 Results of the thermal analyses with deposition holes. ....	125
A5.4 Results of the analyses of glaciation stage T1. ....	126
A5.5 Results of the analyses of glaciation stage T2. ....	127
A5.6 Results of the analyses of glaciation stage T3. ....	128
A5.7 Results of the analyses of glaciation stage T4. ....	129
A5.8 Results of the analyses of glaciation stage T5. ....	130
A5.9 Results of the analyses of earthquake scenario with magnitude M6. ....	131
A5.10 Results of the analyses of earthquake scenario with magnitude M7. ....	132
A5.11 Results of the analyses of fault jump. ....	133

# 1. Introduction

This report documents external review work in the context of SSM's Main Review Phase for SKB's safety assessment SR-Site. This review work concerns the evaluation of the likelihood and extent of fracture growth around the deposition tunnels and holes of the planned KBS-3 repository at Forsmark (see Appendix 1). However, the issue of spalling and similar rock failure is not considered.

The issues of the isostatic, shear and thermal loading concerning the stability and evolution of rock fractures around the KBS-3 repository at Forsmark are addressed. Hereby, the thermal, glacial and earthquake scenarios are considered. The likelihood and extent of fracture growth is analysed considering the implications for the size of the fractures intercepting the deposition holes, the integrity of the repository barriers and the changes of hydro-mechanical properties of the rock.

In a previous study the response of the Discrete Fracture Network (DFN) to the typical loading history of a set of deposition holes in a repository was simulated by Backers and Stephansson (2011) using Fracod2D, which is a fracture mechanics code. The study showed that the fracture network is potentially subjected to fracture growth during selected phases of the stress changes in the history of a repository. The amount of fracture growth depends on the in situ stress model assumed, but evidence was also found that significant fracture extension may be expected for increased fluid pressures during glacial periods. The previous study used a generic fracture network with few fractures (less than 15) and was only aiming at showing the potential of fracture extension and connection to the deposition holes on small scale models.

In the study at hand, the impact of different loading scenarios on realizations of fracture networks was evaluated. The fracture networks were generated by an independent SSM consultant assignment using the SKB statistical data (Min et al., 2013). The size of the analysed models is about 50×50 m, hence much larger than previous analyses. The analyses were performed using a fracture mechanics based code called roxol as a main tool to analyse the potential of extension of the DFN.

## 1.1. Comment on the nomenclature for faults and fractures used by SKB

In general the term *fault* is used to refer to a deterministically identified deformation zone that is defined as a geological structure along which there is a concentration of deformation, as opposed to the term *fracture*, which is used to refer to small scale joints and discontinuities exhibiting small or no deformations that are statistically modelled as fracture sets within specific rock volumes (e.g. deformation zones, ZFM, or fracture domains, FFM).

The term *fault* is not clearly defined in any of the reviewed SKB reports. However, Stephens et al. (2007, SKB R-07-45) define the term *fault zone* as a brittle deformation zone with known shear sense of movement. A brittle deformation zone without known shear sense is termed *fracture zone*. Table 1.1 shows a set of definitions

provided by Stephens et al. (2007, SKB R-07-45) that follow the nomenclature described in Munier and Hermansson (2001, SKB R-01-15) and Munier et al. (2003, SKB R-03-07). The definition of brittle structures is based on Andersson et al. (2000, SKB R-00-15).

Table 1.1. Terminology and geometrical description of brittle structures in the bed-rock based on Andersson et al. (2000, SKB R-00-15).

Terminology	Length	Width	Geometrical description
Regional deformation zone	> 10 km	> 100 m	Deterministic
Local major deformation zone	1 km - 10 km	5 m - 100 m	Deterministic (with scale-dependent description of uncertainty)
Local minor deformation zone	10 m - 1 km	0.1 m - 5 m	Stochastic DFN (if possible, deterministic)
Fracture	< 10 m	< 0.1 m	Stochastic DFN

This terminology however is not consistently used through SKB's publications. For example Lund et al. (2009, SKB TR-09-15) use the terms *fracture*, *fracture zone* and *fault zone* as synonymous for deformation zones. In Hökmark et al. (2010, SKB TR-10-23) the terminology seems largely consistent with Stephens et al. (2007, SKB R-07-45), however, fracture of length up to 300 m are considered, not following the above terminology (Table 1.1). Fälth et al. (2010) use the term *fault* for discontinuities potentially generating an earthquake, and the term *fracture* for receivers and potentially slipping planes ("target fractures") in response to seismic movements on faults, also not following the terminology by Stephens et al. (2007, SKB R-07-45).

In this report we will use the terms *fault* for deterministically identified deformation zones (i.e. zones that are named ZFM) and *fracture* or *crack* for statistically modelled fractures and deformation zones. This definition should be independent of any scale, but deterministic deformation zones are naturally larger.

## 1.2. Comments on criteria for judgment of the fracture and fault stability

The assessment of stability of brittle discontinuities is carried out by SKB with the same analytical method irrespective of the scale. The basic approach transfers the Mohr-Coulomb brittle failure criterion to instability indicators like the Coulomb Failure Stress (*CFS*; e.g. Lund et al., 2009, SKB TR-09-15; Fälth et al., 2010, SKB TR-08-11), Factor of Safety (*FoS*; Hökmark et al., 2010, SKB TR-10-23) or reactivation potential (*rp*, this report). The informative value of these criteria is the same. The assumption about the strength of the discontinuity of interest, which is the resistance to slip in this context, is crucial. There are abundant mostly laboratory derived values of friction angles for fractures, sealed fractures, fracture domains and even deformation zones. The instability quantities *CFS* and *FoS* solely depend on the choice of this parameter, as they normalise the ratio of shear and normal stress

on the plane of interest to the assumed critical value for shearing. In this respect, the reactivation potential as used in the context of the present study has the advantage of not being normalised to a specific friction angle. However, the disadvantage of using the reactivation potential  $r_p$  is that it has to be compared with the assumed critical friction angle to obtain a measure of the shear stability of deformation zones and fractures.

The question whether laboratory derived strength parameters are valid for field application is beyond the scope of this report. It also needs to be emphasised that SKB mostly does not actually touch the topic of fault or fracture extension due to failure of the rock but rather assesses the stability and quantifies the amount of slip on pre-existing discontinuity planes. Most of the models employed by SKB assume linear elasticity and cannot describe inelastic deformation.



## 2. Stability of the structural inventory at Forsmark

### 2.1. SKB's presentation of the stability of the structural inventory

#### 2.1.1. Summary of the stress fields

For the repository depth, several stress models have been put forward by SKB. The available stress models are summarised in Table 2.1. SKB's main<sup>1</sup> site stress model was developed by Martin (2007, SKB R-07-26) and is largely based on overcoring stress measurements. It corresponds to a reverse faulting regime at all depths in the repository volume and beyond, down to 600 m depth. Another model is based on hydraulic testing methods and results in a strike-slip faulting regime at repository depth (Ask et al., 2007, SKB P-07-206). A review of the stress data and measurement methods by Backers et al. (2014, SSM Technical Note 2014:10) yielded a new interpretation of the in situ stresses resulting in a transitional faulting regime at repository depth, from reverse to strike-slip conditions.

Table 2.1. Stress models and related stress magnitudes at repository depth (500 m) for Forsmark. SH is the maximum horizontal stress, Sh is the minimum horizontal stress, Sv is the vertical stress and Pp is the pore pressure.

SH [MPa]	Sh [MPa]	Sv [MPa]	PP [MPa]	References
41.0 ± 6.2	23.2 ± 4.6	13.3 ± 0.3	5	Martin 2007 (R-07-26)
22.7 ± 1.1	10.2 ± 1.6	13.3	5	Ask et al. 2007 (P-07-206)
35.5 ± 5	13.3 ± 2	13.3	5	geomecon (Backers et al. 2014, SSM Technical Note 2014:10)

#### 2.1.2. Discrete fracture networks

The discrete fracture networks in the different fracture domains have been statistically modelled by Fox et al. (2007, SKB R-07-46) on the basis of outcrop mapping and cored boreholes in the Forsmark area. Fracture sets with the same orientation are identified and characterized by dip direction and dip angle of the mean pole, and a set of other parameters for size, intensity and concentration that describe how the fracture pole vectors cluster around the mean pole (Table 2.2). The fracture sets are divided in global sets, which were mapped in (nearly) every outcrop, and local sets, which represent highly localized stress environments (Fox et al., 2007, SKB R-07-46, Tables 4-15 to 4-22).

---

<sup>1</sup> SKB is referring to it as “most likely” and using this model in most analyses.

### 2.1.3. SKB's assessment of the stability at present-day

Hökmark et al. (2010, SKB TR-10-23) evaluate the effects of elevated stresses during a thermal phase and a glacial cycle using a combination of numerical tools (3DEC code) and analytical solutions. For the stability analysis under present-day stress conditions, they apply SKB's in-situ stress model (Martin, 2007, SKB R-07-26, cf. Table 2.1). Hökmark et al. (2010) also use the factor of safety (*FoS*) for the stability evaluation, which is a parameter defined as the ratio of shear strength and shear stress (SKB TR-10-23, page 73):

$$FoS = \frac{c + \mu \sigma_n}{\tau} \quad \text{Eq. (2.1)}$$

where  $c$  is the cohesion,  $\sigma_n$  is the normal stress,  $\mu$  is the coefficient of friction and  $\tau$  is the shear stress, respectively. For the present-day conditions, using a friction angle of  $35.8^\circ$  ( $\mu = 0.72$ ) and a cohesion of 0.5 MPa for the fractures in FFM01, the stability by means of the *FoS* is shown in a pole plot (Figure 2.1; top right). Shallow dipping fracture orientations show *FoS* less than one, hence, they could exhibit slip, particularly those trending ENE.

Table 2.2. Fracture sets in different fracture domains at Forsmark (Fox et al., 2007, SKB R-07-46).

Fracture Domain	Mean poles global sets [°]		Mean poles local sets [°]	
	Trend	Plunge	Trend	Plunge
FFM01	314.9 270.1 230.1 0.8	1.3 5.3 4.6 87.3	157.5 0.4 293.8 164.0 337.9	3.1 11.9 0.0 52.6 52.9
FFM02	315.3 92.7 47.6 347.4 186.3 157.9	1.8 1.2 4.4 85.6 4.3 4.0	107.2 73.0	1.8 5.6
FFM03	311.1 270.2 42.4 348.8 196.5	2.7 6.9 2.8 81.0 7.3	164.8	1.2
FFM06	125.7 91.0 34.1 84.3	10.1 4.1 0.8 71.3	155.4 0.0	8.3 47.5

### 2.1.4. SKB's assessment of the stability during the thermal phase

The assessment is carried out for different locations in the repository with respect to the deposition areas where heat is generated (Figure 2.1, top left; SKB TR-10-23, Figures 6-24 to 6-26). For the thermal phase, SKB conclude based on the analysis of

the factor of safety that fractures with a dip less than 55° in locations peripheral to the deposition areas (i.e. between the deposition areas, scanline A, Figure 2.1; bottom right), become unstable almost irrespective of their strike, except for sub-horizontal fractures. Fractures in heated regions should not become as unstable as fractures around the deposition areas (scanline B, Figure 2.1; bottom left). Additionally, the stresses that evolve during heating of the repository are represented as Mohr circles according to the failure criterion:

$$\tau = 0.5 \text{ MPa} + \tan(35.8^\circ) \cdot \sigma_n \quad \text{Eq. (2.2)}$$

which shows potential failure at the repository level, and more stable conditions at depths below and above the repository.

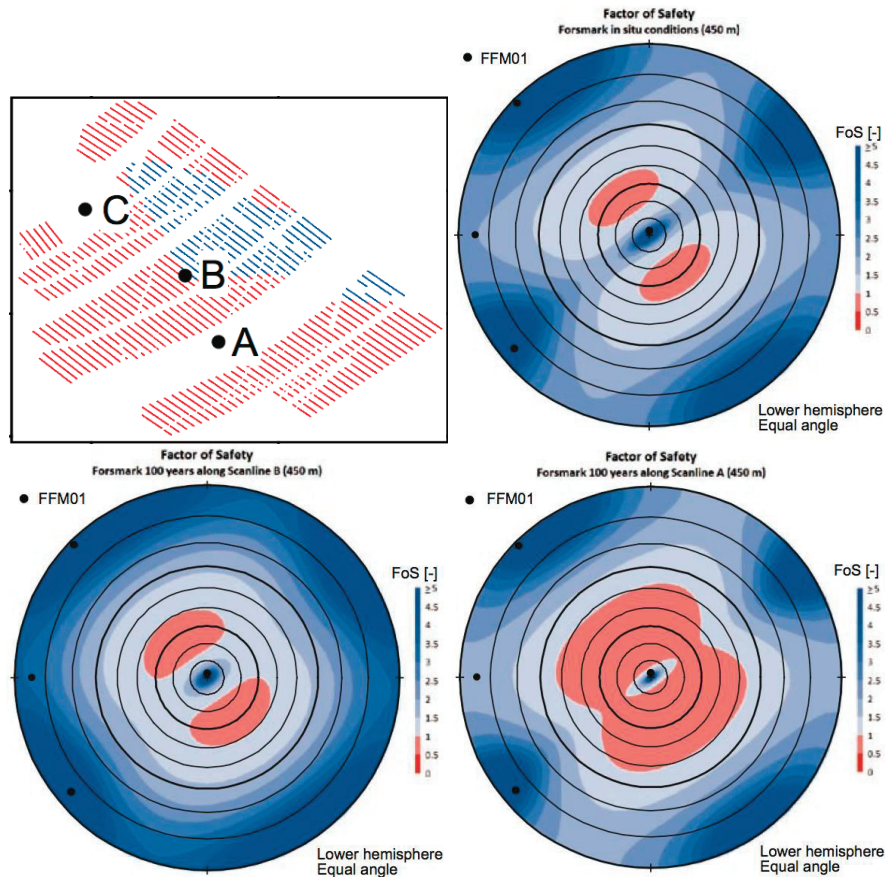


Figure 2.1. SKB's determination of the factor of safety ( $FoS$ ) for present-day conditions and during the thermal phase (from SKB TR-10-23, Figures 6-24 to 6-26). Red areas in the pole plots indicate  $FoS < 1$ . Black dots in the pole plots represent mean poles to global fracture sets in FFM01 (cf. Table 2.2). (Top left) Position of the vertical scanlines A, B and C in the repository. (Top right) Pole plot showing the factor of safety for present-day stress conditions. (Bottom left) Pole plot showing the factor of safety 100 years after canister deposition (peak temperatures) along scanline B. (Bottom right) Pole plot showing the factor of safety 100 years after canister deposition (peak temperatures) along scanline A.

Since the initial background stresses already imply shear displacements at repository depth prior to heating, the maximum displacement in excess of the displacement for present-day conditions under the given stress field is presented. According to Hökmark et al. (2010, SKB TR-10-23) the resulting maximum displacements occur after 100 years and are larger along scanline A. An optimally oriented fracture with a 300 m diameter in non-heated areas is estimated to slip about 28 mm, compared to a slip of about 6 mm in heated areas (Figure 2.2).

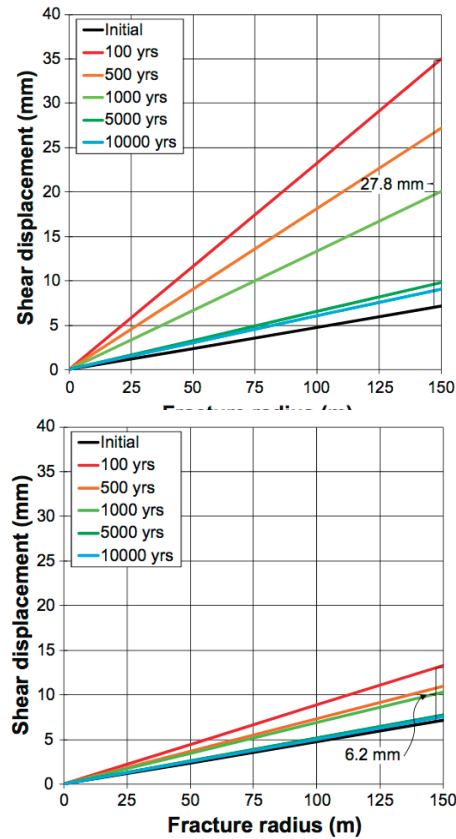


Figure 2.2. Shear displacement vs. fracture radius at 460 m depth for different time steps during the thermal phase of the repository (from SKB TR-10-23, Figures 6-27 and 6-28). (Left) non-heated region along scanline A; (Right) heated region along scanline B (see Figure 2.1 for reference).

### 2.1.5. SKB's assessment of the stability during the glacial phase

In Hökmark et al. (2010, SKB TR-10-23), the temporal evolution of the stresses induced by the ice sheet is assumed according to model MT9 by Lund et al. (2009, SKB TR-09-19), which is also adopted for analyses in this report (Figure 2.3). The pore pressure during this evolution has been modelled as fraction of the vertical load increase to be added to the hydrostatic pore pressures. Two models are evaluated by Hökmark et al. (2010, SKB TR-10-23), the first with a pore pressure equal to 98% of the glacially induced vertical load, the second with excess pore pressures as described in section 7.3.2 in Hökmark et al. (2010, SKB TR-10-23). For the glacial phase, the stability is evaluated via the resulting shear displacements on critical planes due to glacially induced stresses. Pole plots are shown, in which the maximum shear displacements for fractures with diameter of 200 m is plotted for most critical times during glacial evolution (Figure 2.5, right).

Hökmark et al. (2010, SKB TR-10-23) identify the time of a passing ice margin after the second glacial maximum as the most critical, i.e. involving the largest shear displacements (Figure 2.5, left). A fracture measuring 200 m in diameter that is optimally oriented ("most critical") would show a maximum slip at the fracture

centre of 12 mm; that is considering the second pore pressure model with excess pore pressures. The pole plot in Figure 2.5 shows the distribution of shear displacements for the most critical conditions (58 000 years and excess pore pressure). It is concluded that very few sub-horizontal fractures in fracture domains FFM01 and FFM06 would experience large shear displacements during a glacial cycle.

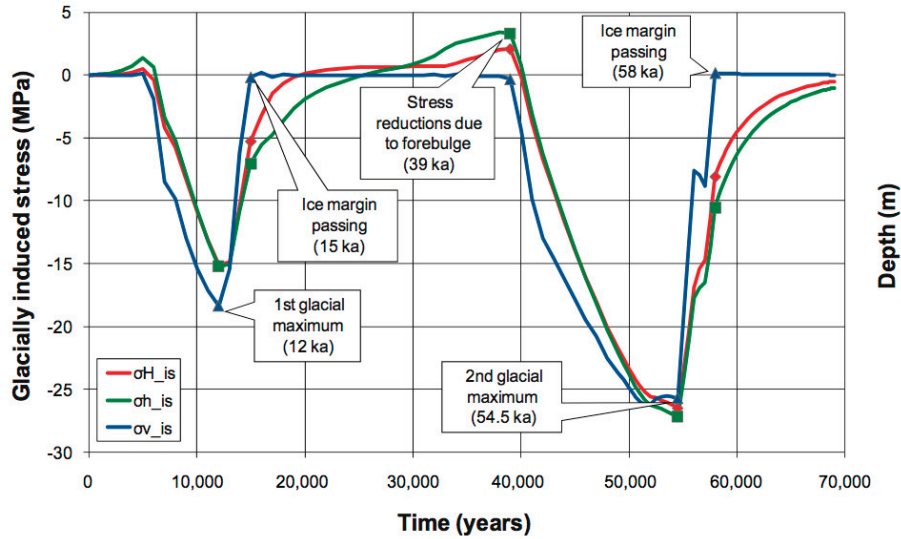


Figure 2.3. Glacially induced stress increments in the direction of present-day in situ stresses (compression is negative) as in model MT9 by Lund et al. (2009). Distinct points in time T1 to T5 are marked for further examination (from SKB TR-10-23, Figure 7-3).

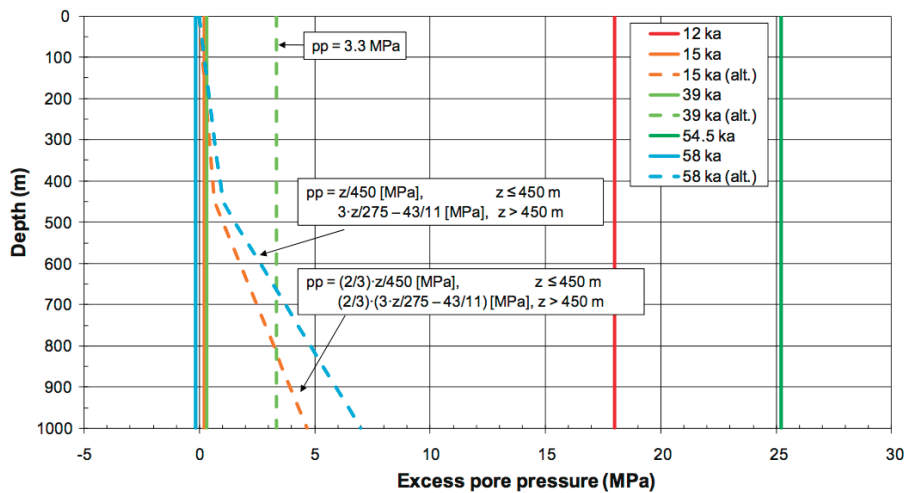


Figure 2.4. Glacially induced pore pressures as used in Hökmark et al. (2010, SKB TR-10-23). Dashed lines show the modelled excess pore pressures (from SKB TR-10-23, Figure 7-4).

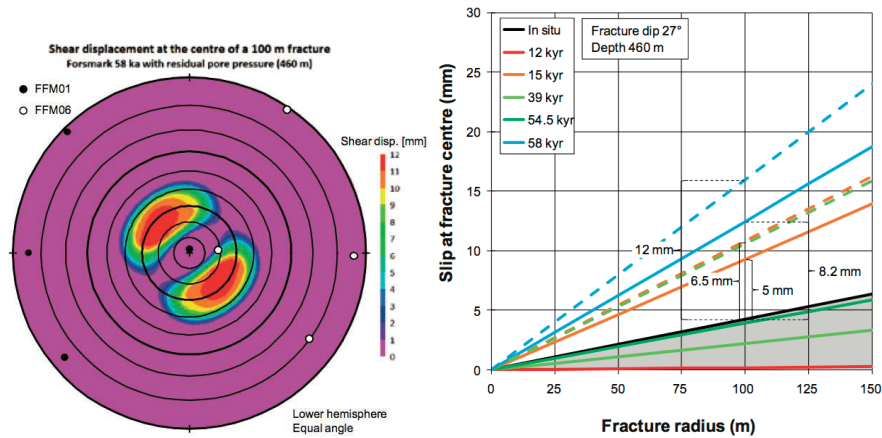


Figure 2.5. (Left) Shear displacements (in excess to displacements induced by initial in-situ stresses) after 58 000 years with excess pore pressure variant and fractures with diameter of 200 m at a depth of 460 m. (Right) Shear displacements for fractures of different radii at repository depth for selected points in time with a pore pressure equal to 98% of the ice load (solid lines) and excess pore pressures (dashed lines) (from SKB TR-10-23, Figures 7-18 and 7-19).

## 2.2. Independent analyses of the stability of fracture sets in this study

### 2.2.1. Motivation of the assessment

A good understanding of the stress field, its orientation and evolution with respect to the prominent structural features in a geological setting is a prerequisite for any geomechanical analysis. Therefore, for this consultants' assessment it is deemed necessary to:

- analyse the relevance of the stress models as developed and presented by SKB,
- present fracture stability plots to enable to identify the orientations prone to reactivation during different stages of the repository after closure.

Hökmark et al. (2010, SKB TR-10-23) only test one background stress field. For such background stress conditions, the stress magnitudes imply relatively large differential stresses on every of the considered fracture planes. According to SKB there is no change of the faulting regime during a glacial cycle. Hence, SKB does not consider all relevant stability issues and only allow for reverse faulting mechanism. There is a need to test more stress field assumptions to analyse if the initial stress field model and related faulting regime may change during the stress evolution of the repository and lead to instability in different orientations other than for the gently dipping planes.

This assessment provides a broader understanding of the mechanical behaviour of the system and serves as a starting point for further numerical analyses. In addition, the results of individual independent analyses can be discussed in the context of the geomechanical system at Forsmark.

### 2.2.2. Analyses of the stability of fracture sets

Among the stress field models at repository depth that have been summarised in section 2.1.1, the Consultants will evaluate the influence of the stress field model by Martin (2007, SKB R-07-26) and Backers et al. (2014, SSM Technical Note 2014:10) on the stability of fracture sets. The model by Ask et al. (2007, SKB P-07-206) is similar to Backers et al. (2014) regarding the assumed faulting regime.

#### Discrete fracture network

The fracture sets for the Forsmark site have been provided by Fox et al. (2007, SKB R-07-46) as summarised in Table 2.2. In the following analyses of fracture stability, the mean poles for all reported fracture sets are shown as in Figure 2.6. Note that the future repository at Forsmark is restricted to fracture domains FFM01 and FFM06.

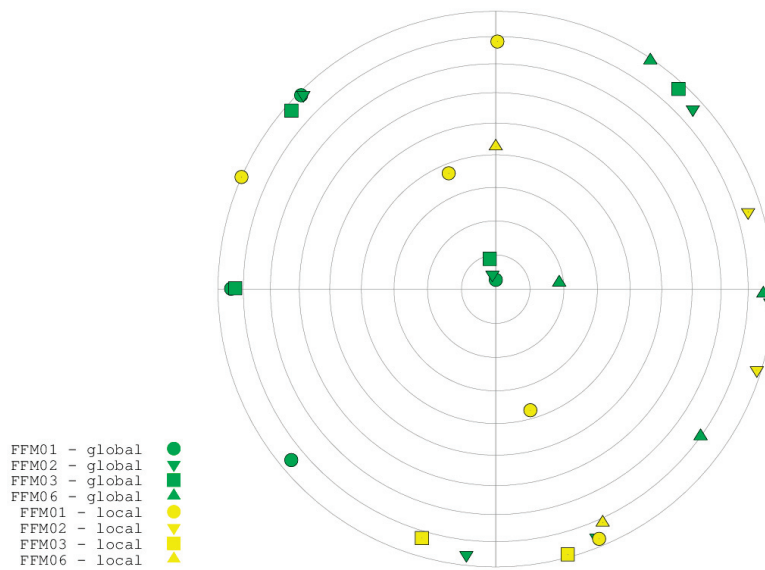


Figure 2.4. Pole plot showing the mean poles of the global and local fracture sets for fracture domains FFM01, FFM02, FFM03 and FFM06 at Forsmark in a lower hemisphere equal area plot. Grey circles denote 10° dip intervals.

#### Reactivation potential analysis

In order to evaluate stability of fracture sets with a specific frictional coefficient and orientation under a given stress field, the reactivation potential  $rp$ , which is the ratio of shear stress to normal stress acting on an arbitrarily oriented plane, is calculated.

$$rp = \frac{\tau}{\sigma_n} \quad \text{Eq. (2.3)}$$

From this relation it follows that reactivation, i.e. shear displacement along a plane, occurs when the reactivation potential exceeds the frictional strength  $\mu$ . The cohesion is thereby here neglected. This is reasonable at depth where shear stresses are much larger than the cohesion. Neglecting the cohesion in any case will lead to more

conservative estimates of the stability assessment. In the following, not only the stability at the considered present-day in-situ stresses is evaluated, but also the long-term evolution scenarios of thermal heating and glacial cycle are analysed.

In order to evaluate fracture stability we use a threshold reactivation potential of 0.72. This value corresponds to the reported friction angle of the fractures of  $35.8^\circ$  as obtained as average of the laboratory-determined peak and residual values of frictional strength (SKB TR-10-52, Table 6-60). In so doing, a fracture that is judged to be "unstable" in the following analysis means it has a reactivation potential higher than 0.72. Likewise "stable" fractures have a reactivation potential below 0.72. The general problem of scaling when obtaining strength parameters for fractures from laboratory testing reduces the significance of these test results. The analysis allows assuming other thresholds for frictional strength different than 0.72 to easily draw conclusions on the stability of the fractures.

Compared to the stability analysis by means of the Coulomb Failure Stress *CFS* (Lund et al., 2009, SKB TR-09-15; Fälvh et al., 2010, SKB TR-08-11) or the Factor of Safety *FoS* (Hökmark et al., 2010, SKB TR-10-23), the reactivation potential has basically the identical explanatory power. A maximum reactivation potential that equals the reported coefficient of friction corresponds to  $CFS = 0$  or  $FoS = 1$ . The reader should bear in mind that stress models constructed by assuming frictional equilibrium on fractures will naturally reproduce the assumed values as outcome of the maximum reactivation potential. Nevertheless those models give insight about the most critical orientations and provide information about the impact of long-term evolution under the particular stress regime.

### Fracture stability at present-day

Under present-day stress conditions with the stress model defined by SKB, the maximum reactivation potential is 0.82 (Figure 2.5) leading to instability of the fractures if a frictional strength of 0.72 is assumed. This is in accordance with the analysis by Hökmark et al. (2010, SKB TR-10-23) (cf. Figure 2.1 top right). SKB show the mean poles for the global fracture sets in FFM01, which fall all in the area of stable orientations. From Figure 2.5 it is evident that some fractures which mean pole falls into the unstable range might be subjected to shearing.

The stress model by Backers et al. (2014, SSM Technical Note 2014:10) produces a maximum reactivation potential of 0.7. This reflects the assumption for the construction of this stress field, where the most critical discontinuity planes are just at the point of frictional equilibrium with friction angle equal to 0.7. However, several fractures from both local and global sets fall into the area of potential reactivation (Figure 2.6).

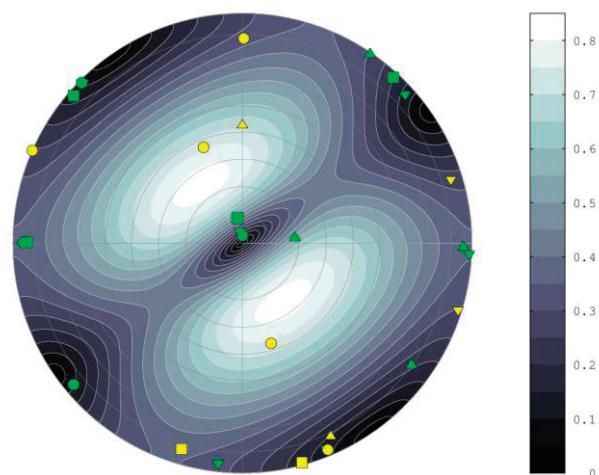


Figure 2.5. Reactivation potential at repository depth under present-day stress conditions defined by SKB's site stress model (Martin, 2009, SKB R-07-26). The maximum value of  $rp$  is 0.82.

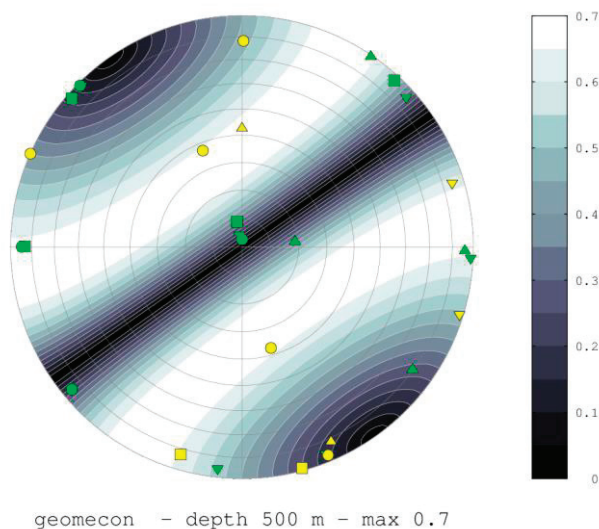


Figure 2.6. Reactivation potential at repository depth under present-day stress conditions defined by the model by Backers et al. (2014, SSM Technical Note 2014:10). The maximum value of  $rp$  is 0.7.

### Fracture stability during the thermal phase

During the thermal phase, the increase in rock temperature leads to elevated horizontal stresses while the vertical stress does not change significantly. In the reactivation potential analysis we used the addition of  $SH = +27$  MPa,  $Sh = +23$  MPa,  $SV = +3$  MPa (SKB TR-10-23, Figure 6-6; Backers et al., 2014, SSM Technical Note 2014:10). The reactivation potential for the background stress field by Martin (2007, SKB R-07-26) is significantly increased and reaches values of almost 1,

which is larger than any reported fracture frictional strength for Forsmark (Figure 2.7). This predicts that shallow dipping planes are unstable in fracture domains FFM01 and FFM06, as also reported by Hökmark et al. (2010, SKB TR-10-23) (c.f. Figure 2.1, bottom left). The sub-horizontal fracture sets mostly lie just within the stable range in the centre of the pole plot. A global fracture set in FFM06 has a mean pole that falls into the range of instability. Counting on the natural statistical scatter around the mean pole of a fracture set, even the stable oriented sub-horizontal fracture sets might contain fractures with critical orientations.

The thermal stress superposition to the background stresses defined by Backers et al. (2014, SSM Technical Note 2014:10) lead to a shift of the faulting regime towards reverse faulting and result in very similar critical orientations as for SKB's stress model as shown in Figure 2.8. The maximum reactivation potential is 0.91 and lower than for the SKB model, but still exceeding the reported frictional strength of fractures at Forsmark.

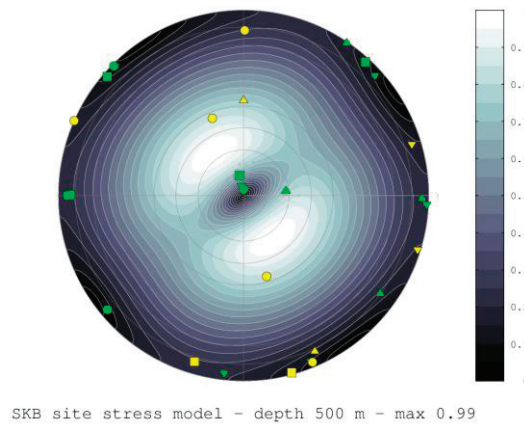


Figure 2.7: Reactivation potential at repository depth under thermally induced stresses defined by the model by Martin (2007, SKB R-07-26). The maximum value of  $rp$  is 0.99.

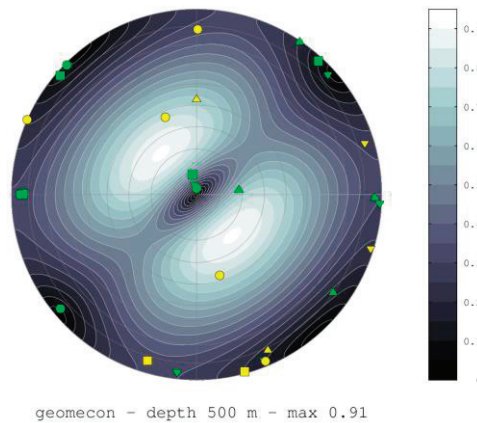


Figure 2.8. Reactivation potential at repository depth under thermally induced stresses defined by the model by Backers et al. (2014, SSM Technical Note 2014:10). The maximum value of  $rp$  is 0.91.

## Fracture stability during the glacial phase

In this section, the influence of a reference glaciation scenario on the stability of the fractures at Forsmark is examined. For this purpose the existing glaciation model by Lund et al. (2009, SKB TR-09-15) that has been discussed above is used (cf. section 2.1.3). From the evolution of the glacially induced stresses (Figure 2.3), five marked points in time, T1 through T5, are selected for stability analysis (Table 2.3). The induced pore pressure is assumed to amount to 50% of the ice load (c.f. intermediate scenario by Lund et al., 2009, SKB TR-09-15).

Figure 2.9 shows the reactivation potential for fractures under glacially induced stresses from T1 to T5 as listed in Table 2.3 and for the background stress field by Martin (2007, SKB R-07-26). It is noticeable that at the glacial maxima (T1 and T4) the glacial stresses stabilise the fractures. The maximum reactivation potential is reduced compared to present-day stresses.

During times of ice retreat (T2 and T5) the observed effect is similar to that under thermally induced stresses with reactivation potentials of 0.95 for T2 and 1.0 for T5, respectively, i.e. significantly increased potential for slip in the reverse faulting regime.

The horizontal stress reduction due to a forebulge (T3) has virtually no effect on the maximum reactivation potential since only the intermediate principal stress is affected and the maximum differential stress does not change. What can be observed, however, is that the contour lines of the unstable area are shifted; steeply dipping fracture sets that strike N-S for example, present in all global sets, show increased reactivation potentials compared to present-day, although still below the assumed critical value of 0.72.

If the background stresses according to Backers et al. (2014, SSM Technical Note 2014:10) are applied (Figure 2.10), the different glacial stages with induced stresses promote different faulting mechanisms. From an initial state of stress that implies a transitional faulting regime between reverse and strike slip faulting, the regime turns into strike-slip faulting during T1, T3, and T4, with increased reactivation potential during T3 and decreased reactivation potential during T1 and T4.

Table 2.3. Glacially induced stresses from model MT9 by Lund et al. (2009, SKB TR-09-15) at five points in time (cf. Figure 2.3).

Time		T1	T2	T3	T4	T5
Stress increments		1st glacial maximum (12 ka)	Ice margin passing (15 ka)	Stress reductions due to forebulge (39 ka)	2nd glacial maximum (54.5 ka)	Ice margin passing (58 ka)
SH	[MPa]	+16	+7.5	0	+29	+12.5
Sh	[MPa]	+14	+5	-5	+27	+9
SV	[MPa]	+18	0	0	+28	0
Pp (50% Pind)	[MPa]	+9	0	0	+14	0

During T2 and T5 with increased reactivation potential the regime shifts towards reverse faulting. The critical value of 0.72 is exceeded during T2, T3 and T5. Some gently dipping local fracture sets within FFM01 and FFM06 become unstable during T2 and T5. During T3, steeply dipping global sets in FFM06 become unstable with exception of the ones that strike NE. In FFM01, the global fracture set striking NS becomes unstable as well as other NS local sets that show a reactivation potential just at the edge of stability during T3.

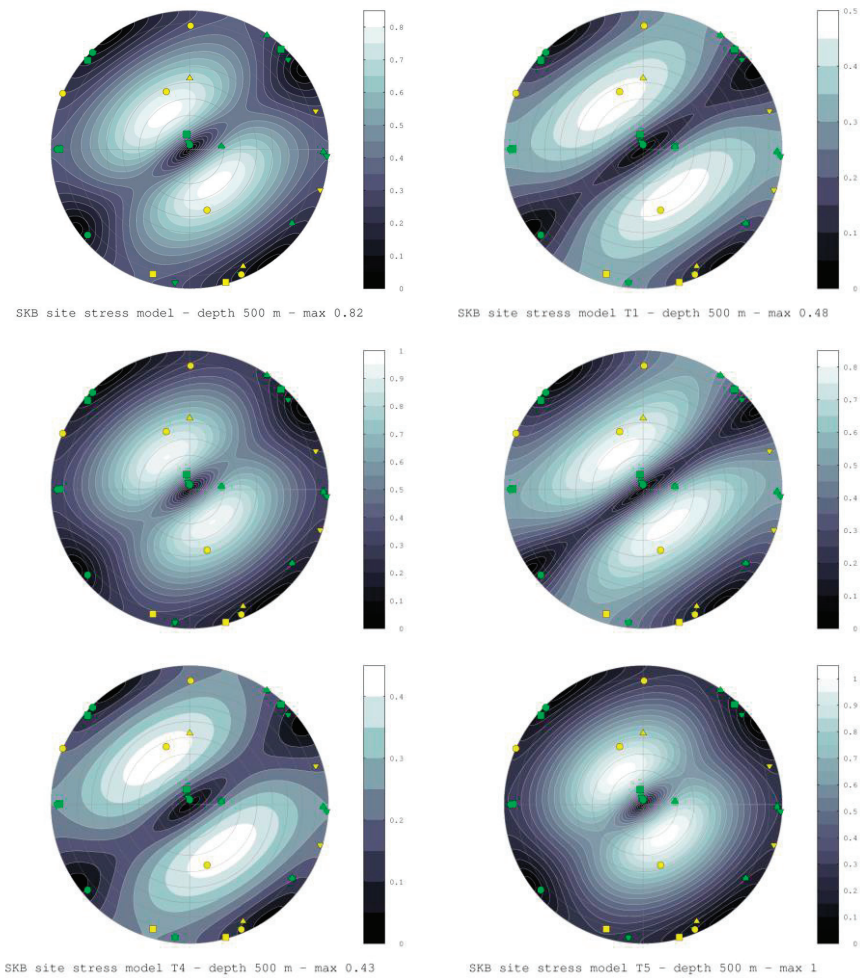


Figure 2.9. Reactivation potential at repository depth under glacially induced stresses defined by SKB's model by Martin (2007, SKB R-07-26). The maximum values of  $rp$  are: for present-day 0.82 (upper left), for T1 0.48, for T2 0.95, for T3 0.82, for T4 0.43 and for T5 1.0, respectively.

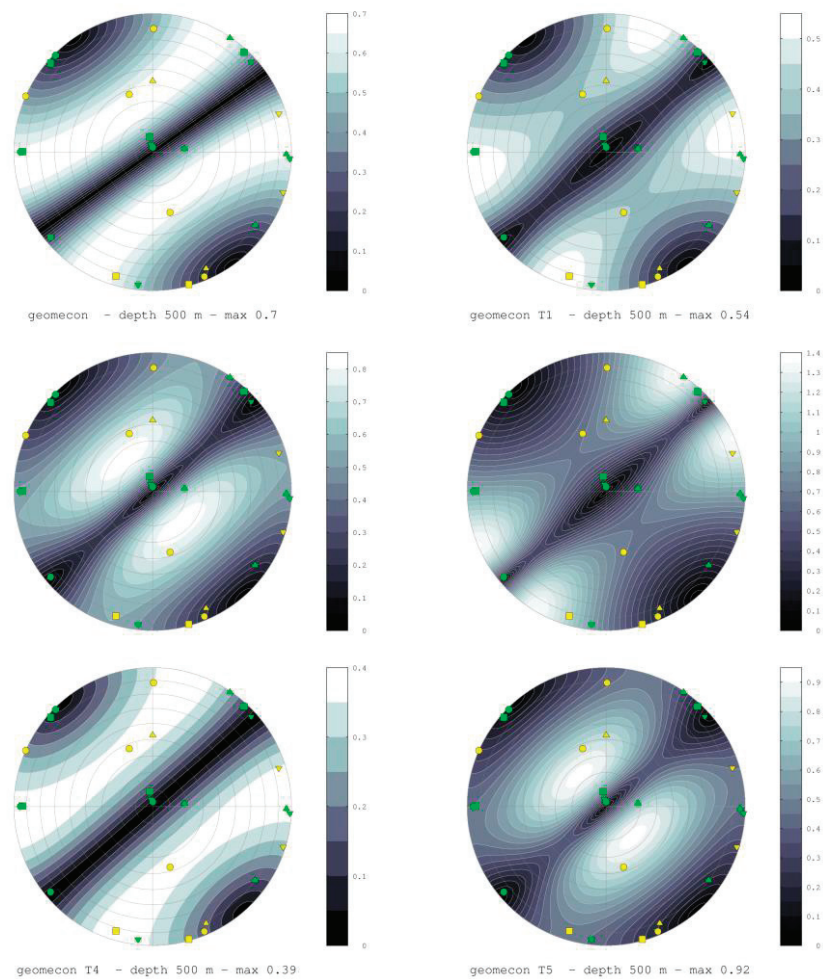


Figure 2.10. Reactivation potential at repository depth under glacially induced stresses defined by the model by Backers et al. (2014, SSM Technical Note 2014:10). The maximum values of  $rp$  are: for present-day 0.7 (upper left), for T1 0.54, for T2 0.84, for T3 1.4, for T4 0.39 and for T5 0.92, respectively.

### 2.3. The Consultants' assessment on the stability of fracture sets

The analysis on the reactivation potential for fractures cannot deliver a prediction of the occurrence of fracture propagation, but it can indicate which fractures might be subjected to slip, i.e. non-reversible shear displacement. As the critical strength parameters of the fractures are provided by SKB, some stability evaluations are possible. SKB consider only one stress field model in their analyses, i.e. the model by Martin (2007, SKB R-07-26), and select only one glacial evolution model without a broad discussion of alternatives and their implications.

In general, SKB stated that during the thermal phase shallow dipping fractures of 200 m diameter exhibit a maximum slip of 27.8 mm. During glaciation, the maximum expected slip on the same type of fracture (200 m diameter, shallow dip) is

12 mm. In both cases, slip values are in excess of the slip that is already implied with the assumed present-day stress.

The Consultants have not only considered SKB's stress model, but also used an additional model that was derived in the context of an earlier scientific assessment on spalling (Backers et al., 2014, SSM Technical Note 2014:10). The application of the alternative stress model shows some relevant implications on the results.

In the analysis of the impact of the thermal load on the stability of the fractures, the Consultants' results in general confirm SKB's results. Gently dipping fractures would exhibit slip with the assumption of SKB's temperature increase from the canisters. This is slightly more pronounced for SKB's stress model compared to the alternative stress model.

The Consultant's and SKB's analyses predict slip of the fractures with the assumption of the stress model by Martin (2007) and glaciation model MT9 by Lund et al. (2009) during times of retreating ice. With the assumption of the alternative stress model in combination with glaciation model MT9, the analysis predicts slip on fractures, not only for times of ice retreat, but also for the period of forebulge.

From this analysis, the critical fracture sets could be identified for further studies and may help to better interpret numerical simulation results in the following chapters. In addition, the stress analysis by means of the reactivation potential clearly shows that a good understanding of the stress field is essential for any mechanical understanding of the behaviour of the geological system at Forsmark. It is therefore suggested that the stress field models by SKB are critically revisited and a sound and integrated stress model for the site is developed.



### 3. Influence of thermal loading on fracture growth

#### 3.1. SKB's presentation of fracture growth

The influence of the thermal phase on fracture stability has been assessed by Hökmark et al. (2010, SKB TR-10-23). Their analysis has been discussed in the previous chapter and only the main findings are summarized here. During the peak of thermally induced stresses, the regions of the repository where most fractures can become unstable are within the unheated areas between and around the deposition panels. SKB do not carry out analyses that explicitly address fracture growth.

Fractures in heated regions can become unstable if the dip angle is between  $15^\circ$  and  $40^\circ$  in the direction of the maximum horizontal stress (Figure 3.1, left). Those fractures are predicted to slip at most about 6 mm in excess of the theoretical slip due to present-day conditions (Figure 3.1, right). This value of slip is well below the acceptable maximum displacement of 50 mm for fractures intersecting deposition holes. This is found for fractures with 300 m diameter and 100 years after canister deposition. Deposition holes should therefore not be affected by the maximum extent of fracture instability during the thermal phase.

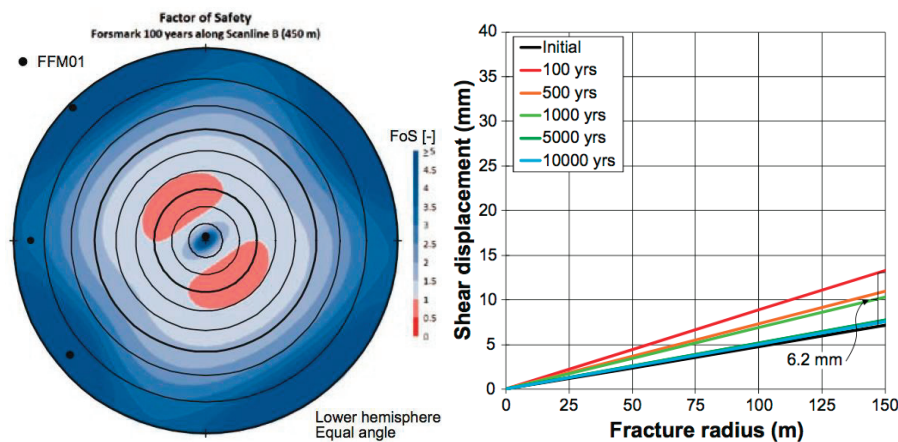


Figure 3.1. (Left) Pole plot showing the factor of safety (FoS) for planes with frictional strength  $\mu = 0.72$  under peak thermally induced stresses in heated regions of the repository (from TR-10-23, Figure 6-26). The background stress field is SKB's "most likely" stress field from (Martin 2007, SKB R-07-26). Red colours indicate  $FoS < 1$ . Black dots in the pole plots represent mean poles of the global fracture sets in FFM01 (cf. Table 2.2). (Right) Maximum shear displacement at the centre of a fracture dipping  $27.1^\circ$  versus fracture radius for different time steps according to SKB's 3DEC modelling (Hökmark et al., 2010, Figure 6-28).

## 3.2. Independent modelling of the influence of thermal loading on fracture growth

### 3.2.1. Motivation of the assessment

In existing SKB reports the mechanical response of fractures to stress changes associated with elevated temperatures in the repository are mainly evaluated in terms of elastic displacement along fractures. This is done in the light of SKB's canister damage criterion of 50 mm maximum allowed slip along a fracture intersecting a canister position. An issue that is thereby neglected is the potential growth of single fractures from its tips and associated extension of the existing fracture network.

Fracture growth is critical since it can significantly affect the integrity of the repository and harm the long-term safety. The behaviour of the DFN that represents the fracture network at the repository is therefore evaluated for the phase of thermally induced stresses in the following sections. Creation of new fractures, frequently referred to as fracture initiation, is not considered in this context, as usually it is assumed that rock mass fractures only extend. Fracture initiation is a matter of rock failure, which might be of importance for spalling and rock damage. However, in case of an existing DFN any change of boundary conditions will potentially lead to deformation on the rock mass, which in return will lead to extension of fractures, and not rock failure.

### 3.2.2. Modelling setup

The influence of thermally induced stresses on the fracture network was evaluated by the Consultants using the roxol simulation software (see Appendix A4.1 for a description of the software; [www.roxol.de](http://www.roxol.de)). The constitutive laws and employed fracture propagation criteria used, as well as the model geometry are summarised in Appendix A4.2 and A4.3. The rock mass properties are summarised in Table 3.1.

Table 3.1. Properties for the simulation of DFN extension with roxol.

Model parameters	Type / Values	References
Young's modulus	76 GPa	SKB TR-08-05 Table 7-3
Poisson's ratio	0.23	SKB TR-08-05 Table 7-3
Fracture cohesion	0.8 MPa	SKB TR-08-05 Table 7-4
Fracture friction coefficient	0.72	SKB TR-08-05 Table 7-4
Mode I fracture toughness	3.8 MPa·m <sup>1/2</sup>	Backers (2005)
Mode II fracture toughness	5.1 MPa·m <sup>1/2</sup>	Backers (2005)

Table 3.2. Present-day stresses and thermal stress increments as used in the roxol simulations.

	<b>SH</b>	<b>Sh</b>	<b>Sv</b>	<b>P<sub>p</sub></b>
	[MPa]	[MPa]	[MPa]	[MPa]
Present-day stresses (Backers et al., 2014, SSM Technical Note 2014:10)	35.5	13,3	13.3	5
Thermal stress increments (Hökmark et al., 2010, SKB TR-10-23)	27	23	3	0

The constitutive models in roxol assume fracture propagation, if a critical tensile or shear stress is exceeded at the fracture tip. This is a well-established criterion that is widely assumed to accurately apply to rocks. The code is based on an extension of the finite element method for estimating the potential for fracture extension. It is therefore capable of incorporating physically based constitutive models for any process. The input parameters to the models may be measured in the laboratory or by other methods and therefore, the input basis for roxol is reliable. As roxol uses physical models with a minimum necessity for any calibration or tuning of the parameters, we consider this a generally valid approach.

The realisations of the discrete fracture networks according to the SKB specifications provided by J. Geier (see Appendix 2) and reported in Min et al. (2013)(see also Appendix 3) were customised for the use within roxol as described in Appendix A4.3. The realisations are presented as 2D cross sections in three different orientations, perpendicularly to each of the principal stress directions. DFN realisations denoted HZ2d are horizontal and perpendicular to SV. DFN realisations denoted with N35W2d and N55E2d are vertical and perpendicular to Sh and SH, respectively.

In order to evaluate the influence of elevated temperatures on the DFN evolution, the present-day stresses according to the geomecon stress model were increased as described in section 2.2.2. The stress conditions are summarised in Table 3.2. The total stresses were implemented as SH = 62.5 MPa, Sh = 36.6 MPa and SV = 16.3 MPa, with P<sub>p</sub> = 5 MPa. Thus, the differential stresses due to thermal load increase for the vertical section N35W by a factor of two to about 46.2 MPa. The differential stresses in section HZ are about the same as for the present-day stress field, and for section N55E the differential stress increases from 0 MPa to about 20 MPa.

### 3.2.3. Results from simulation of increased stresses due to thermal loading

30 simulations were run in order to assess the influence of stress increase due to thermal loading. Simulations were run for ten examples of each of the 2D DFN section representations, i.e. the vertical plane subject to SH - SV (N35W), the vertical plane Sh - SV (N55E), and the horizontal plane SH-Sh (HZ). Each simulation was conducted by calculation steps in which the occurrence of propagation of the fractures in the DFN was evaluated (cf. Appendix A2.3). If the fracture was found to propagate, it was then extended for a predefined length of 0.5 m before the next

calculation step. This procedure was ended when no more fracture growth occurred or a maximum of 10 simulation steps had been performed. It can thus be assumed that if 10 simulation steps needed to be performed, stable conditions could not be reached. Initiation of new fractures was not permitted in the simulations, thus, only existing fractures in the tested DFNs were evaluated.

In the following, the results are presented in viewgraphs that always show the initial DFN (cf. Appendix A2.4) on the left and the last simulation step on the right. The propagating fractures are highlighted in green and red for growth in dominant Mode I (tension) and II (shear), respectively. Note that only the propagated fracture segments of the last simulation step are highlighted. Non-highlighted fractures may have grown in previous simulation steps and in different modes of failure. The Figures show a square with an edge length of 72 m.

The simulations show that the fracture networks during thermal loading are in stable conditions for the horizontal sections and the vertical sections parallel to Sh. For simulations with the DFN in the SV-Sh-plane (N55E), almost no fracture propagation takes place. Fracture growth in the SH-Sh-plane (HZ) does occur but is very limited. The maximum increase in crack length is 1.1 % and appears in DFN FFM01geoDFNr0fixed05\_Hz2d (Figure 3.2). The horizontal sections show a maximum of 3 simulation steps (average 1.3) before stability is reached. While the N55E and HZ sections show an average of 0.0 % and 0.3 % increase in total fracture length compared to the initial DFNs, the increase in the N35E sections parallel to SH amounts to 20.2 % on average (Figures 3.3-3.8), leading to potential increase of fracture connectivity. Fracture propagation in Mode II dominated in 81% of the cases in those sections (Table 3.3).

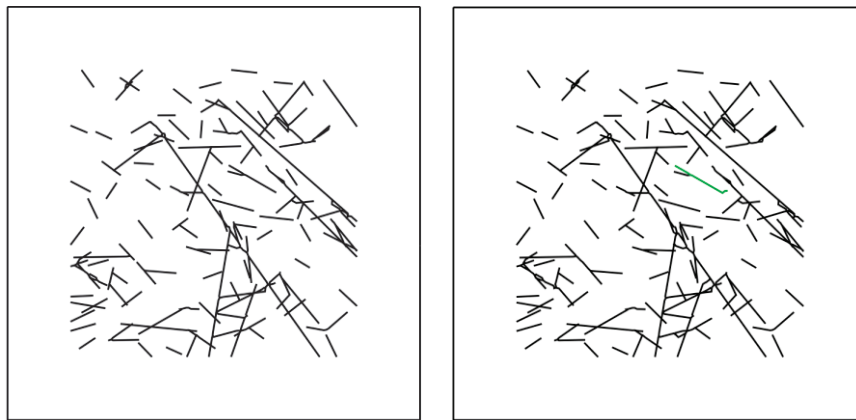


Figure 3.2. Horizontal section. (Left) Initial fracture geometry of FFM01geoDFNr0fixed05\_Hz2d (SH-Sh plane, SH is horizontal). (Right) Fracture propagation in the final simulation step 2. No significant connection of fractures can be observed. Although the last simulation step shows only one fracture propagating in Mode I (green), 83% of fracture growth propagate in Mode II (5 fractures propagating in Mode II in simulation step 1). The initial total fracture length increases by 1.1%.

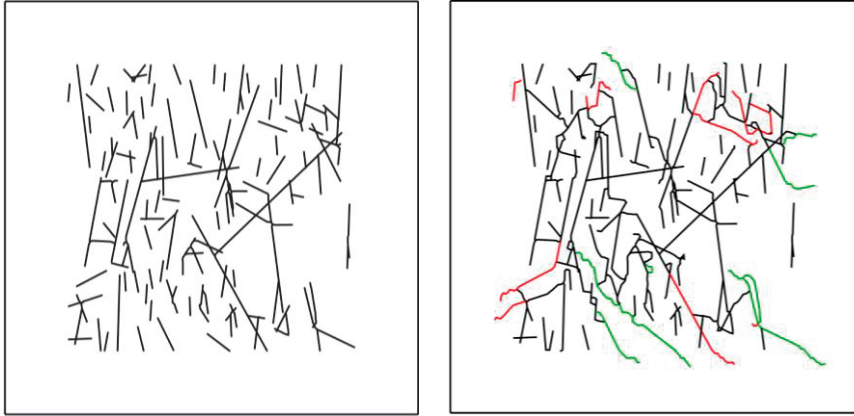


Figure 3.3. Vertical N35W section. (Left) Initial fracture geometry of FFM01geoDFNr0fixed02\_N35W2d (SH-SV plane, SH is horizontal). (Right) Fracture propagation in the final simulation step 10. The initial total fracture length increases by 27.8%.

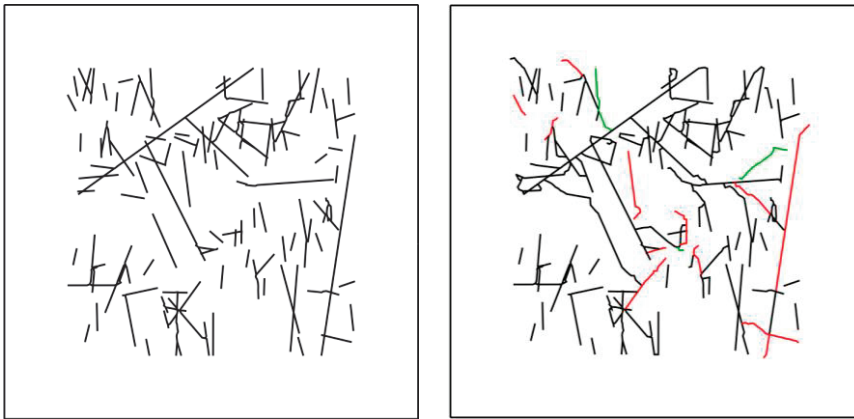


Figure 3.4. Vertical N35W section. (Left) Initial fracture geometry of FFM01geoDFNr0fixed03\_N35W2d (SH-SV plane, SH is horizontal). (Right) Fracture propagation in the final simulation step 10. The initial total fracture length increases by 17.5%.

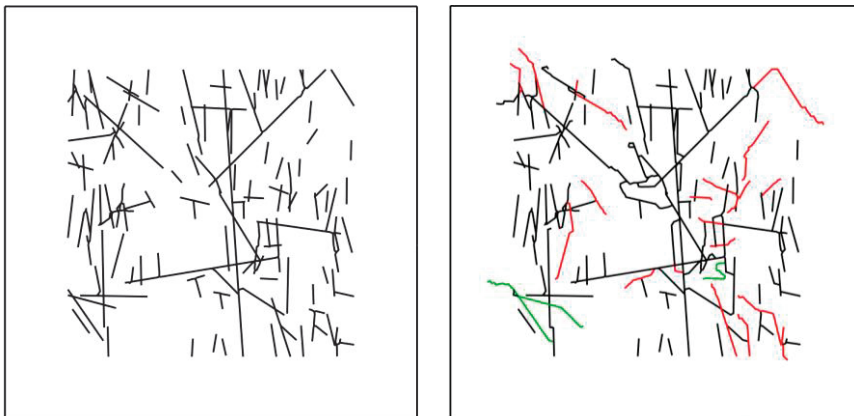


Figure 3.5. Vertical N35W section. (Left) Initial fracture geometry of FFM01geoDFNr0fixed06\_N35W2d (SH-SV plane, SH is horizontal). (Right) Fracture propagation in the final simulation step 10. The initial total fracture length increases by 23.2%.



Figure 3.6. Vertical N35W section. (Left) Initial fracture geometry of FFM01geoDFNr0fixed08\_N35W2d (SH-SV plane, SH is horizontal). (Right) Fracture propagation in the final simulation step 10. The initial total fracture length is increased by 25.4%.

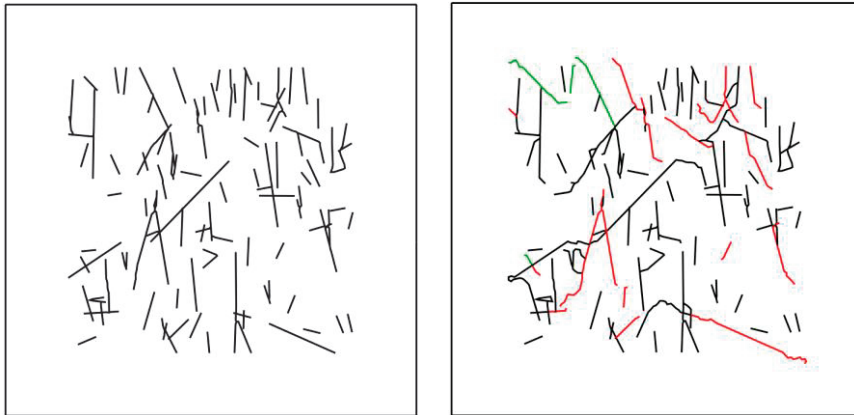


Figure 3.7. Vertical N35W section. (Left) Initial fracture geometry of FFM01geoDFNr0fixed09\_N35W2d (SH-SV plane, SH is horizontal). (Right) Fracture propagation in the final simulation step 10. The initial total fracture length increases by 20.3 %.



Figure 3.8. Vertical N35W section. (Left) Initial fracture geometry of FFM01geoDFNr0fixed10\_N35W2d (SH-SV plane, SH is horizontal). (Right) Fracture propagation in the final simulation step 10. The initial total fracture length increases by 19.3%.

### Influence of temperature on fracture toughness

The simulations have shown that the fractures grow due to the change of differential stress on the model boundaries. If the resistance to shear fracturing were changed due to the influence of temperature, the amount of fracture growth would also be changed. It was shown in an experimental study with a granitic rock that an increase in temperature influences the Mode II fracture toughness,  $K_{IIC}$  (Meier, 2009). The Mode II fracture toughness reported in that study increased by about  $0.7 \text{ MPa} \cdot \text{m}^{1/2}$  for the increase in temperature of  $48^\circ\text{C}$  reported by SKB for the thermal phase (SKB TR-10-23). This corresponds to an increase in Mode II fracture toughness of about 12% compared to the value in Table 5.1.

To analyse if a change in resistance to fracture growth due to the thermal effect on this parameter has a major impact on the results of assessment, simulations were performed to account for this effect. As it was expected, the increase in fracture toughness stabilised the previously unstable fractures by reducing the number of propagating cracks and the average number of simulation steps to reach stability. The increase in total fracture length is significantly reduced from 20.2 % to 6.6 % (Figures 3.9-3.12). This analysis also shows that it is important to verify the governing fracture propagation criterion and related resistance parameters. The reported values for the rock at Forsmark were determined in only one study on a very limited number of samples. Hence, it is not known if the used values reflect the properties of the rock and its variability at Forsmark.

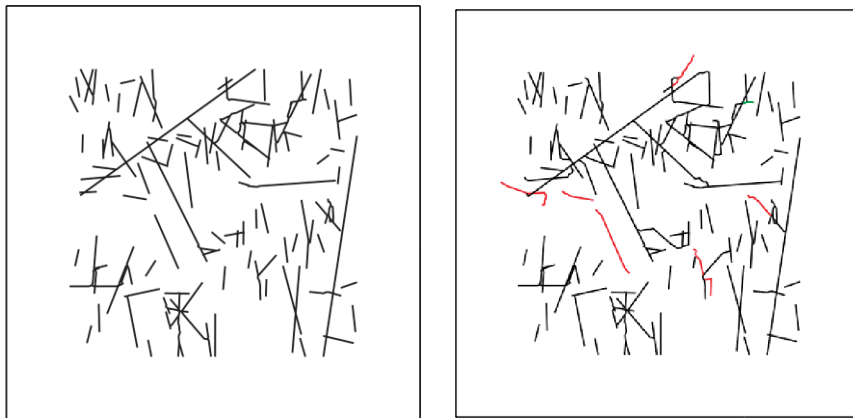


Figure 3.9. Vertical N35W section. (Left) Initial fracture geometry of FFM01geoDFNr0fixed03\_N35W2d (SH-SV plane, SH is horizontal). (Right) Fracture propagation in the final simulation step 10 with an elevated  $K_{IIC}$  due to an increased temperature of about  $50^\circ$ . The initial total fracture length increases by 7.7%.

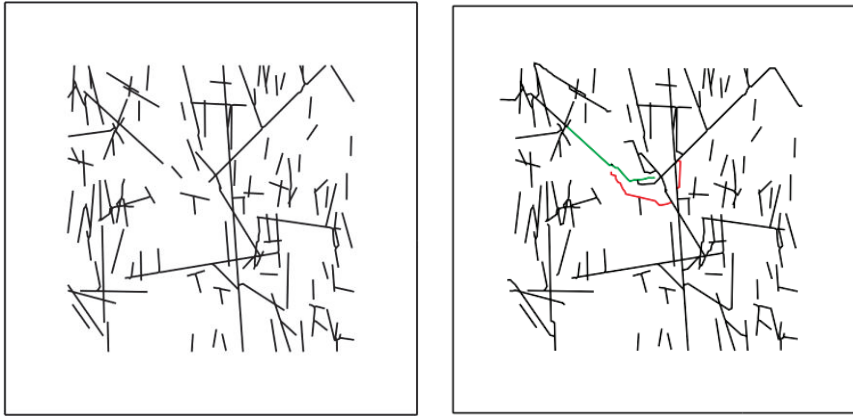


Figure 3.10. Vertical N35W section. (Left) Initial fracture geometry of FFM01geoDFNr0fixed06\_N35W2d (SH-SV plane, SH is horizontal). (Right) Fracture propagation in the final simulation step 10 with an elevated  $K_{IIIC}$  due to an increased temperature of about 50°. The initial total fracture length increases by 6.5%.

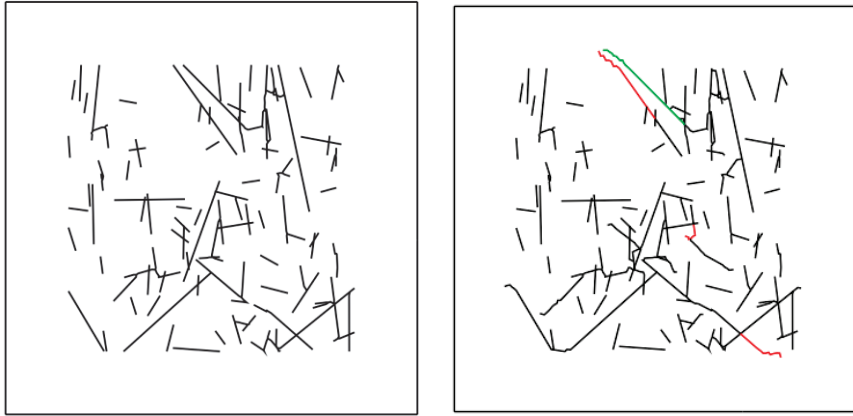


Figure 3.11. Vertical N35W section. (Left) Initial fracture geometry of FFM01geoDFNr0fixed08\_N35W2d (SH-SV plane, SH is horizontal). (Right) Fracture propagation in the final simulation step 10 with an elevated  $K_{IIIC}$  due to an increased temperature of about 50°. The initial total fracture length increases by 9.2%.

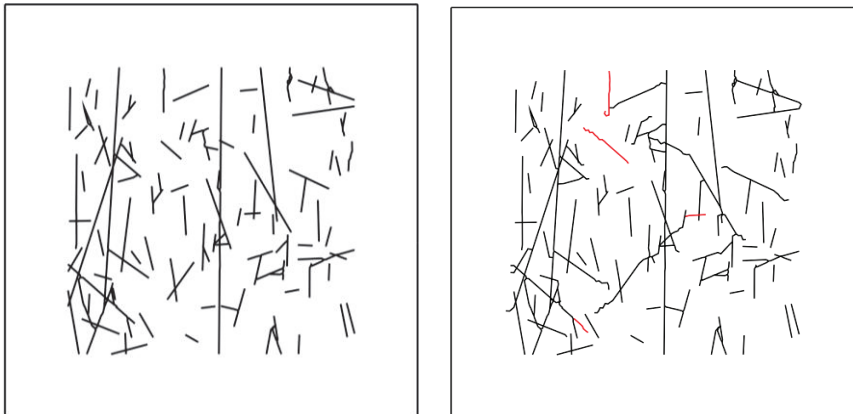


Fig. 3.12. Vertical N35W section. (Left) Initial fracture geometry of FFM01geoDFNr0fixed10\_N35W2d (SH-SV plane, SH is horizontal). (Right) Fracture propagation in the final simulation step 10 with an elevated  $K_{IIIC}$  due to an increased temperature of about 50°. The initial total fracture length increases by 8.4%.

## Influence of the presence of deposition holes on the fracture network growth potential

To analyse the influence of the presence of the deposition holes on the growth of the fracture network, three deposition holes (diameter 1.8 m and 6 m distance between their centres) were introduced into selected DFN realisations. In all tested cases very limited additional fracture growth was taking place. Compared to the simulations without the deposition holes, the growth of total fracture length increased between 0.3% to 0.7%. Fractures near deposition holes were growing to terminate against the deposition holes (Figure 3.13). This is consistent with the results previously published by Backers and Stephansson (2011).

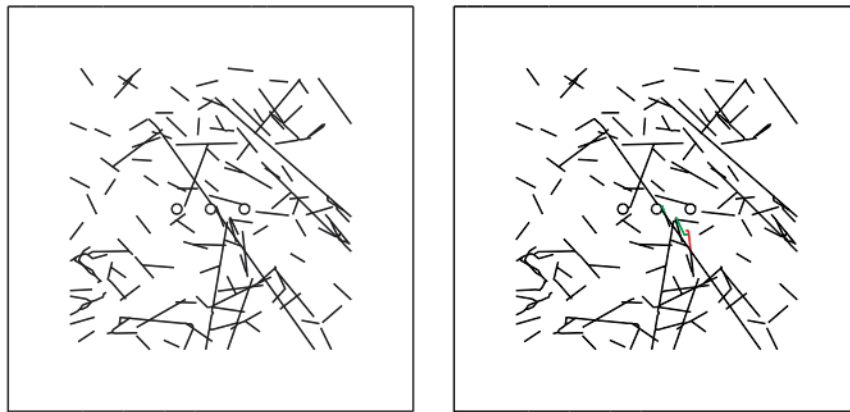


Figure 3.13. Horizontal section. (Left) Initial fracture geometry of FFM01geoDFNr0fixed05\_Hz2d with deposition holes (SH-Sh plane, SH is horizontal). (Right) Fracture propagation in the final simulation step 2. The initial total fracture length is increased by 0.8%.

### 3.3. The Consultants' assessment on the influence of thermal loading on fracture growth

In total, 30 DFN realisations have been simulated with the increased stresses from thermal loading in a particular position in the repository. In the simulations of the vertical sections, moderate extension of the fractures and connection of the fractures forming potential extended fluid pathways have been observed. The simulations have not considered fracture initiation, hence, local effects like spalling or EDZ were not considered. It can be concluded that the influence of the thermal loads on the extension of the fracture network is limited. This also implies that a significant increase in hydraulic connectivity is not to be expected. The maximum change of fracture density P21 due to the fracture growth occurring in the N35W sections, which on average is initially 1.1215 for the r0-fixed base case (cf. Appendix A5.1), is about 5%. One should be aware of the fact that the simulations in 2D may be an oversimplification of real 3D fracture networks in certain cases.

The simulations run in this Chapter were carried out on a fraction ( $< 0.5\%$ ) of all the fractures in the realizations of the DFN model for the rock mass since only fractures longer than 1 m were considered. This approach is conservative in two ways: (a) smaller fractures are generally more stable than longer fractures, so only the least stable fractures were considered in the analysis, and (b) with less fractures in the

simulation domain, longer fractures may propagate larger distances as they will not be able to stop in correspondence of smaller fractures (so called “arresters”). Furthermore, the applied level of stress for the modelling reflects the maximum reported stress increase that only occurs at certain locations in the central part of the repository. For this reasons, the analyses carried out on fracture growth during thermal loading of the repository are probably rather conservative.

The deposition tunnels and deposition holes have been found to have limited effect on growth of nearby fractures. This was to be expected, as the effect of the stress redistribution due to the excavations is limited to few radii, i.e. about 2-4 m from the excavation walls. However, some fractures extend to intercept the deposition holes. This is in agreement with the study by Backers and Stephansson (2011) that showed that some fractures become connected to the deposition holes and may increase connectivity between neighbouring holes. The connection of individual fractures to the deposition holes due to the stress redistribution may lead to increased fluid inflow. The inflow into deposition holes will serve, on one hand as wetting agent for the bentonite, but also may cause increased buffer erosion. Furthermore, the creation of connection to the DFN by fracture propagation into the holes may lead to an increase potential for nuclide transport.

From the analyses it may also be concluded that the formation of fracture linkages that cumulate to a length of the fractures that may be of concern with respect to the integrity of the canisters is not to be expected.

Table 3.3. Fracture propagation statistics for the thermal loading scenario, increased fracture resistance and models with explicit deposition holes. The values are averaged over results with ten DFN realisations per each section. The area of the analysed sections is 2500 m<sup>2</sup>.

		Total length of new cracks	Relative crack length increase	Average propagation angle	Average Mode I growth	Average Mode II growth	Computation steps to stability
Models	Section	[m]	[%]	[°]	[%]	[%]	[-]
Only DFN	HZ	2.3	0.3	36	15	85	1.3
	N35W	135.2	20.2	28	19	81	10.0
	N55E	0.1	0.0	71	100	0	0.2
Only DFN and increased fracture resistance	N35W	44.8	6.6	29	33	67	9.0
With dep. holes	HZ	4.6	0.7	41	18	82	2.1

## 4. Influence of the glacial cycle on fracture growth

### 4.1. SKB's presentation of fracture growth

The effects of a glacial cycle on the state of stress in the repository and fracture stability has been assessed by Hökmark et al. (2010, SKB TR-10-23). Their analysis has been discussed in Chapter 2 of this report and only the main findings are presented here. According to Hökmark et al. (2010) the most critical times during the modelled glacial cycle are just after the second glacial maximum. For this phase, the calculated displacements on fractures are largest. A fracture measuring 200 m in diameter that is optimally oriented (“most critical”, i.e. with shallow dip in the direction of SH, Figure 4.1) would show a maximum elastic deformation at the fracture centre of 12 mm.

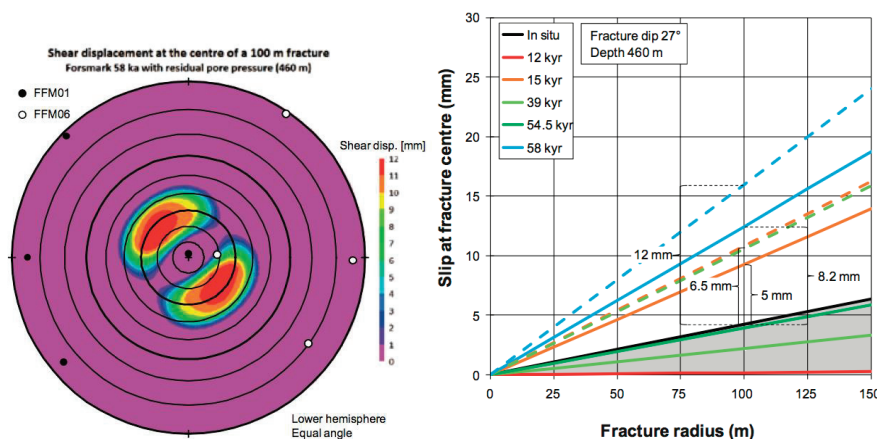


Figure 4.1. (Left) Shear displacements (in excess to present-day stress induced displacement) after 58 000 years with excess pore pressure assumption and fractures of 200 m diameter.

(Right) Shear displacements at repository depth for selected points in time for a pore pressure equal to 98% of the ice thickness (solid lines) and excess pore pressures (dashed lines) (from Hökmark et al., 2010, Figures 7-18 and 7-19).

### 4.2. Independent analyses on the influence of the glacial cycle on fracture growth

#### 4.2.1. Motivation of the assessment

In existing reports by SKB, the mechanical response of fractures to stress changes associated with a glaciation scenario are mainly evaluated in terms of expected displacements along target fractures. This is done in the light of SKB's canister damage

criterion of 50 mm maximum allowed shear displacement along a fracture that intersects a canister position. An issue that is thereby neglected is the potential growth of single fractures and associated increase of connectivity of the existing fracture network. The knowledge of the possibility of fracture growth occurrence is critical since it can significantly affect the integrity rock that is one of the barriers in the repository. The behaviour of the fracture network at the repository is therefore numerically evaluated in this study for the phase of glacially induced stresses.

#### 4.2.2. Modelling setup

For the assessment of the influence of a glacial cycle on the fracture growth potential, a numerical simulation campaign was conducted using the fracture mechanics code roxol (see description in Appendix 4). The numerical framework, the geometrical model and the parameters are summarised in the respective section in Appendix A4.1 to A4.3. The simulation procedure is analogous to that in the Consultants' assessment of the effect of thermally induced stresses as described in the previous chapter. In the glaciation scenario, the ice cover above the repository induces stress changes that were evaluated by Lund et al. (2009, SKB TR-09-15). The glaciation model MT9 has been adopted here as described in Chapter 2. The induced stresses and pore pressures are added to the present-day stresses at five points in time during the glacial cycle according to Table 2.3.

#### 4.2.3. Results of modelling of a glacial cycle

In the following section, the simulation results are summarised for the five time steps T1 through T5 separately. Examples of modelling results are shown.

##### First glacial maximum (T1)

For the first glacial maximum (T1), the stresses were set to  $S_H = 51.5$  MPa,  $S_h = 27.3$  MPa,  $S_v = 31.3$  MPa and  $P_p = 14$  MPa. The simulations show that very limited fracture propagation appears in the 30 analysed DFN realisations. While the increase of the total fracture length is below 0.05 % for the vertical sections, it is slightly more pronounced for the horizontal section with an average of 0.3 %. As the differential stresses are very similar to the present-day in-situ stress state (T0), the DFNs appear to be stable. Figure 4.2 shows an example of the simulation results for a horizontal cross section (SH-Sh plane) where very little fracture propagation, although it represents the case with the most severe fracture growth (0.9% in length) among all the models.

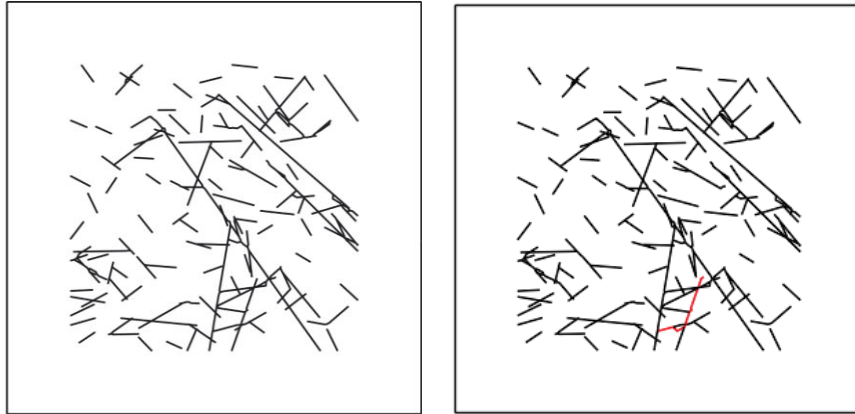


Figure 4.2. Horizontal section. (Left) Initial fracture geometry of FFM01geoDFNr0fixed05\_HZ2d (SH-Sh plane, SH is horizontal). (Right) Fracture propagation in the final simulation step 5. The initial total fracture length increases by 0.9%.

### Retreating ice margin (T2)

For the case of a retreating ice margin (T2), the stresses were adapted to  $SH = 43.0$  MPa,  $Sh = 18.3$  MPa,  $Sv = 13.3$  MPa and  $P_p = 5$  MPa. The fracture networks along sections N55E (Sh-SV plane) and HZ (SH-Sh plane) are in stable conditions. However, the fracture networks on section N35W subjected to SH and SV show fracture growth in some DFN realisations due to the slightly increased differential stresses compared to the present-day conditions. Figure 4.3 to 4.5 show vertical cross sections subjected to SH and SV where an average increase in total fracture length of 0.3 % is observed and an average number of simulation steps before stability of 1.9 is reached.

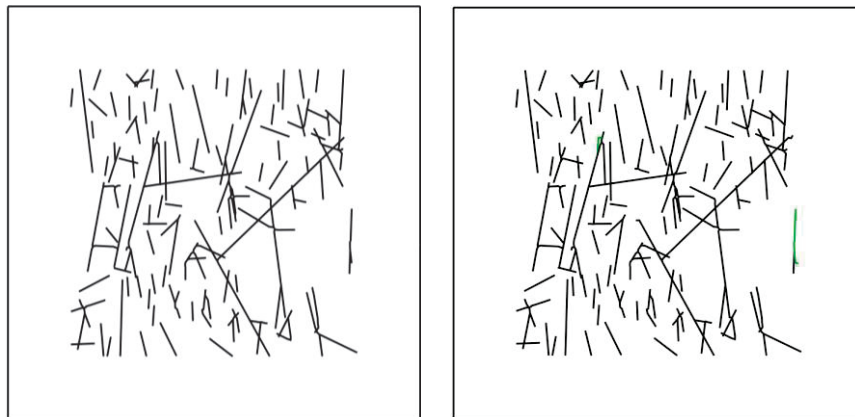


Figure 4.3. Vertical N35W section. (Left) Initial fracture geometry of FFM01geoDFNr0fixed02\_N35W2d (SH-SV plane, SH is horizontal). (Right) Fracture propagation in the final simulation step 3. The initial total fracture length increases by 0.5%.

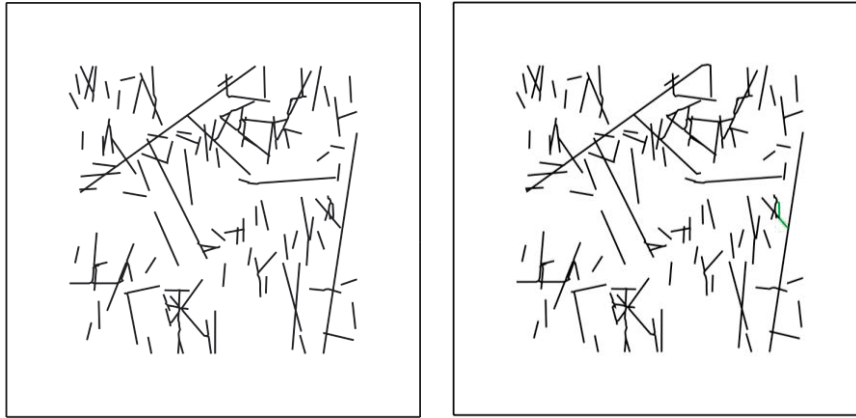


Figure 4.4. Vertical N35W section. (Left) Initial fracture geometry of FFM01geoDFNr0fixed03\_N35W2d (SH-SV plane, SH is horizontal). (Right) Fracture propagation in the final simulation step 2. The initial total fracture length increases by 0.4%.



Figure 4.5. Vertical N35W section. (Left) Initial fracture geometry of FFM01geoDFNr0fixed06\_N35W2d (SH-SV plane, SH is horizontal). (Right) Fracture propagation in the final simulation step 8. The initial total fracture length increases by 2.1%.

### Stress reduction due to a glacial forebulge (T3)

For the case of a stress reduction due to a forebulge (T3), the stresses are modelled as  $SH = 35.5$  MPa,  $Sh = 8.3$  MPa,  $SV = 13.3$  MPa and  $P_p = 5$  MPa. Thus, the stresses for the N35W sections are the same as the background stresses, hence the DFN is stable. Simulations for N55E (Sh-SV plane) show no pronounced fracture propagation as well. However, the simulations of the horizontal sections (HZ) show pronounced fracture propagation in all 10 DFN realisations. Increased differential stresses due to the stress reduction of  $Sh$  and consequently elevated shear stresses are causing fracture propagation that links fractures together. The fracture growth is thereby dominated by Mode I in 94% of the cases. The evolution of the horizontal DFN sections is shown in Figure 4.6 to 4.15.

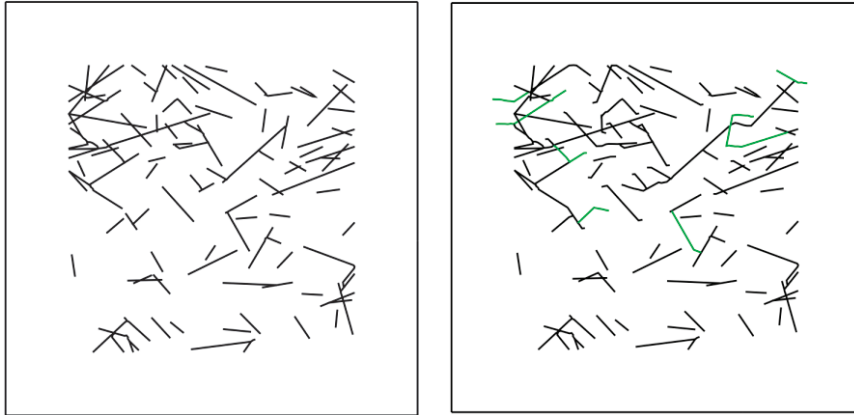


Figure 4.6. Horizontal section. (Left) Initial fracture geometry of FFM01geoDFNr0fixed01\_HZ2d (SH-Sh plane, SH is horizontal). (Right) Fracture propagation in the final simulation step 10. The initial total fracture length increases by 8.3%.

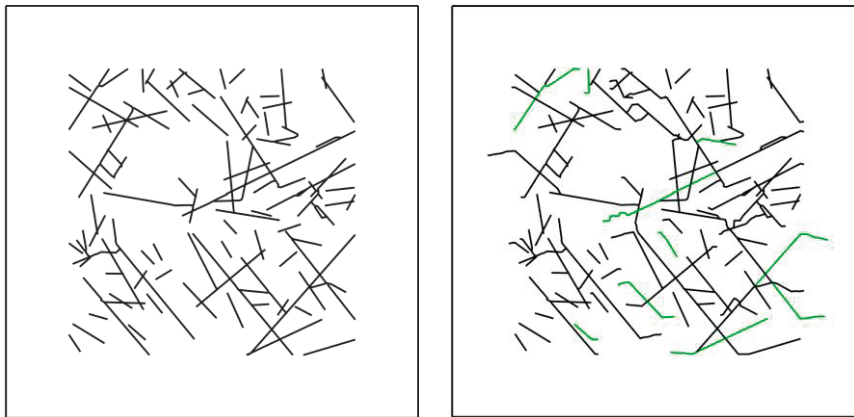


Figure 4.7. Horizontal section. (Left) Initial fracture geometry of FFM01geoDFNr0fixed01\_HZ2d (SH-Sh plane, SH is horizontal). (Right) Fracture propagation in the final simulation step 10. The initial total fracture length increases by 12.8%.

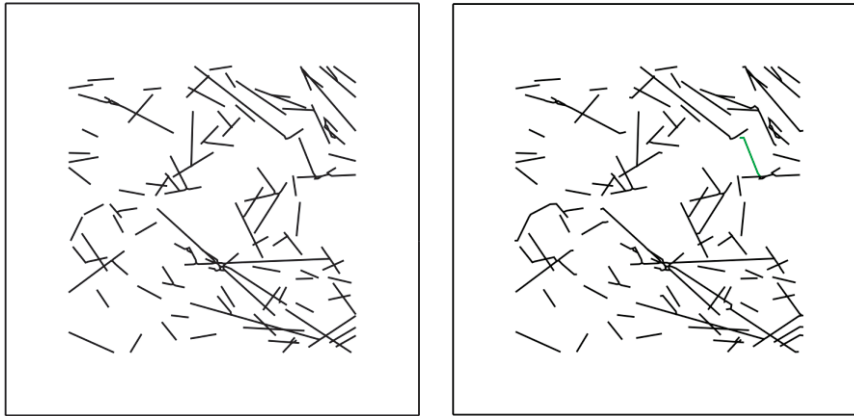


Figure 4.8. Horizontal section. (Left) Initial fracture geometry of FFM01geoDFNr0fixed03\_HZ2d (SH-Sh plane, SH is horizontal). (Right) Fracture propagation in the final simulation step 5. The initial total fracture length increases by 2.4%.

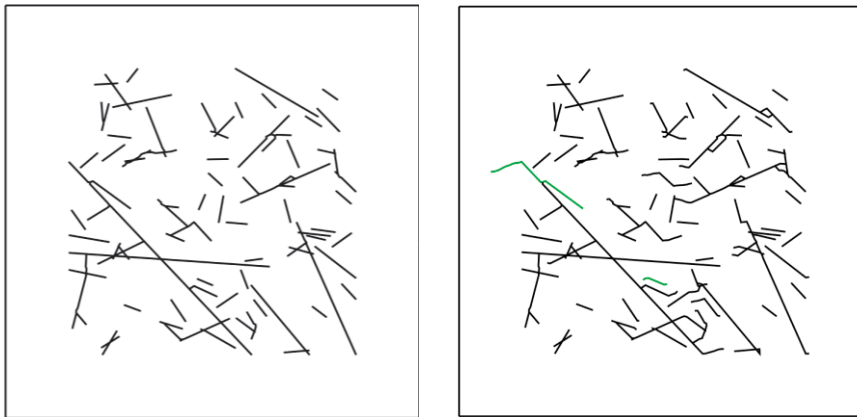


Figure 4.9. Horizontal section. (Left) Initial fracture geometry of FFM01geoDFNr0fixed04\_HZ2d (SH-Sh plane, SH is horizontal). (Right) Fracture propagation in the final simulation step 10. The initial total fracture length increases by 10.8%.

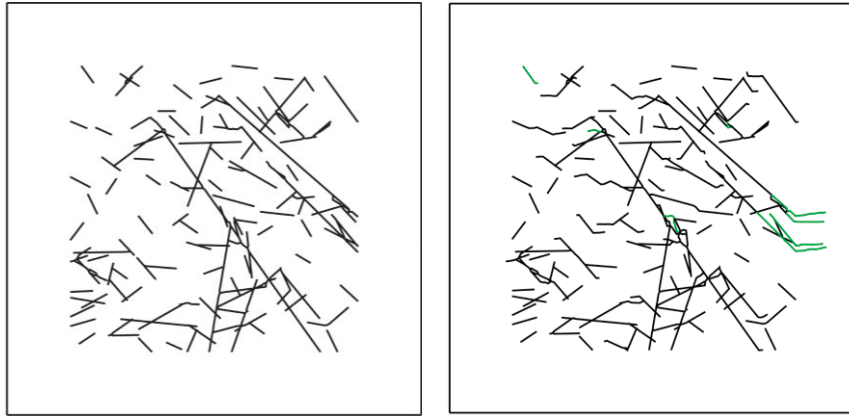


Figure 4.10. Horizontal section. (Left) Initial fracture geometry of FFM01geoDFNr0fixed05\_HZ2d (SH-Sh plane, SH is horizontal). (Right) Fracture propagation in the final simulation step 10. The initial total fracture length increases by 11.5%.

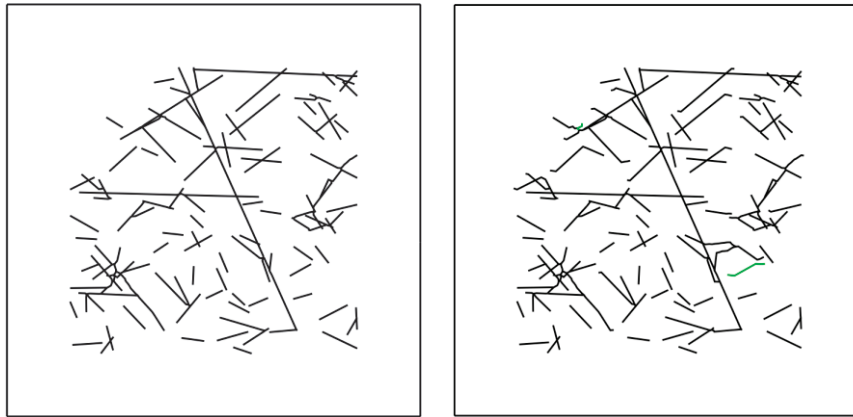


Figure 4.11. Horizontal section. (Left) Initial fracture geometry of FFM01geoDFNr0fixed06\_HZ2d (SH-Sh plane, SH is horizontal). (Right) Fracture propagation in the final simulation step 10. The initial total fracture length increases by 5.4%.

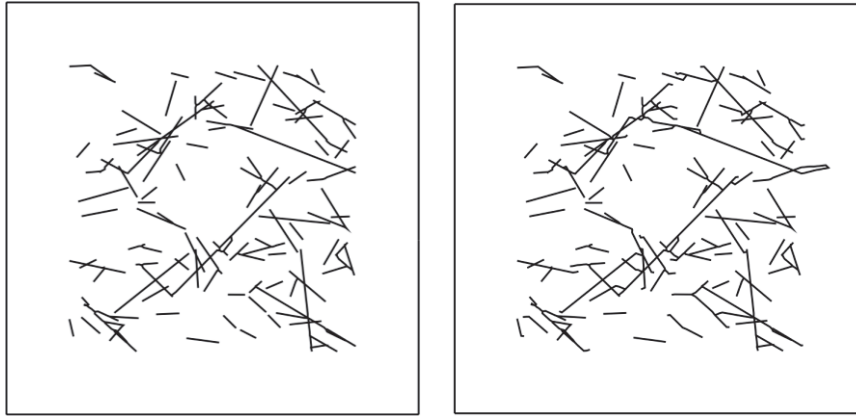


Figure 4.12. Horizontal section. (Left) Initial fracture geometry of FFM01geoDFNr0fixed07\_HZ2d (SH-Sh plane, SH is horizontal). (Right) Fracture propagation in the final simulation step 10. The initial total fracture length increases by 7.5%.

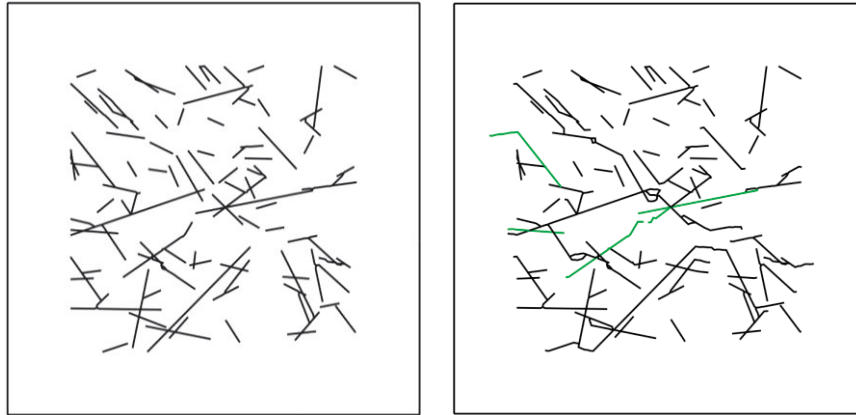


Figure 4.13. Horizontal section. (Left) Initial fracture geometry of FFM01geoDFNr0fixed08\_HZ2d (SH-Sh plane, SH is horizontal). (Right) Fracture propagation in the final simulation step 10. The initial total fracture length increases by 10.9%.

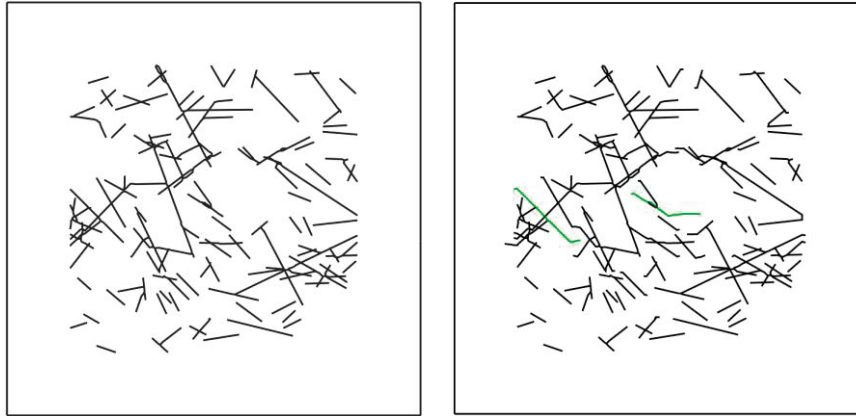


Figure 4.14. Horizontal section. (Left) Initial fracture geometry of FFM01geoDFNr0fixed09\_HZ2d (SH-Sh plane, SH is horizontal). (Right) Fracture propagation in the final simulation step 10. The initial total fracture length increases by 5.2%.

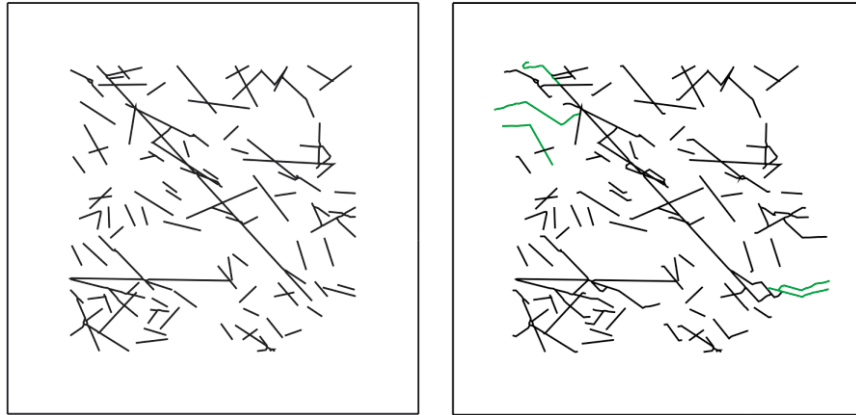


Figure 4.15. Horizontal section. (Left) Initial fracture geometry of FFM01geoDFNr0fixed10\_HZ2d (SH-Sh plane, SH is horizontal). (Right) Fracture propagation in the final simulation step 10. The initial total fracture length increases by 12%.

### Second glacial maximum (T4)

For the second glacial maximum (T4), the stresses were set to  $SH = 64.5$  MPa,  $Sh = 40.3$  MPa,  $SV = 41.3$  MPa and  $P_p = 19$  MPa. The simulations show very little fracture propagation (at most 1.1% in length) in all sections of the fracture network realisations.

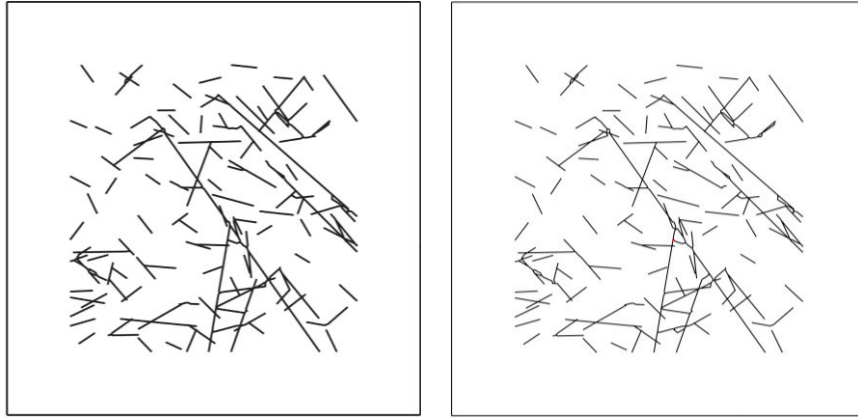


Figure 4.16. Horizontal section. (Left) Initial fracture geometry of FFM01geoDFNr0fixed05\_HZ2d (SH-Sh plane, SH is horizontal). (Right) Fracture propagation in the final simulation step 3. The initial total fracture length increases by 1.1%.

### Retreating ice margin (T5)

For the final case of a retreating ice margin (T5) after the second glacial maximum, the stresses were modelled as  $SH = 48.0$  MPa,  $Sh = 22.3$  MPa,  $SV = 13.3$  MPa and  $P_p = 5$  MPa. For the fracture network realisations of HZ and N55E only few fractures grow, with stability being reached after 1.2 and 0.4 simulation steps, respectively. However, the fracture network realisations N35W show more pronounced fracture propagation, which is shown in Figure 4.17 to 4.21. Increased differential stresses are causing fracture propagation into intact rock. An average of 5.4 simulation steps are performed before stability is reached. The increase in total fracture length for this sections is 1.3 %.



Figure 4.17. Vertical N35W section. (Left) Initial fracture geometry of FFM01geoDFNr0fixed02\_N35W2d (SH-SV plane, SH is horizontal). (Right) Fracture propagation in the final simulation step 10. The initial total fracture length increases by 3.4%.

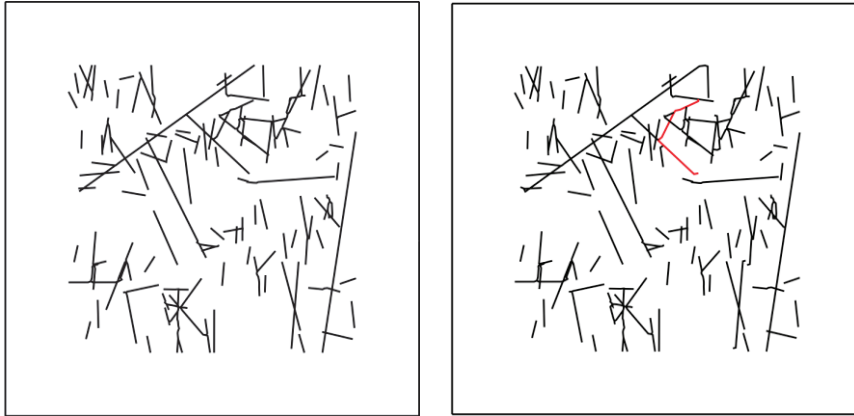


Figure 4.18. Vertical N35W section. (Left) Initial fracture geometry of FFM01geoDFNr0fixed03\_N35W2d (SH-SV plane, SH is horizontal). (Right) Fracture propagation in the final simulation step 5. The initial total fracture length increases by 1.3%.



Figure 4.19. Vertical N35W section. (Left) Initial fracture geometry of FFM01geoDFNr0fixed06\_N35W2d (SH-SV plane, SH is horizontal). (Right) Fracture propagation in the final simulation step 10. The initial total fracture length increases by 2.3%.



Figure 4.20. Vertical N35W section. (Left) Initial fracture geometry of FFM01geoDFNr0fixed07\_N35W2d (SH-SV plane, SH is horizontal). (Right) Fracture propagation in the final simulation step 6. The initial total fracture length increases by 1.7%.

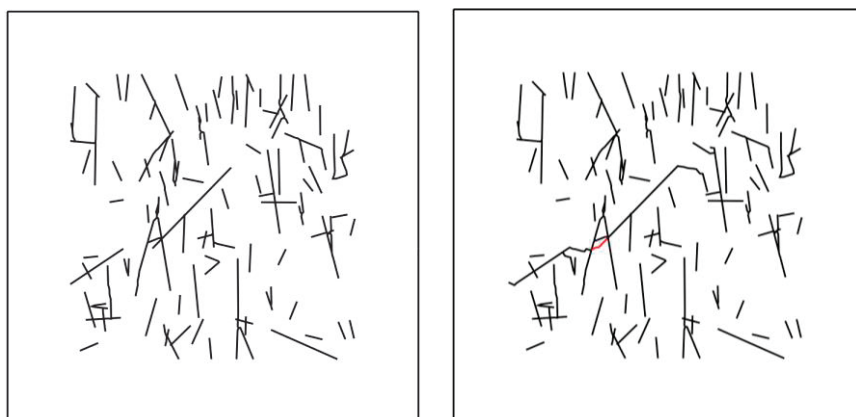


Figure 4.21. Vertical N35W section. (Left) Initial fracture geometry of FFM01geoDFNr0fixed09\_N35W2d (SH-SV plane, SH is horizontal). (Right) Fracture propagation in the final simulation step 10. The initial total fracture length increases by 2.8%.

### 4.3. The Consultants' assessment on the influence of the glacial cycle on fracture growth

The simulation campaign analysing the impact of a glaciation on the growth of the fractures in the DFN has shown that the impact in most of the glacial phases is minor. Only during forebulge periods it may be expected that some fractures extend in such a way that the fractures coalesce and form few additional pathways for fluids. The fact that during the glacial maxima (T1, T4) all DFNs stay stable with very limited fracture growth is a good verification of the predictive capacity of the numerical modelling. This result perfectly fits to the analytical evaluation of fracture stability (cf. chapter 2), which indicated a stabilising effect during those stages of maximum ice thickness. During the stages of retreating ice margins (T2, T5), when only horizontal stresses are increased, a slight increase in fracture propagation is observed. This also mirrors the analytical results. However, if the principal stress directions would rotate, different fracture sets might propagate and connect. Indicatively, it would appear that the thermal phase would be stable while T1 and T4 could be less stable.

The maximum change of fracture density P21, which on average is initially 1.1215 for the r0-fixed base case (cf. Appendix A2.3), occurs due to the fracture propagation for the horizontal sections and is about 2%. One however has to bear in mind that the simulations were run on 2D models of cross sections that may be an oversimplification of real 3D fracture networks in certain cases.

Further, it needs to be emphasised that SKB provide several stress evolution histories for the glaciation period, reflecting the high uncertainty in the models. It is therefore suggested to perform a stress sensitivity analysis on the DFN stability to be able to identify the limits for tolerable fracture network growth. If identified, one could assess the likelihood for such stress conditions during future glaciations in Scandinavia.

If the present-day stress model by Martin (2007) would have been used for the above analyses, it would have resulted in different amounts of fracture propagation,

depending on the glacial evolution stage and the section of interest. In general, slightly more fracture propagation during stages of ice retreat (T2, T5) would be expected compared to the case with the stress model by Backers et al. (2014, SSM Technical Note 2014:10). During the forebulge period (T3), however, it would have resulted in much less fractures propagation than for the stress model employed here.

The rock mass at Forsmark was subject to similar loading in the past during the last glaciation. Therefore, the present day DFN should include a signature of the effects of past glacial loading. In the light of this, the assumptions in this analysis are potentially conservative and the fracture extension analysis might overestimates the fracture growth. Additionally, one may discuss if the stress field assumptions are correct or if the fracture mechanics parameters correctly reflect the rock mass at Forsmark.

Table 4.1. Fracture propagation statistics for the glaciation loading scenarios. The values are averaged over ten DFN realisations per section. The area of the analysed sections is 2500 m<sup>2</sup>.

		Total length of new cracks	Relative crack length increase	Average propagation angle	Average Mode I	Average Mode II	No. of computation steps to stability
Time	Section	[m]	[%]	[°]	[%]	[%]	[-]
<b>T1</b>	HZ	1.9	0.3	33	33	67	1.7
	N35W	0.2	0.0	37	17	83	0.5
	N55E	0.1	0.0	54	50	50	0.2
<b>T2</b>	HZ	1.1	0.2	46	52	48	0.7
	N35W	2.7	0.3	45	83	17	1.9
	N55E	0.1	0.0	54	100	0	0.2
<b>T3</b>	HZ	59.1	8.7	24	94	6	9.5
	N35W	0.8	0.1	52	92	8	0.9
	N55E	0.0	0.0	54	100	0	0.2
<b>T4</b>	HZ	2.4	0.3	35	9	91	1.3
	N35W	0.5	0.1	30	0	100	0.9
	N55E	0.1	0.0	60	67	33	0.3
<b>T5</b>	HZ	1.4	0.2	37.7	37.5	62.5	1.2
	N35W	9.3	1.3	38.3	70.5	29.5	5.4
	N55E	0.1	0.0	53.6	100.0	0.0	0.4



## 5. Influence of time dependent fracture growth

### 5.1. SKB's presentation of time dependent fracture growth

SKB assumes that time-dependent effects including subcritical fracture growth need not to be considered in the analysis of rock deformation (SKB TR-11-01, p. 336 ff). According to SKB the *“concept of creep implies that a material has inherent time-dependent mechanical properties so that movements take place without additional loading, due to already active stresses. The consequence of extensive creep movement along fractures would be that fracture shear stresses would relax and that the stress state would tend to be less deviatoric over time. However, there is no evidence, anywhere in the world where deep mining is carried out in hard rocks that such a condition exists, i.e. substantial deviatoric stresses are recorded at all mine sites.”* Additional justification they take from a paper by Damjanac and Fairhurst (2010), where it is concluded that *“the threshold (for long term strength) is of the order of 40% of the unconfined compressive strength or higher for laboratory specimens under unconfined compressive loading, and increases rapidly in absolute value with confinement.”*

### 5.2. The Consultants' assessment of time dependent fracture growth

#### 5.2.1. Motivation of the analyses of time dependent deformation fracture growth

The argumentation by SKB on time dependent fracture growth is very concise and it assumes the following that can be objected:

- The stresses acting on the fractures are below the critical values for chemically motivated fracture growth. Although continuously discussed for good reasons, a lower threshold has never been experimentally determined. The lower bound is not known for rock in geological relevant time scales. For Äspö diorite it has been reported subcritical fracture propagation at 75% of  $K_{IC}$  and 85% of  $K_{IIC}$  (Backers et al., 2006).
- The fracture network at Forsmark can be assumed stable today. This implies that no significant fracture extension takes place. But an increase in differential stress will increase the stress intensity at the fracture tips and the fracture may become unstable and grow. This might be in particular the case close to excavations where stresses are magnified by redistribution.
- The study by Damjanac and Fairhurst considers Mode I (tensile) micro-fracturing only, which might be appropriate at ambient conditions. This is questionable at higher confining stresses, as Mode II (in-plane shear) and Mode III (out-of-plane shear) driven micro-fracture growth becomes an issue (Backers et al., 2002).

- SKB discusses creep of rock material, which is different from subcritical fracture growth. Creep of rock material is generally the time-dependent deformation of rock, which may be linked to different mechanisms like twinning, dislocation, and time-dependent micro-fracture growth. In contrast, and this is of larger concern in the context of the mechanical behaviour of fractures, time-dependent (i.e. subcritical) fracture growth is the slow extension of macro fractures under static loads. This chemically driven process has been shown to exist for Mode I, Mode II and Mode III loading in hard rocks (Atkinson, 1991; Backers et al., 2006; Ko and Kemeny, 2011).
- The velocity of fracture growth is dependent, amongst other parameters, on humidity (higher humidity implies higher fracture propagation velocity), and temperature (higher temperature promotes higher chemical activity which implies higher fracture propagation velocity). In turn, one may argue that a temperature increase reduces the threshold for fracture growth.

Hence, it needs to be discussed, if fracture extension can take place with the changes of boundary conditions, e.g. temperature, humidity, loading and stress, occurring at the repository, and if these may contribute to a fracture network development that may be relevant for the long-term safety.

### 5.2.2. Discussion of the time dependent fracture growth

If the stress intensity at the fracture tip is below the critical threshold for rapid fracture extension, i.e. below fracture toughness, it was shown for different materials that a fracture will grow stable and slowly. If the loading is reduced, the fracture stops growing. The higher the stress intensity is, the faster the fracture propagates. This can be described by Charles' law as a linear relation in log-log space (Lawn, 1993).

At constant loading conditions, a sub-critically extending fracture will be self-accelerating. As the fracture grows it becomes longer, and it is generally assumed that the length of a fracture positively correlates to the stress intensity factor at its tip. An higher stress intensity leads to faster extension of the fracture, as the stress intensity becomes closer to the threshold for rapid fracture extension.

Backers et al. (2006) have shown that Äspö diorite, (a) creeps under triaxial stress conditions, and (b) shows sub-critical fracture propagation for both loading Mode I and Mode II at levels of stress below the critical load. The strain rate stepping tests performed in the context of that study showed that for differential stress as low as 60% of the short term strength values creep is evident. In the experimental campaign on sub-critical fracture growth, lower limits for fracture extension were not found. However, sub-critical fracture propagation was confirmed at levels of about 75% of  $K_{IC}$  for tensile loading, and about 85% of  $K_{IIC}$  for in-plane shear loading. The testing campaign was carried out on saturated specimens, that showed reduced fracture toughness compared to values determined on dry samples: 30% lower values for loading Mode I ( $2.7 \text{ MPa} \cdot \text{m}^{1/2}$  instead of  $3.8 \text{ MPa} \cdot \text{m}^{1/2}$ ), and 12% lower values for loading Mode II ( $4.5 \text{ MPa} \cdot \text{m}^{1/2}$  instead of  $5.1 \text{ MPa} \cdot \text{m}^{1/2}$ ). It is assumed that the Äspö diorite shows in general similar behaviour to the relevant rock types at Forsmark (i.e. granite and granodiorite). Hence, the conclusion and related arguments brought forward by SKB, that time-dependent fracturing is not an issue per se, are not correct.

The results for the Äspö diorite referred to above are for experiments on small specimens, and only prove that subcritical fracture extension is evident at laboratory scale. Extrapolation to the meter scale bears, besides the general scaling problems, the issue, that inhomogeneities exist on different scales and may serve as energy sinks and hence stop fracture extension (so-called arrester positions). These arrester positions may be due to differences in mineralogical composition, large crystals or most prominently other fractures. While the lithological inhomogeneities may be of secondary importance and relevant for short fractures only, the structural features, i.e. other fractures, are of major significance in this context. Any discontinuity in the path of the propagating fracture will have the potential to stop the propagation or change the direction of propagation. Firstly, the encountered fracture might be inclined with respect to the direction of the propagating fracture, and hence it will be less loaded under given conditions, being presumably stable and not extending. Secondly, the propagating fracture runs into the other fracture and the created junction will absorb the stress concentration. Hence, the subcritical fracture propagation will eventually stop.

From the analysis of today's situation of fracture domain FFM01 at Forsmark it may be concluded that at a  $rp$  of 0.65 or below subcritical fracture propagation does not take place (see Figure 5.1a). During the thermal phase, the fracture sets are also stable (see Figure 2.8). During the glaciation the reactivation potential at most times is below 0.65 except for T3 (Figure 5.1d). The passing of the glacial forebulge shows higher reactivation potentials, but as the limit for subcritical crack growths is not known, it cannot be concluded that the fractures will extend.

The N-S striking and steeply dipping fracture set is subjected to roughly 85% of the maximum reactivation potential (Figure 5.1), and hence the only set potentially prone to sub-critical shear extension. Extension may be stopped by one of the other three sets and hence the issue is of minor importance. It is of interest to analyse, if the N-S striking fracture set is mostly ending against fractures of the WNW or WSW striking fracture sets. If so, this would be an evidence of the existence of significant sub-critical fracture growth under today's stress conditions. From an analysis by Fox et al. (2007, SKB R-07-46) this could not be confirmed.

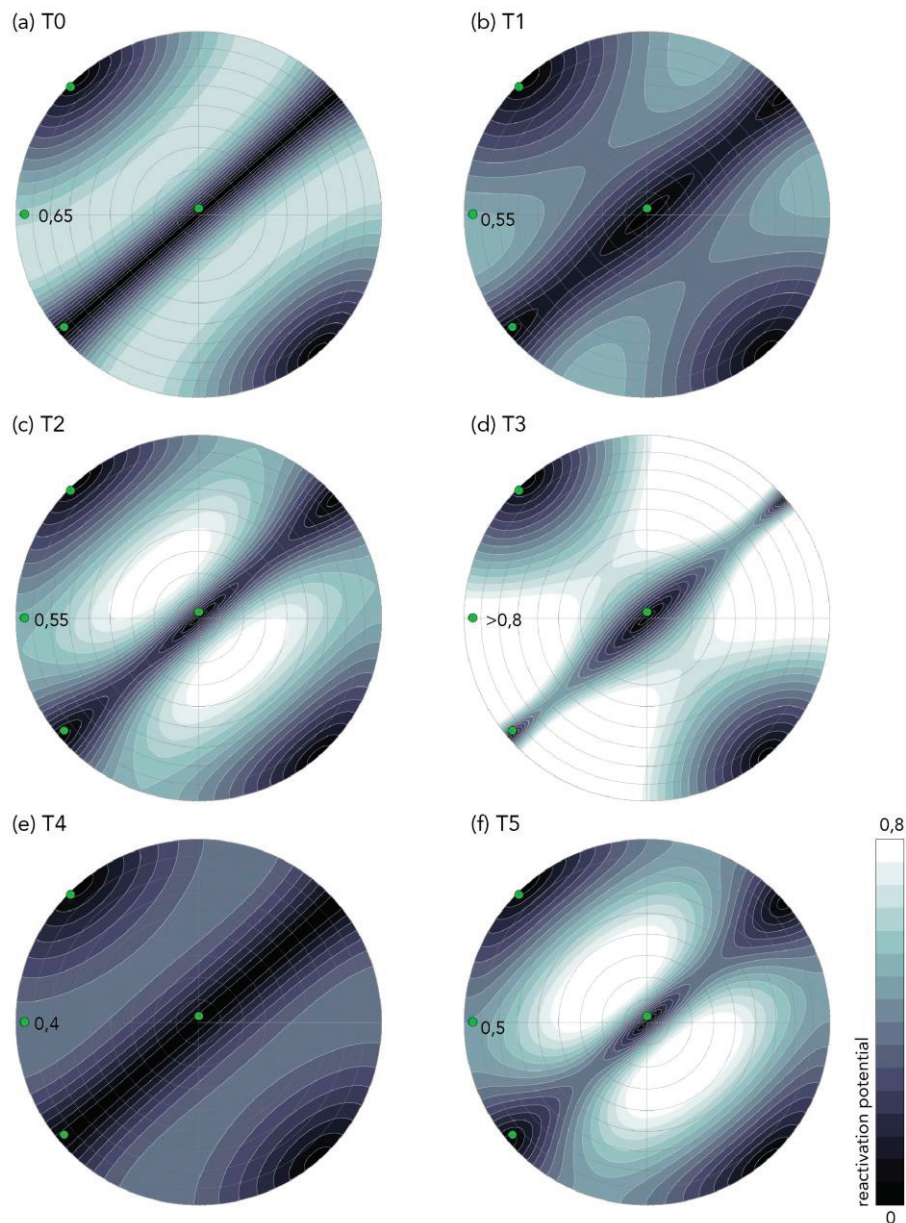


Figure 5.1. Pole plot with global fracture sets for FFM01, showing the reactivation potential when the geomecon stress field model at a depth of 500 m is assumed (T0) superposed to the glacial stress conditions at time T1 through T5.

### 5.3. The Consultants' assessment on time dependent fracture growth

SKB concludes that time-dependent effects including subcritical fracture growth need not to be considered in the analysis of rock deformation. This is only partially correct; the Consultants assess that time dependent fracture extension is not a mechanism considerably impacting the extent of the undisturbed fracture network evolution. If sub-critical fracture extension would occur, it should be confined to small

rock volumes, as fractures in preferred orientations (which are N-S-striking and steeply dipping fractures) would propagate only short distance into a fracture of another fracture set before stopping. As the fracture density is quite large (see Fox et al., 2007, SKB R-07-46 and Figure 5.2), hence, the extension of selected and preferably longer fractures will only be several decimetres.

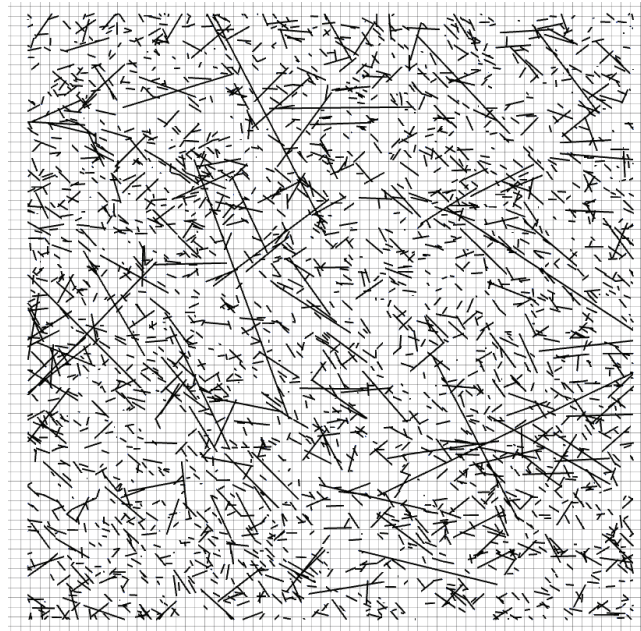


Figure 5.2. DFN realisation of the rock mass in the repository (realisation FFM01geoDFNR0fixed09\_HZ2D). The maximum distance for fractures to extend is several decimetres. The edge of the area shown here is 50 m long.



## 6. Influence of an earthquake on fracture growth

### 6.1. SKB's presentation

Two mechanisms related to the earthquake scenarios that potentially could damage the emplaced fuel canisters are identified by SKB: (1) Direct fault movement along a seismogenic fault that intersects the repository and (2) secondary displacements on fractures induced by an earthquake. La Pointe et al. (1997, SKB TR-97-07) performed numerical simulations to calculate the slip on secondary fractures due to earthquakes of varying magnitudes as a function of the distance from the seismogenic fault to a repository (Figure 6.1). They further found a linear scaling behaviour between the fracture radius and the resulting shear offset as calculated by the numerical model with the code POLY3D. The developed methodology was then applied to three generic sites in La Pointe et al. (1999, SKB TR-99-03). The sensitivity to input parameters and conservativeness of the results have been assessed in La Pointe et al. (2000, SKB TR-00-08).

Fälth and Hökmark (2007, SKB R-06-48) and Fälth et al. (2010, SKB TR-08-11) similarly evaluated the effect of earthquakes on displacements of target fractures by means of numerical simulation with the 3DEC code and came to similar conclusions. Their results are presented as “respect distances” as a function of fracture size for specific magnitudes and a given displacement of 50 mm. Their results seem to fit reasonably well to the analyses of La Pointe et al. (2000, SKB TR-00-08).

All studies found that the most important factors for target fracture displacement are earthquake magnitude, distance from the seismogenic fault to the target fracture and the fracture size.

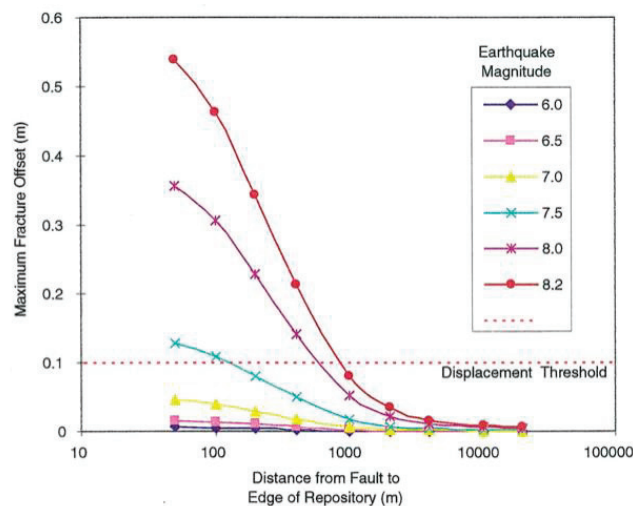


Figure 6.1. Maximum displacement on fractures induced by earthquakes of varying magnitudes and distances to the repository (from La Pointe et al., 1997, SKB TR-97-07, Figure 4-7). Note that the displacement threshold has been reduced from 100 to 50 mm in the present SKB's design premises.

## **6.2. The consultants' assessment of the influence of an earthquake on fracture growth**

### **6.2.1. Motivation of the assessment**

The displacements on target fractures have been estimated by SKB using a set of simplifying assumptions. Fractures were assumed to be frictionless and cohesionless, and to behave linear-elastically without the possibility of propagation. This is conceivable because SKB needed to develop a method for evaluating the risk that fracture displacement along a fracture intersecting a canister position would exceed the canister damage criterion of 50 mm in the event of an earthquake. Those analyses were done mainly for the purpose of site selection, repository layout design and deposition acceptance criteria.

However, the evolution of the fracture network in response to an earthquake was not assessed by SKB. The potential growth of fractures is critical for the repository integrity as e.g. fractures initially not intersecting deposition holes may grow to reach deposition holes where canisters with spent nuclear fuel were placed.

Additionally, as it has been pointed out in the SKB reports, the displacement along a fracture should be a function of the fracture size. Should a set of fractures be substantially propagating and coalescing to form longer features that also reach the deposition holes, the implied maximum displacements would likewise increase and might exceed the imposed maximum of 50 mm displacement. This even if criteria as respect distances from deformation zones and maximum critical radii of the fractures intercepting deposition holes are applied.

### **6.2.2. Analyses**

In the following analyses with roxol, three earthquake scenarios are evaluated. Two earthquakes have moment magnitude 6 and one moment magnitude 7. The earthquakes differ in terms of size of rupture plane, maximum displacement and distance to the repository.

In the course of previous assignment commissioned by SSM (Backers et al., 2014, SSM Technical Note 2014:58), the effect of an earthquake on deformation zone stability has been evaluated by geomecon GmbH by using the code Comsol. Numerical simulations of three different strike-slip earthquakes on regional deformation zones of the Forsmark tectonic lens were carried out (Figure 6.2). The results in terms of induced stresses resulting from those analyses provide the input for the numerical simulation of the evolution of the fracture network in this Chapter.

In case of dynamic stress changes, as for the earthquake scenarios, the static critical values in Table 3.1 are potentially incorrect. Available dynamic data to be input in the models is extremely limited in the literature and unknown for the rocks at Forsmark. As for dynamic loadings, some studies suggest that dynamic critical values are potentially higher than static values, therefore, the fracturing during dynamic loading predicted in this Chapter will be overestimated by roxol.

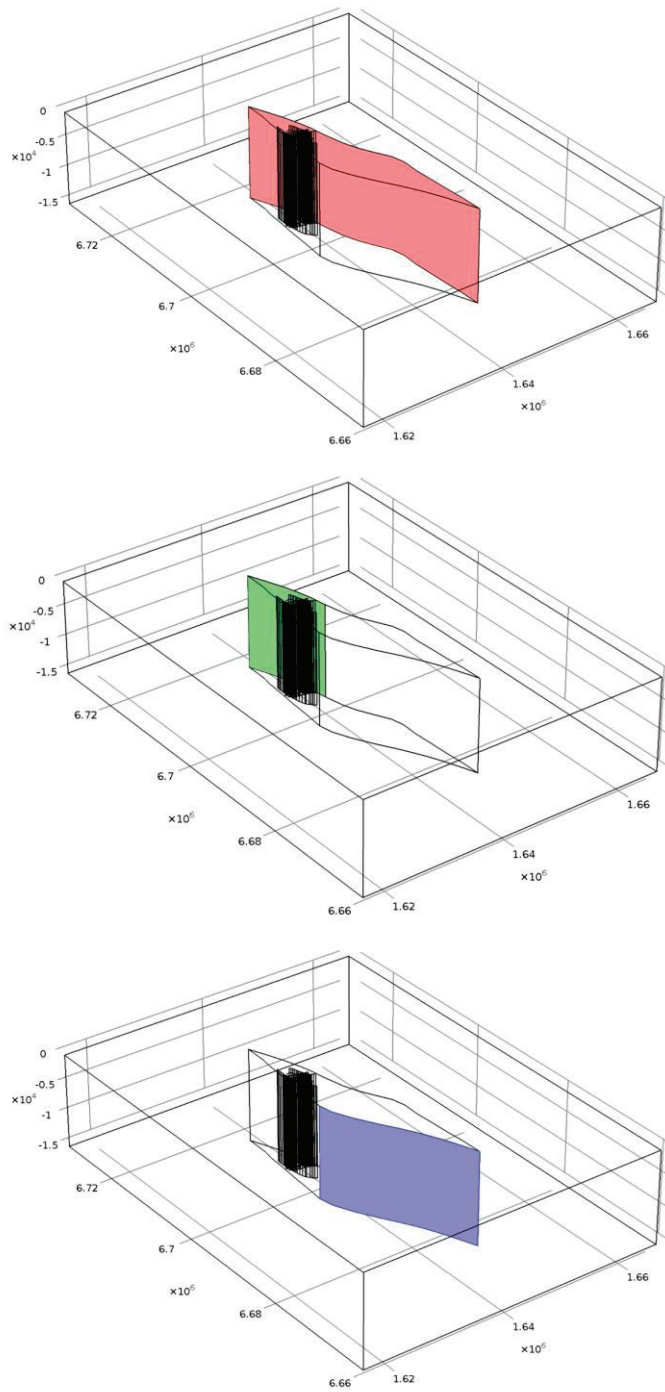


Figure 6.2. Modelled rupture areas for the three earthquake simulations on the regional deformation zones that define the Forsmark tectonic lens. The red area corresponds to the M7 earthquake, the green and the blue areas correspond to the proximal and distal M6 earthquakes, respectively. The respective sizes and assigned displacements are summarised in Table 6.1 (Backers et al., 2014, SSM Technical Note 2014:58).

Table 6.1. Rupture areas and displacements as realised for the earthquake simulations.




Color code	Moment Magnitude	Rupture Area [km <sup>2</sup> ]	Maximum Displacement [m]
	M7	643.8	9.0
	M6	373.7	0.5
	M6	205.7	0.9

Table 6.2. Stresses during times of maximum reactivation potential as they evolve during the earthquake simulations of the M7 and proximal M6 earthquakes, respectively, assuming the in situ stresses according to Backers et al. (2014, SSM Technical Note 2014:10).

	SH	Sh	Sv	P <sub>p</sub>
Moment Magnitude	[MPa]	[MPa]	[MPa]	[MPa]
M7	43,2	-0,4	13,3	5
M6	36,6	12,6	13,2	5

The earthquake induced displacements and stress increments of SH, Sh and SV within the repository were measured every 0.25 s for a period of 10 s after the rupture and are presented in Figure 6.3 and 6.4 for the M7 earthquake, and in Figures 6.27 and 6.28 for the proximal M6 earthquake. The induced stresses during times of maximum reactivation potential for the respective earthquakes were chosen for the evaluation of fracture growth (Table 6.2). A change of fluid pressure was not resolved by the simulations and hence not considered.

The simulations with roxol are carried out as static calculations with given stresses at time of maximum reactivation potential. Using the stress state at maximum reactivation potential also reflects the moment of maximum potential shear displacement. The approach is therefore conservative because:

- There is a major difference between a dynamic and static loading. In dynamic loading conditions, the momentum of inertia will result in much more stable conditions than for the correspondent static loading conditions. This is also reflected by the fact that fracture toughness for fracture propagation in Mode I is reported to exponentially increase with acceleration. In the simulations in this report, static loading and static critical values for fracture extension have been used. Hence, fracture extension will be overestimated.
- The simulations run here were carried out with only on about 0.5% of all the fractures generated in the DFN realizations. Fractures shorter than 1m were not considered. This approach is conservative since smaller fractures are generally more stable than longer fractures, and longer fractures may propagate larger distances before stopping because some fractures functioning as arresters are ignored in the models. Hence, fracture extension will be overestimated.

Comsol cannot take into consideration failure of the rock and deformation zones due to tensional loads, therefore, some of the resulting stress increments might be over-estimated in magnitude. Limited tensile strength of the zones would probably result in damping and scattering of the seismic wave hitting them. Tensile stresses would probably induce tensile cracks during the propagation of the seismic wave through the rock mass and thereby damping it. As the simulations ignore these effects, we consider the stress increments to be used for further analyses as conservative.

### 6.2.3. Magnitude 7.0 earthquake

An earthquake of magnitude 7.0 was simulated according to estimations of maximum possible earthquake magnitudes on regional deformation zones (M7.2 according to SKB TR-11-01, Table 10-15). The rupture area is in this case the whole modelled Singö deformation zone in Figure 6.2 down to a depth of 15 km. Figure 6.4 shows that the stress increments are in the same order as the induced stresses during other long-term scenarios. During the M7 earthquake, however, tensile stresses may evolve that act in direction of Sh.

The modelling results show no pronounced fracture propagation in section N35W. The increase in total fracture length is the largest of all tested loading scenarios with 69.2% and 33.4% for the horizontal and vertical N55E sections, respectively. Fracture networks in the sections HZ and N55E show similar propagation behaviour with significant fracture growth dominated by Mode I in 85% of the cases for the horizontal section, and in 99% of the cases in section N55E, respectively. The simulation results for all horizontal DFN sections are shown in Figures 6.5 to 6.14. For the minor fracture propagation in the vertical N35W sections, two examples are shown in Figures 6.15 and 6.16. The results for the vertical N55E sections are shown in Figures 6.17 to 6.26.

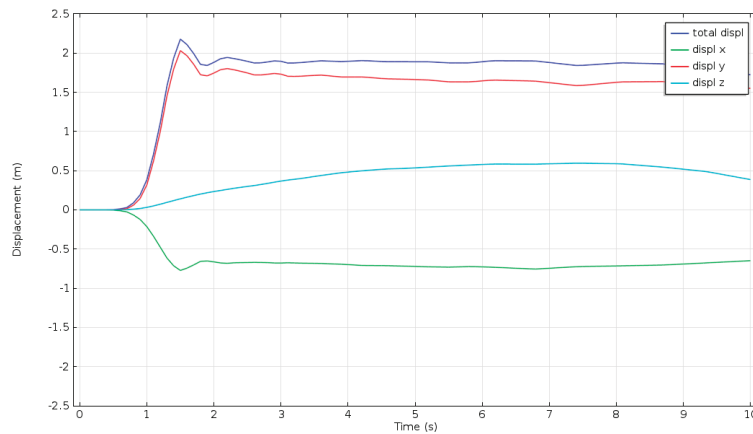


Figure 6.3. Displacements in the direction of the background principal stresses as monitored in the repository plane at 500 m depth (from Backers et al., 2014, SSM Technical Note 2014:58). x, y and z are the directions of SH, Sh and SV, respectively.

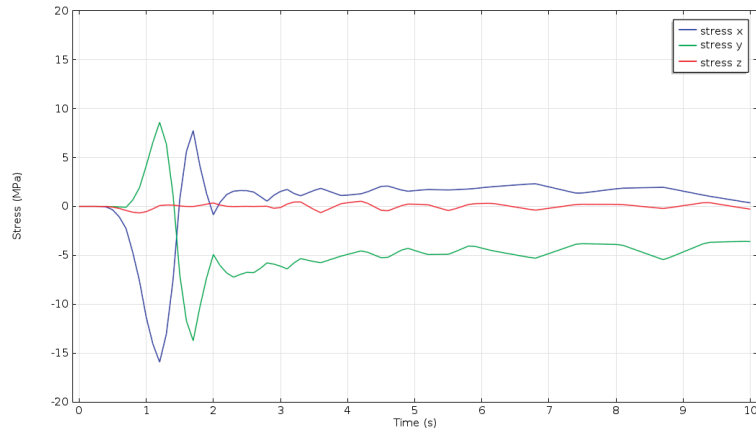


Figure 6.4. Stress increments in the direction of the background principal stresses as monitored in the repository plane at 500 m depth (from Backers et al., 2014, SSM Technical Note 2014:58). x, y and z are the directions of SH, Sh and SV, respectively.

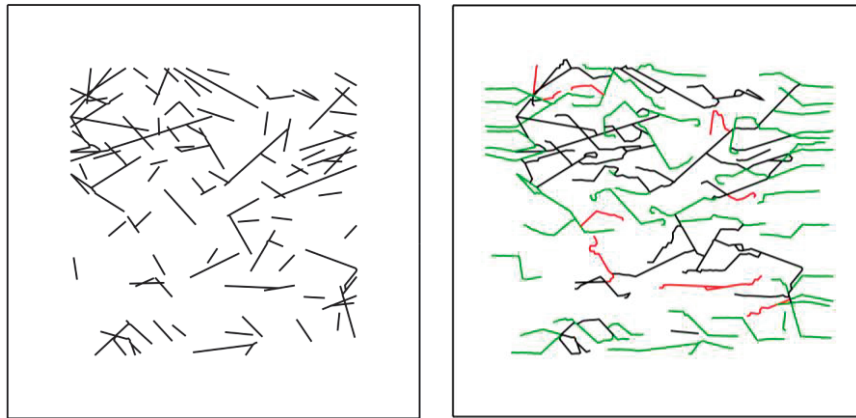


Figure 6.5. Horizontal section. (Left) Initial fracture geometry of FFM01geoDFNr0fixed01\_HZ2d (SH-Sh plane, SH is horizontal). (Right) Fracture propagation in the final simulation step 10. The initial total fracture length increases by 79.3%.

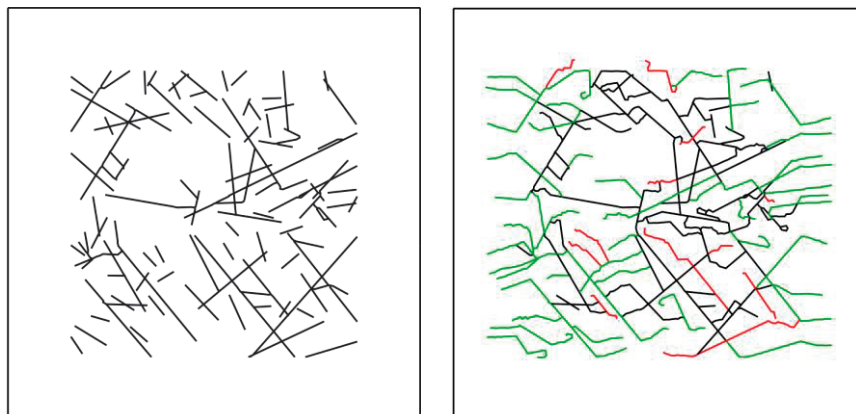


Figure 6.6. Horizontal section. (Left) Initial fracture geometry of FFM01geoDFNr0fixed02\_HZ2d (SH-Sh plane, SH is horizontal). (Right) Fracture propagation in the final simulation step 10. The initial total fracture length increases by 58.7%.

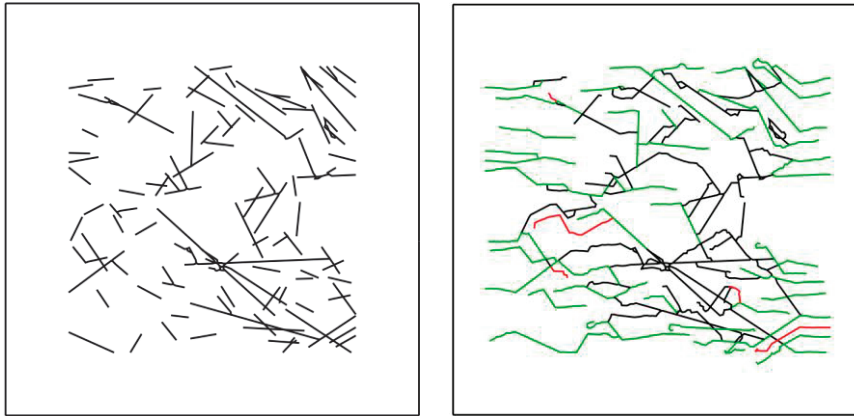


Figure 6.7. Horizontal section. (Left) Initial fracture geometry of FFM01geoDFNr0fixed03\_HZ2d (SH-Sh plane, SH is horizontal). (Right) Fracture propagation in the final simulation step 10. The initial total fracture length increases by 73.3%.

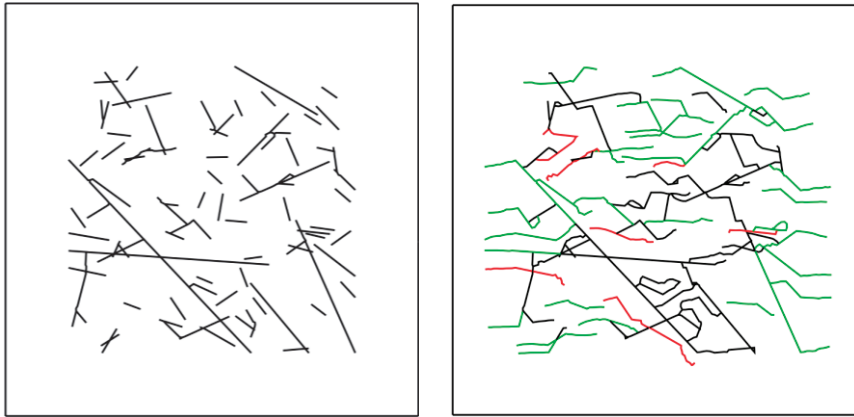


Figure 6.8. Horizontal section. (Left) Initial fracture geometry of FFM01geoDFNr0fixed04\_HZ2d (SH-Sh plane, SH is horizontal). (Right) Fracture propagation in the final simulation step 10. The initial total fracture length increases by 74.6%.

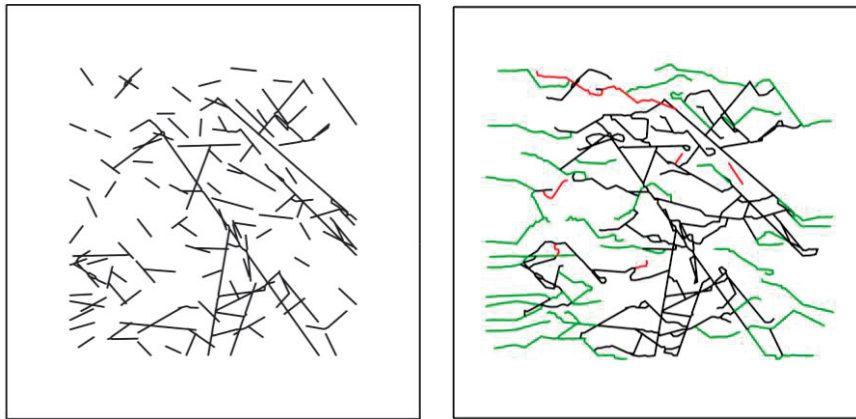


Figure 6.9. Horizontal section. (Left) Initial fracture geometry of FFM01geoDFNr0fixed05\_HZ2d (SH-Sh plane, SH is horizontal). (Right) Fracture propagation in the final simulation step 10. The initial total fracture length increases by 65.0%.

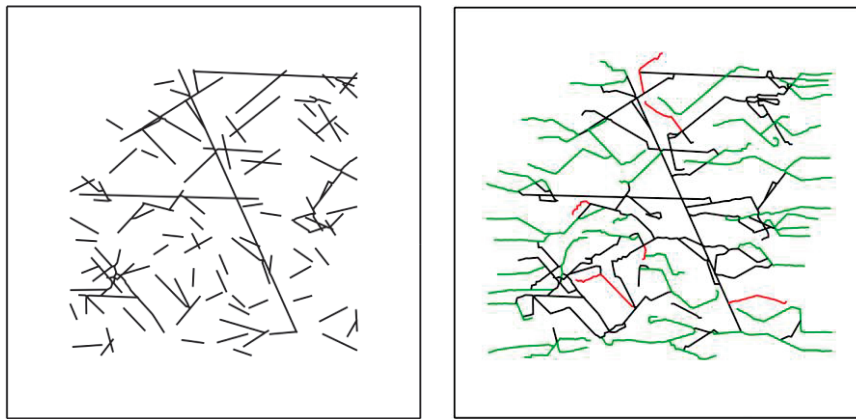


Figure 6.10. Horizontal section. (Left) Initial fracture geometry of FFM01geoDFNr0fixed06\_HZ2d (SH-Sh plane, SH is horizontal). (Right) Fracture propagation in the final simulation step 10. The initial total fracture length increases by 71.4%.

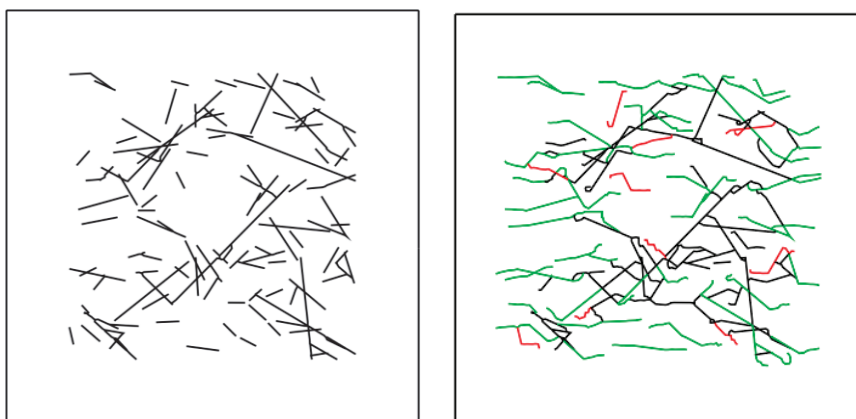


Figure 6.11. Horizontal section. (Left) Initial fracture geometry of FFM01geoDFNr0fixed07\_HZ2d (SH-Sh plane, SH is horizontal). (Right) Fracture propagation in the final simulation step 7. The initial total fracture length increases by 53.2%.

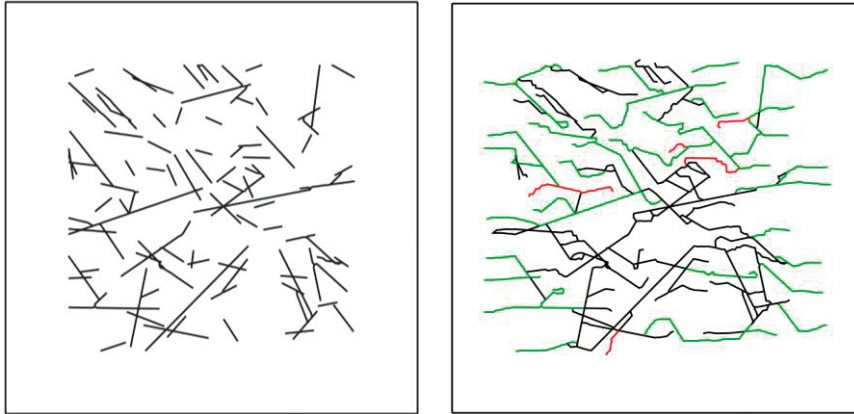


Figure 6.12. Horizontal section. (Left) Initial fracture geometry of FFM01geoDFNr0fixed08\_HZ2d (SH-Sh plane, SH is horizontal). (Right) Fracture propagation in the final simulation step 10. The initial total fracture length increases by 68.5%.

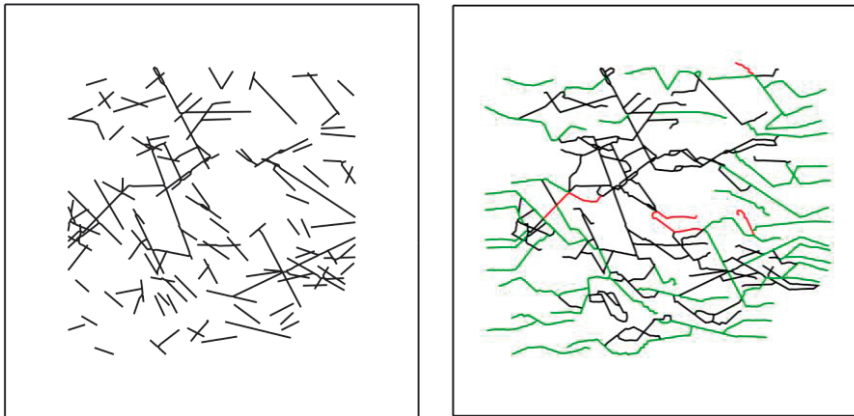


Figure 6.13. Horizontal section. (Left) Initial fracture geometry of FFM01geoDFNr0fixed09\_HZ2d (SH-Sh plane, SH is horizontal). (Right) Fracture propagation in the final simulation step 10. The initial total fracture length increases by 70.2%.

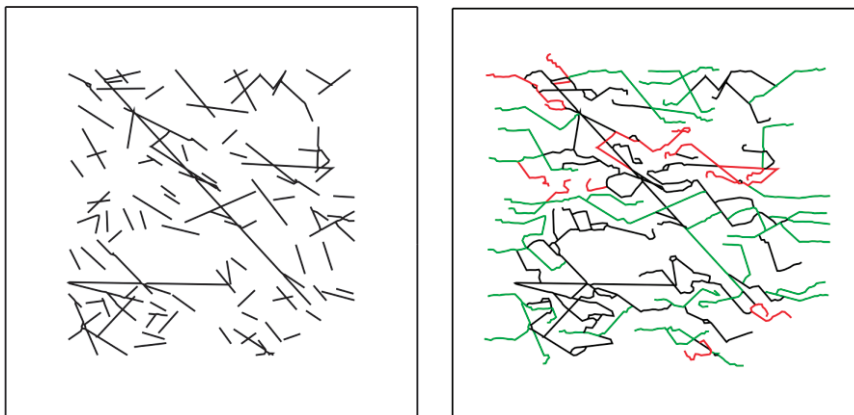


Figure 6.14. Horizontal section. (Left) Initial fracture geometry of FFM01geoDFNr0fixed10\_HZ2d (SH-Sh plane, SH is horizontal). (Right) Fracture propagation in the final simulation step 10. The initial total fracture length increases by 78.0%.



Figure 6.15. Vertical N35W section. (Left) Initial fracture geometry of FFM01geoDFNr0fixed06\_N35W2d (SH-SV plane, SH is horizontal). (Right) Fracture propagation in the final simulation step 10. The initial total fracture length increases by 2.1%.

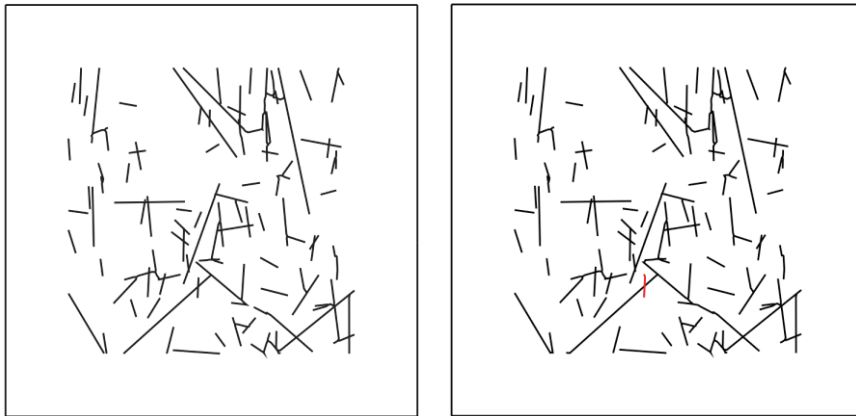


Figure 6.16. Vertical N35W section. (Left) Initial fracture geometry of FFM01geoDFNr0fixed08\_N35W2d (SH-SV plane, SH is horizontal). (Right) Fracture propagation in the final simulation step 4. The initial total fracture length increases by 0.5%.

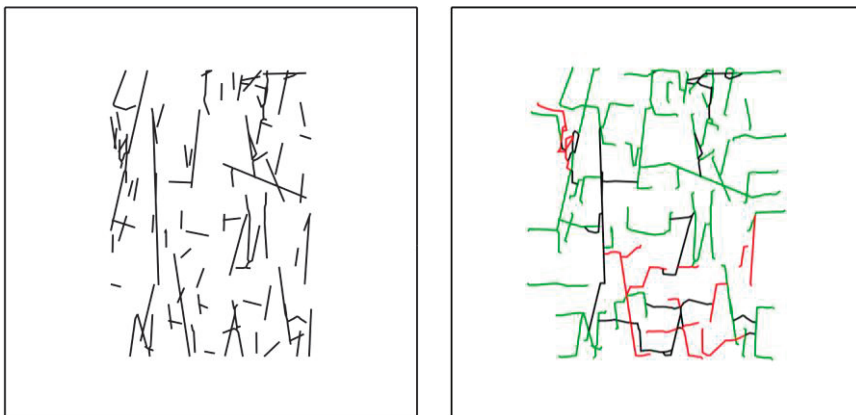


Figure 6.17. Vertical N55E section. (Left) Initial fracture geometry of FFM01geoDFNr0fixed01\_N55E2d (Sh-SV plane, Sh is horizontal). (Right) Fracture propagation in the final simulation step 10. The initial total fracture length increases by 42.4%.



Figure 6.18. Vertical N55E section. (Left) Initial fracture geometry of FFM01geoDFNr0fixed01\_N55E2d (Sh-SV plane, Sh is horizontal). (Right) Fracture propagation in the final simulation step 10. The initial total fracture length increases by 27.8%.

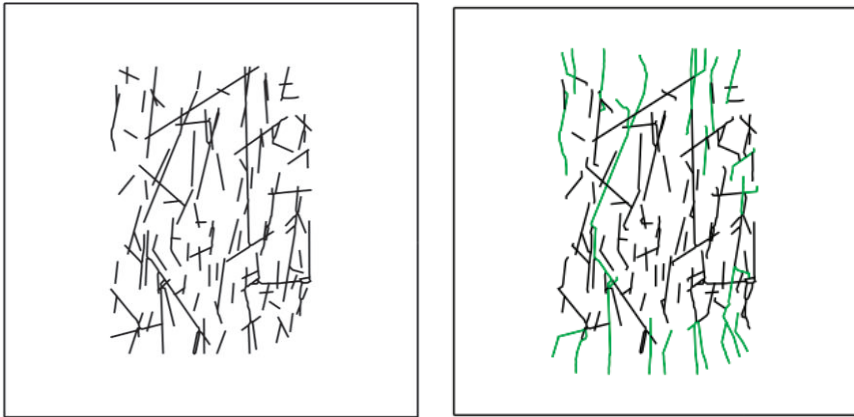


Figure 6.19. Vertical N55E section. (Left) Initial fracture geometry of FFM01geoDFNr0fixed03\_N55E2d (Sh-SV plane, Sh is horizontal). (Right) Fracture propagation in the final simulation step 7. The initial total fracture length increases by 20.0%.



Figure 6.20. Vertical N55E section. (Left) Initial fracture geometry of FFM01geoDFNr0fixed04\_N55E2d (Sh-SV plane, Sh is horizontal). (Right) Fracture propagation in the final simulation step 10. The initial total fracture length increases by 35.5%.

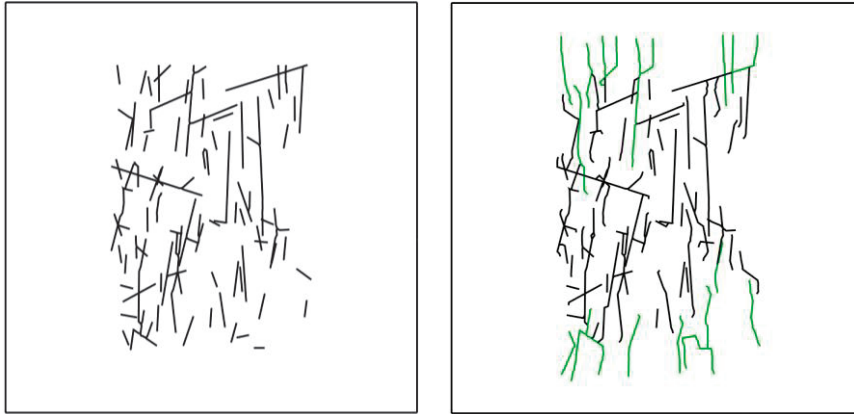


Figure 6.21. Vertical N55E section. (Left) Initial fracture geometry of FFM01geoDFNr0fixed05\_N55E2d (Sh-SV plane, Sh is horizontal). (Right) Fracture propagation in the final simulation step 10. The initial total fracture length increases by 38.5%.

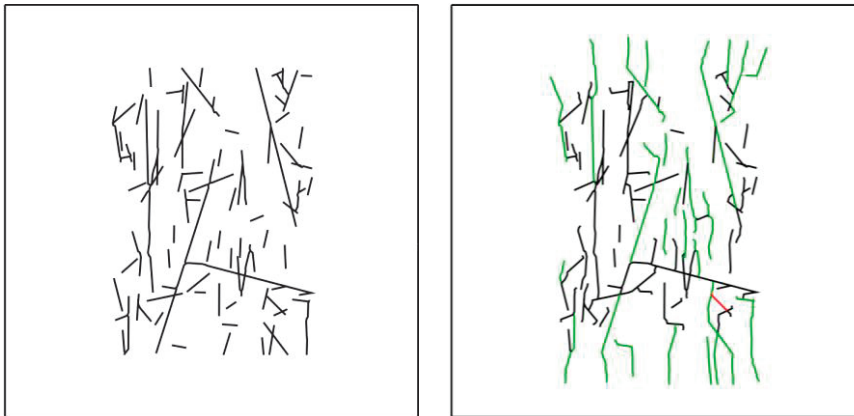


Figure 6.22. Vertical N55E section. (Left) Initial fracture geometry of FFM01geoDFNr0fixed06\_N55E2d (Sh-SV plane, Sh is horizontal). (Right) Fracture propagation in the final simulation step 10. The initial total fracture length increases by 37.3%.

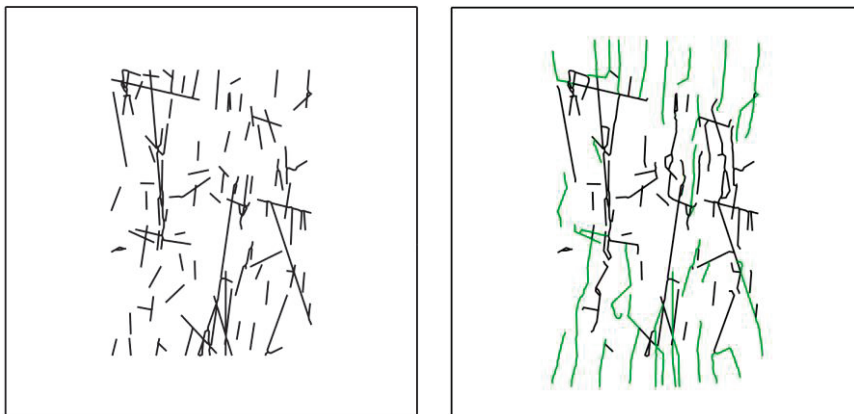


Figure 6.23. Vertical N55E section. (Left) Initial fracture geometry of FFM01geoDFNr0fixed07\_N55E2d (Sh-SV plane, Sh is horizontal). (Right) Fracture propagation in the final simulation step 10. The initial total fracture length increases by 44.5%.



Figure 6.24. Vertical N55E section. (Left) Initial fracture geometry of FFM01geoDFNr0fixed08\_N55E2d (Sh-SV plane, Sh is horizontal). (Right) Fracture propagation in the final simulation step 10. The initial total fracture length increases by 29.2%.



Figure 6.25. Vertical N55E section. (Left) Initial fracture geometry of FFM01geoDFNr0fixed09\_N55E2d (Sh-SV plane, Sh is horizontal). (Right) Fracture propagation in the final simulation step 10. The initial total fracture length increases by 29.4%.



Figure 6.26. Vertical N55E section. (Left) Initial fracture geometry of FFM01geoDFNr0fixed10\_N55E2d (Sh-SV plane, Sh is horizontal). (Right) Fracture propagation in the final simulation step 10. The initial total fracture length increases by 29.8%.

#### 6.2.4. Magnitude 6.0 proximal earthquake

The M6 proximal earthquake was simulated on the same deformation zone (Singö deformation zone) as the M7.0 event with decreased rupture area and average slip, resulting in an earthquake of moment magnitude 6. The stresses induced by this event are about one order of magnitude smaller than those from the M7.0 event (Figure 6.28).

Examples for the most unstable times in selected DFN realisations that experience the largest extent of fracture growth are shown in Figures 6.29 and 6.30. The overall fracture propagation is very little, the largest increase in total fracture length is observed for the horizontal section with 0.6% and an average number of propagation steps of 2.3.

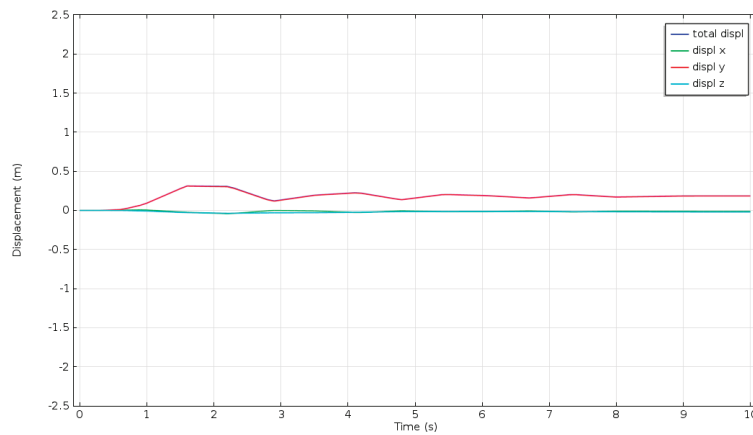


Figure 6.27. Displacements in the direction of the background principal stresses as monitored in the repository plane during the proximal M6 earthquake (green rupture area) and background stresses according to the #4 geomecon stress model (Backers et al., 2014, SSM Technical Note 2014:58).

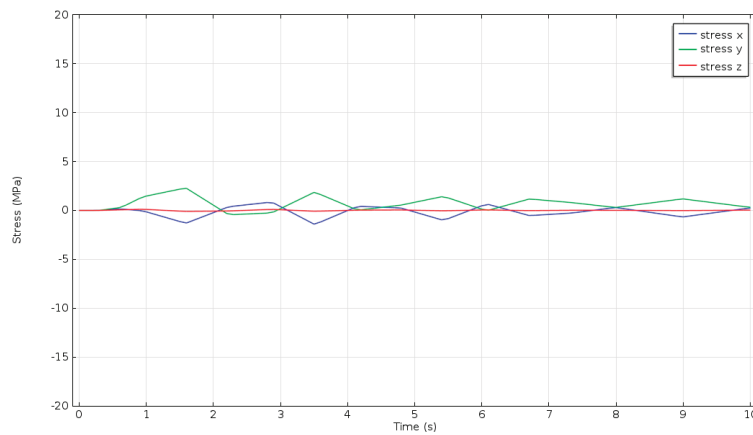


Figure 6.28. Stress increments in the direction of the background principal stresses as monitored in the repository plane during the proximal M6 earthquake (green rupture area) and background stresses according to the #4 geomecon stress model (Backers et al., 2014, SSM Technical Note 2014:58).

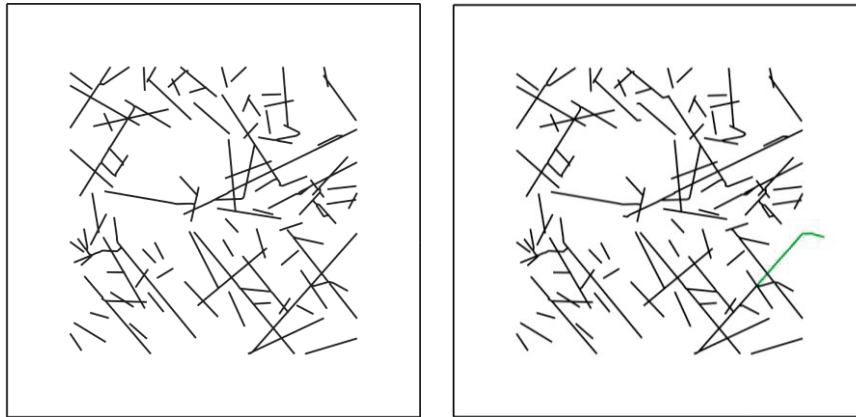


Figure 6.29. Horizontal section. (Left) Initial fracture geometry of FFM01geoDFNr0fixed02\_HZ2d (SH-Sh plane, SH is horizontal). (Right) Fracture propagation in the final simulation step 8. The initial total fracture length increases by 1.2%.

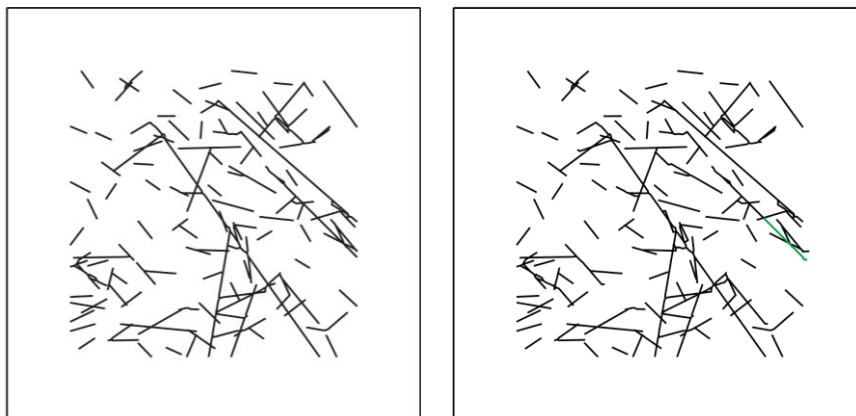


Figure 6.30. Horizontal section. (Left) Initial fracture geometry of FFM01geoDFNr0fixed05\_HZ2d (SH-Sh plane, SH is horizontal). (Right) Fracture propagation in the final simulation step 4. The initial total fracture length increasea by 1.6%.

### 6.2.5. Magnitude 6.0 distal earthquake

The distal earthquake of magnitude 6 was simulated to take place on the Forsmark deformation zone (Figure 6.2) and has a rupture area and average displacement similar to the proximal M6 earthquake. The stress increments observed in the repository show that the seismic wave arrives later than for the other events and that it has longer wavelengths of stress variations. The intensity of stress variations within the repository is somewhat smaller than for the proximal M6 event and a lot smaller than for the M7 event. The stress increments measured in the repository are in the order of 100 kPa and are therefore negligible.

### 6.2.6. Analysis of fault jump potential

In the course of previous assignment by SSM the potential of a fault jump at a fault T-termination was analysed by a combined Comsol and roxol approach (Backers et al, 2014, SSM Technical Note 2014:58, Section 5.3.4). The deformation zone geometry around the repository reveals one T-termination of large scale between deformation zone ZFMENE0060A and ZFMWNNW0123, where a potential fault jump could constitute a risk to the repository integrity. For the large scale analysis the geometry of the T-termination has been significantly simplified (Figure 6.31). This generalisation has the advantage of a future possible transfer to other localities where the risk of fault jump might be identified that would lead to extension of a zone into the repository. Therefore, the stress redistributions at the T-termination were investigated as they occur during the simulated earthquake of magnitude 7.

While in the previous analyses only the stress redistributions behind the T-termination were evaluated, we now consider the presence of DFNs in the critical area and evaluate fracture growth. Therefore, of the 11 different model geometries that were tested for the large scale assessment, we here use the model that resulted in the highest shear stresses around the T-termination (model No. 3, Figure 6.32).

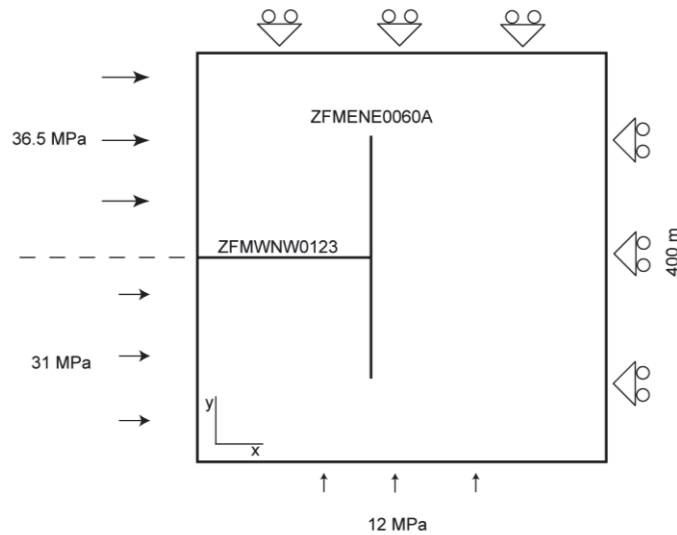


Figure 6.31. Boundary conditions for the T-termination analyses. The top and right sides of the model are defined as displacement boundaries (“roller boundaries”) while static stresses are applied on the bottom and left sides. Different stress conditions were assigned to the two segments of the left boundary on each side of deformation zone ZFMWNNW0123 as derived from the simulation of the M7 earthquake (Backers et al, 2014, SSM Technical Note 2014:58).

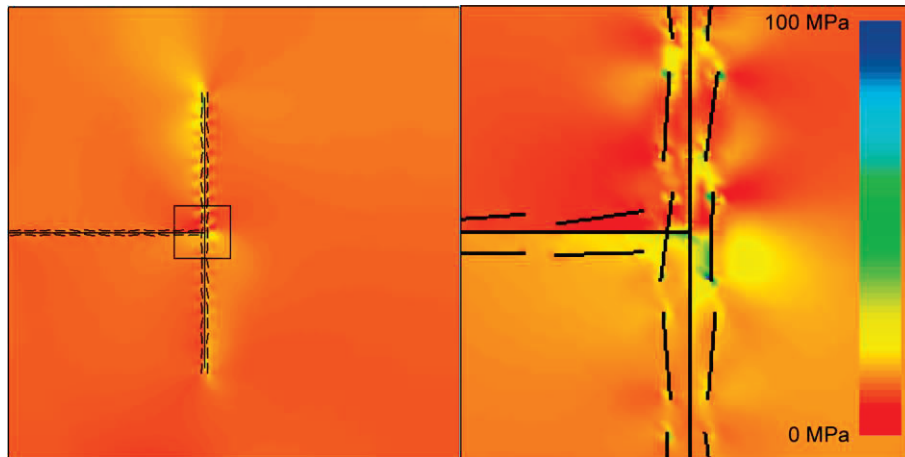


Figure 6.32. Fault jump model No. 3 from Backers et al. (2014, SSM Technical Note 2014:58, Section 5.3.4). The total model area is (200 m x 200 m). The insert in the left figure (50 m x 50 m) is magnified in the right figure. The maximum resulting shear stress around the T-junction is 20.3 MPa.

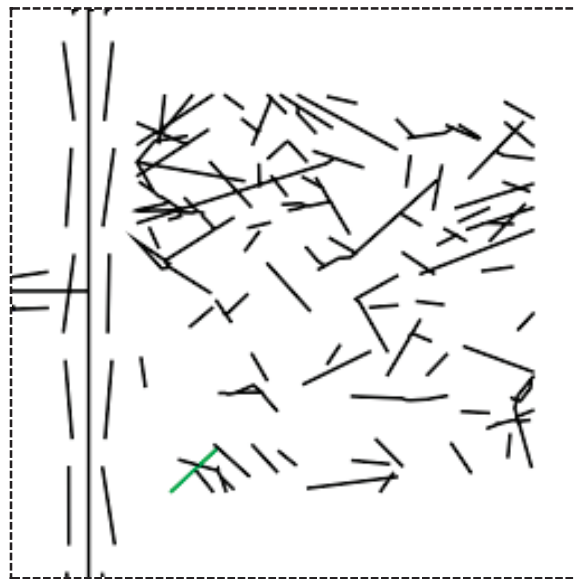


Figure 6.33. Horizontal section of the T-termination model with DFN FFM01geoDFNr0fixed01\_HZ2d. Fracture propagation in the final simulation step 1 is shown.

The maximum shear stress that occurs around the T-termination in model No. 3 is 20.3 MPa. The geometry of the zones involves the deformation zone cores modelled as single major fracture surrounded by a “transition zone” or fractured damage zone of 8 m width. The transition zone is represented by smaller fractures of 10 m length that are sub-parallel to the fault core. Figure 6.33 to 6.35 show examples of the roxol simulations. The simulation results of the T-termination show very little fracture growth. In general the DFNs reach stability within 1 simulation step and the total fracture length increase is 0.1%.

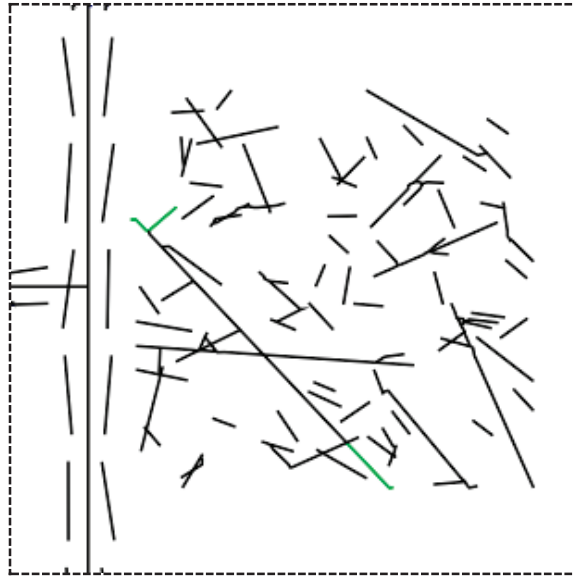


Figure 6.34. Horizontal section of the T-termination model with DFN FFM01geoDFNr0fixed04\_HZ2d. Fracture propagation in the final simulation step 2 is shown.

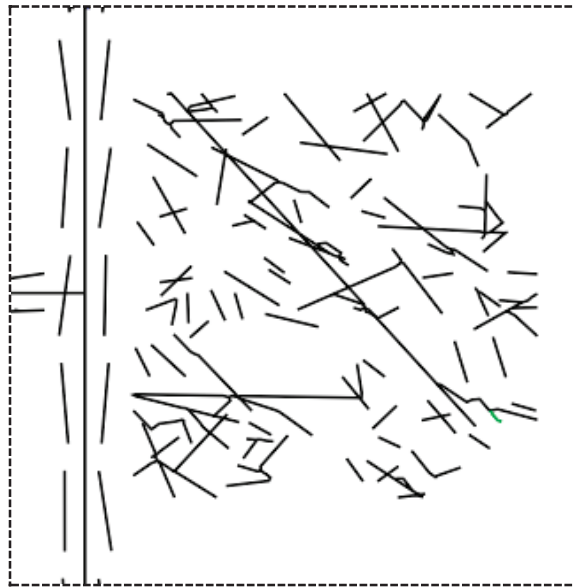


Figure 6.35. Horizontal section of the T-termination model with DFN FFM01geoDFNr0fixed10\_HZ2d. Fracture propagation in the final simulation step 2 is shown.

### 6.3. The Consultants' assessment of the influence of an earthquake on fracture growth

Simulations with two different earthquake magnitudes were used to estimate the stress changes that can affect the repository. The magnitude 6.0 earthquake produces stress changes that are only enough to cause minor fracture propagation that do not exceed an increase in total fracture length of about 1%. This is in line with analyses by SKB that came to the conclusion that earthquakes with magnitudes smaller than 6.0 do not represent a risk for the repository if current respect distances to deformation zones are kept (cf. Figure 6.1). Summarizing statistics of the fracture growth in the DFNs in the numerical simulations of earthquakes are shown in Table 6.3.

The simulation results for the magnitude 7.0 earthquake show that fracture growth occurs and the simulations cannot reach stability within the ten calculation steps for most of the analysed HZ and N55E sections. Since this is the most severe case for those sections, it can be concluded that the tensile stresses that potentially occur during an earthquake have the most pronounced impact on the fracture network. The fracture propagation in the N35W sections is limited and the tested DFNs reach stability after 2.7 simulation steps. In the planes N55E, which are subjected to  $S_h$  and  $S_v$ , it can be observed that tensile stresses lead the fracture propagation (Figure 6.17 to 6.26).

Overall, it can be concluded from those analyses that a magnitude 6.0 seismic event of the simulated type imposes a minor risk to the fracture network and the repository integrity, whereas a magnitude 7.0 seismic event imposes significant fracture extension and coalescence.

It needs to be emphasised here that the impact of seismic loads on the DFN is modelled as a static stress state extracted from a dynamic stress simulation. While it is today the only numerical way to carry out the analyses based on physical principles, it oversimplifies some aspects:

- a) The Comsol simulations of earthquakes on the regional deformation zones do not contain other large scale features than the Forsmark, Singö and Ekafjärden deformation zones. Therefore, there aren't other large scale geological features with low tensile strength in the models that can attenuate the seismic waves and limit the tensile component of the resulting stress at repository level. This results into tensile stresses in the direction of  $S_h$  that could be largely overestimated.
- b) The friction of the modelled fractures is static, whereas a dynamic friction would potentially be larger and stabilise and reduce extension of the fractures in the DFNs. This could be tested in future simulations by a parametric study of the friction coefficient or by introducing a toughening factor like increase in cohesion on the fracture frictional law.
- c) The fracture propagation criterion uses  $K_{IC}$  and  $K_{IIC}$  for fracture extension. This is appropriate for the onset of fracture extension, even under dynamic loads (Bertram, 2008). However, once the fractures will start propagating, they will accelerate under the dynamic load. During acceleration, the energy demand for further extension increases considerably (Bertram, 2008; Marder and Fineberg, 1996; Zhang et al., 1999), and therefore the fractures will tend to stabilise.

It would be of interest to evaluate certain parameter variations, especially the distance between the centre of the rupture area and the repository, the depth of the

rupture area, the orientation of the failure plane with respect to the principal stresses, as well as other faulting mechanisms than strike-slip.

The fault jump scenario results in minor fracture propagation. This is striking, considering that the simulations of the magnitude 7.0 event result in significant fracture propagation in the DFNs. It is necessary to further investigate this scenario with different stress conditions as they evolve during the magnitude 7.0 earthquake. Points in time when less stress difference between the two sides of deformation zone ZFMWNW0123, but larger stress difference between the principal stresses, could lead to more extensive fracture propagation around the T-junction between deformation zones.

Table 6.3. Statistics of the fracture propagation for the earthquake loading scenarios. The values are averaged over ten DFN realisations per section.

		Total length of new cracks	Relative crack length increase	Average propagation angle	Average Mode I	Average Mode II	No. of computation steps to stability
Model	Section	[m]	[%]	[°]	[%]	[%]	[-]
M6	HZ	4.2	0.6	41.9	94.2	5.8	2.3
	N35W	0.6	0.1	49.1	73.3	26.7	0.7
	N55E	0.1	0.0	36.6	100.0	0.0	0.3
M7	HZ	467.1	69.2	20.4	84.9	15.1	9.7
	N35W	3.6	0.5	46.4	89.2	10.8	2.7
	N55E	187.9	33.4	13.8	99.2	0.8	9.7
Fault jump	HZ	1.5	0.1	49.9	100.0	0.0	1.1

## 7. The Consultants' overall assessment on the likelihood and extent of fracture growth in the KBS-3 repository at Forsmark

In this study the Consultants have examined how the changes of in situ stresses that occur during different long-term scenarios affect the stability of the planned KBS-3 repository at Forsmark with respect to growth of the fracture network in the target volume. Thereby, an analytical evaluation preceded detailed numerical simulations of the different scenarios, thermal, glacial and seismic. The results of both approaches were compared and found to support each other. The main conclusions are:

- The present-day in-situ stress regime that builds the base for all analyses of fracture stability has a significant influence on the results. It is therefore vital to either verify the current models of the stress field or to conduct sensitivity analyses for different stress models and take the span of possible variation of the results into account.
- During the phase of thermally induced stresses there is some fracture propagation to be expected for fractures striking parallel to Sh (N35W section). This implies that some increase in hydraulic connectivity of the rock mass has to be expected. The simulations of the fractures in the other two sections show very limited fracture growth and reach stability after a few simulation steps.
- It has been shown in the literature that the fracture toughness  $K_{IIC}$  for loading Mode II increases with higher temperatures. This has a stabilising effect on the fracture network. The simulations conducted for the vertical N35W sections taking into account the temperature effect on fracture toughness showed a reduced total length of fracture growth by almost 70% compared with results for room-temperature fracture toughness.
- During a glacial cycle, the stages of maximum thickness of an ice sheet above the repository have a stabilising effect on the fracture network. Slightly increased fracture propagation will take place after the glacial maxima when the ice retreats and the vertical load is removed, but horizontal stresses are still elevated. The most critical state of stress for fracture propagation is however associated with a glacial forebulge.
- The stress increments that occur during an earthquake of magnitude 6.0 lead to minor fracture propagation in the horizontal plane and in the vertical SH-SV plane. The total fracture length of the tested DFNs increases by less than 1%.
- During an earthquake of magnitude 7.0, the horizontal and the vertical Sh-SV plane indicate elevated potential for fracture propagation and coalescence. The vertical SH-SV plane also shows fracture propagation, however, stabilising after total propagation lengths of about 0.5%. It can be expected that a seismic event of this order of magnitude initiated on a deformation zone around the Forsmark tectonic lens would affect the fracture network by increasing fracture density and hydraulic connectivity.

- The fault jump scenario at a T-termination between two deformation zones has been evaluated in the course of an earthquake. The assessments shows surprisingly little fracture propagation, considering that the simulations were carried out for the magnitude 7.0 seismic event that otherwise produces significant fracture propagation in the DFN models.

The nature of the employed models and the used methods impose certain limitations on the applicability of the results reported here. The most important ones are:

- The DFNs had to be simplified due to numerical limitations. The original DFNs contained numbers of fractures that cannot be handled by the employed code roxol. By ignoring only the smallest fractures up to a length of 3 m, the conservativeness of the model could be maintained, since the fracture stability usually correlates negatively with the fracture length.
- The most obvious constraint when applying roxol is that only 2D sections of the 3D DFN can be analysed. This might be an oversimplification in some cases. However, the most unstable cases should always be captured by this sort of analysis since one of the analysed sections will lie in the plane of maximum and minimum stress.
- The presence of other deformation zones than Forsmark, Singö and Eckafjärden in the Comsol models of seismic events could have limited the occurrence of tensile stresses during an earthquake in the vicinity of the repository.
- The earthquake induced stresses are measured in the direction of the present-day principal stresses while the actual principal stress direction will probably vary during an earthquake. Therefore, strictly speaking, differently oriented planes should be extracted from the 3D DFNs and tested with the actual principal stresses. Since these orientations will constantly vary with time during a seismic event, this cannot realistically be done with a 2D approach.
- The simulations analysing the influence of seismic event on DFN stability are considering static conditions only; i.e. a stress state originated by an earthquake is imposed to the DFN to see its evolution. The simulations do not consider: (a) dynamic friction laws for fractures, or (b) dynamic energy dissipating laws for accelerating fractures; both effects may be expected to reduce the amount of fracture growth.

The results presented here provide a good overall understanding of the stability of fractures during the long-term evolution of the repository for spent nuclear fuel at Forsmark. At the same time they show the areas where there is some need of further work for improving the understanding. In the course of the analyses the Authors found some issues that are worth to further pursue, like the uncertainty of input parameters for the considered glaciation scenario. Lund et al. (2009, SKB TR-09-15) present numerous glaciation models and Hökmark et al. (2010, SKB TR-10-23) expand on this by suggesting alternative pore pressure scenarios for the glaciation model. This is an area where certainly different loading histories could be tested.

An important field of further investigation is the measure of the impact of future large earthquakes on the repository. Not only is it necessary to test different earthquake magnitudes, but also to evaluate the influence of earthquakes generated by different faulting mechanisms. Other aspects that should be studied are the orientation of the seismogenic fault with respect to the principal stress directions, the dis-

tance of the rupture area to the repository, and the shear displacements on the seismogenic fault that lead to the generation of seismic waves. In addition, a parametric study with focus on the difference between static and dynamic of the mechanical properties would help understanding the dynamic effects of an earthquake.

The statistics of fracture propagation data for the loading scenarios in this report are summarised in Table 7.1. There are three scenarios that show fracture propagation that is likely to affect the strength of the rock mass and its permeability. Those are: (1) the thermal phase, (2) the glacial forebulge phase T3, and (3) the magnitude 7.0 earthquake. These are the scenarios where the increase in total fracture length is in the order of several percent of the initial fracture length. Another scenario where an increase of at least 1% is expected is the second glacial retreat scenario T5 where the total fracture length of the N35W section increases on average by 1.3%. The increase in total fracture length for all tested loading scenarios is shown as bar diagram in Figure 7.1.

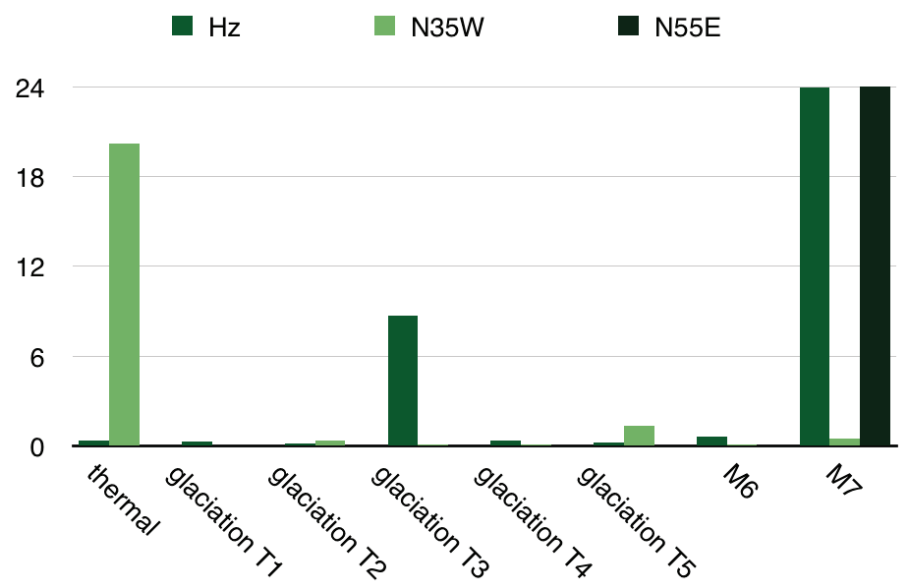


Figure 7.1. Relative increase in percentage of the total fracture length throughout the loading scenarios in this report.

Table 7.1. Summary of statistics of the fracture propagation for the loading scenarios in this report. The values are averaged over ten DFN realisations for every section (see also Appendix 5).

		Total length of new cracks	Increase in total fracture length	Average propagation angle	Average Mode I	Average Mode II	No. of computation steps to stability
Model	Section	[m]	[%]	[°]	[%]	[%]	[-]
Thermal	HZ	2.3	0.3	36	15	85	1.3
	N35W	135.2	20.2	28	19	81	10
	N55E	0.1	0.0	71	100	0	0.2
Increased $K_{IIC}$	N35W	44.8	6.6	29	33	67	9
Deposition holes	HZ	4.6	0.7	40.9	18.5	81.5	2.1
T1	HZ	1.9	0.3	33	33	67	1.7
	N35W	0.2	0.0	37	17	83	0.5
	N55E	0.1	0.0	54	50	50	0.2
T2	HZ	1.1	0.2	46	52	48	0.7
	N35W	2.7	0.3	45	83	17	1.9
	N55E	0.1	0.0	54	100	0	0.2
T3	HZ	59.1	8.7	24	94	6	9.5
	N35W	0.8	0.1	52	92	8	0.9
	N55E	0.0	0.0	54	100	0	0.2
T4	HZ	2.4	0.3	35	9	91	1.3
	N35W	0.5	0.1	30	0	100	0.9
	N55E	0.1	0.0	60	67	33	0.3
T5	HZ	1.4	0.2	37.7	37.5	62.5	1.2
	N35W	9.3	1.3	38.3	70.5	29.5	5.4
	N55E	0.1	0.0	53.6	100.0	0.0	0.4
M6 proximal	HZ	4.2	0.6	41.9	94.2	5.8	2.3
	N35W	0.6	0.1	49.1	73.3	26.7	0.7
	N55E	0.1	0.0	36.6	100.0	0.0	0.3
M7	HZ	467.1	69.2	20.4	84.9	15.1	9.7
	N35W	3.6	0.5	46.4	89.2	10.8	2.7
	N55E	187.9	33.4	13.8	99.2	0.8	9.7
Fault jump	HZ	1.5	0.1	49.9	100.0	0.0	1.1

## 8. References

- Atkinson, B K, 1991. Fracture Mechanics of Rock. Academic Press, London.
- Backers T, Stephansson O, Rybacki E, 2002. Rock fracture toughness testing in Mode II – punch-through shear test. International Journal of Rock Mechanics and Mining Sciences, 39, 755-769.
- Backers T, 2005. Fracture Toughness Determination and Micromechanics of Rock Under Mode I and Mode II Loading. Doctoral Thesis, University of Potsdam, Germany.
- Backers T, Antikainen J, Rinne M, 2006. Time dependent fracture growth in intact crystalline rock: laboratory procedures and results. In: GeoProc2006 – 2nd International Conference on Coupled T-H-M-C Processes in Geosystems: Fundamentals, Modelling, Experiments and Applications. HoHai University, Nanjing, pp. 261 - 266.
- Backers T. 2009. Fracture Mechanics Numerical Modeling – Potential and Examples of Applications in Rock Engineering. ROCKENG09. 3rd CANUS Rock Mechanics Symposium, Toronto, Canada
- Backers T, 2010. Applications of fracture mechanics numerical modelling in rock engineering. first break. Volume 28, issue 3, pages 13 - 22.
- Backers T, Stephansson O, 2011. The influence of temperature and fluid pressure on the fracture network evolution around deposition holes of a KBS-3V concept at Forsmark, Sweden. SSM Report number: 2011:26, ISSN: 2000-0456, Swedish Radiation Safety Authority (SSM).
- Backers T, Stephansson O. 2011a. Examples of application of fracture mechanical simulations in Geomechanics. 18. Tagung für Ingenieurgeologie und Forum Junge Ingenieurgeologen, Berlin, Germany
- Backers T, Gruehser C. 2012. Mechanische Aspekte des hydraulisch induzierten Risswachstums. Der Geothermiekongress. Karlsruhe, Germany
- Backers T, Gruehser C, Meier T and Dresen G. 2012. Fracture Pattern of Borehole Breakouts in Shale - Comparison of Physical and Numerical Experiments. EA-GE. Kopenhagen, Denmark
- Backers T, Meier T, Gipper P and Stephansson O, 2014. Rock Mechanics - Confidence of SKB's models for predicting the occurrence of spalling - Main Review Phase. SSM Technical Note 2014:10, Swedish Radiation Safety Authority (SSM).
- Backers T, Moeck I. 2014. Fault tips as favorable drilling targets for geothermal prospecting – a fracture mechanical perspective. World Geothermal Congress 2015, Melbourne, Australien.
- Backers T, Meier T, Gipper P, Stephansson O. 2014. Rock Mechanics - Assessing probability and extent of blind faults and fault-end growth around the KBS-3 repository at Forsmark – Main Review Phase, SSM Technical Note 2014:58, Swedish Radiation Safety Authority (SSM).

- Bertram A, 2008. Bruchenergie laufender Risse in Gestein. Dissertation. Ruhr-Universität Bochum.
- Damjanac B, Fairhurst C, 2010. Evidence for a long-term strength threshold in crystalline rock. *Rock Mechanics and Rock Engineering*, 43, doi: 10.1007/s00603-00010-00090-00609.
- Geier, J, 2014. Assessment of flows to deposition holes - Main Review Phase. SSM Technical Note 2014:05, Swedish Radiation Safety Authority (SSM).
- Ko T Y, Kemeny J, 2011. Subcritical crack growth in rocks under shear loading. *Journal of Geophysical Research*, Vol 116, B01407, doi:10.1029/2010JB000846.
- Lawn B, 1993. *Fracture of Brittle Solids*. Cambridge University Press, Cambridge.
- Marder M, Fineberg J, 1996. How Things Break. *Physics Today*: 24-29.
- Min K-B, Lee J, Stephansson O, 2013. Rock - Mechanics - Evolution of fracture transmissivity within different scenarios in SR-Site - Main Review Phase. SSM Technical Note 2013:37, ISSN: 2000-0456, Swedish Radiation Safety Authority (SSM).
- Mischo H, Backers T. 2012. Analysis of fracture coalescence by fracture mechanics simulation. EUROCK, Stockholm, Sweden
- Shen B, Stephansson O, Rinne M, Lee H-S, Jing L, Roshoff K, 2004. A fracture propagation code and its applications to nuclear waste disposal. *International Journal of Rock Mechanics and Mining Sciences*, 41, 448-449.
- SKB P-07-206. Ask D, Cornet F, Fontbonne F, 2007. Forsmark site investigation. Stress measurements with hydraulic methods in boreholes KFM07A, KFM07C, KFM08A, KFM09A and KFM09B. Svensk Kärnbränslehantering AB.
- SKB R-00-15. Andersson J, Ström A, Almén K-E, Ericsson LO, 2000. Vilka krav ställer djupförvaret på berget? Geovetenskapliga lämplighetsindikationer och kriterier för lokalisering och platsutvärdering. Svensk Kärnbränslehantering AB.
- SKB R-01-15. Munier R, Hermansson J, 2001. Metodik för geometrisk modellering. Presentation och administration av platsbeskrivande modeller. Svensk Kärnbränslehantering AB.
- SKB R-03-07. Munier R, Stenberg L, Stanfors R, Milnes A G, Hermansson J, Triumf C-A, 2003. Geological Site Descriptive Model. A strategy for the model development during site investigations. Svensk Kärnbränslehantering AB.
- SKB R-06-48. Fälth B, Höckmark H, 2006. Seismically induced slip on rock fractures. Results from dynamic discrete fracture modeling. Svensk Kärnbränslehantering AB.
- SKB R-07-26. Martin CD, 2007. Quantifying in situ stress magnitudes and orientations for Forsmark Design Step D2. Svensk Kärnbränslehantering AB.
- SKB R-07-45. Stephens M B, Fox A, La Pointe P, Simeonov A, Isaksson H, Hermansson J, Öhman J, 2007. Geology Forsmark. Site descriptive modelling Forsmark stage 2.2. Svensk Kärnbränslehantering AB.
- SKB R-07-46. Fox A, La Pointe P, Hermansson J, Öhman J, 2007. Statistical geological discrete fracture network model. Forsmark modelling stage 2.2. Svensk Kärnbränslehantering AB.
- SKB TR-97-07. La Pointe P, Wallmann P, Thomas A, Follin S, 1997. A methodology to estimate earthquake effects on fractures intersecting canister holes. Svensk Kärnbränslehantering AB.

- SKB TR-99-03. La Pointe P, Cladouhos T, Follin S, 1999. Calculation of displacements on fractures intersecting canisters induced by earthquakes: Aberg, Beberg and Ceberg examples. Svensk Kärnbränslehantering AB.
- SKB TR-00-08. La Pointe P, Cladouhos T, Outters N, Follin S, 2000. Evaluation of the conservativeness of the methodology for estimating earthquake-induced movements of fractures intersecting canisters. Svensk Kärnbränslehantering AB.
- SKB TR-08-05. Site description of Forsmark at completion of the site investigation phase. SDM-Site Forsmark, 2008. Svensk Kärnbränslehantering AB.
- SKB TR-08-11. Fälth B, Hökmark H, Munier R, 2010. Effects of large earthquakes on a KBS-3 repository. Evaluation of modelling results and their implications for layout and design. Svensk Kärnbränslehantering AB.
- SKB TR-09-15. Lund B, Schmidt P, Hieronymus C, 2009. Stress evolution and fault stability during the Weichselian glacial cycle. Svensk Kärnbränslehantering AB.
- SKB TR-10-23. Hökmark H, Lönnqvist M, Fälth B, 2010. THM-issues in repository rock. Thermal, mechanical, thermo-mechanical and hydromechanical evolution of the rock at the Forsmark and Laxemar sites. Svensk Kärnbränslehantering AB.
- SKB TR-10-52. Data report for the safety assessment SR-Site. Svensk Kärnbränslehantering AB.
- SKB TR-11-01. Long-term safety for the final repository for spent nuclear fuel at Forsmark. Main report of the SR-Site project. Svensk Kärnbränslehantering AB.
- Sukumar N, Prévost J-H, 2003. Modeling quasi-static crack growth with the extended finite element method Part I: Computer implementation. *International Journal of Solids and Structures*, 40, 7513–7537.
- Whittaker BN, Singh RN, Sun G, 1992. *Rock Fracture Mechanics - Principles, Design and Applications*, volume 72 of *Developements of Geotechnical Engineering*. Elsevier, Amsterdam - London - New York Tokyo, 1992.
- Zhang, Z.X., Kou, S.Q., Yu, J., Yu, Y., Jiang, L.G. & Lindqvist, P.A. 1999. Effects of loading rate on rock fracture. *Int. J. Rock Mech. Min. Sci.*; 36: 597-611.



# Coverage of SKB reports

Table A1.1. SKB reports covered in the assignment.

Reviewed report	Reviewed sections	Comments
SKB P-07-206. Forsmark site investigation. Stress measurements with hydraulic methods in boreholes KFM07A, KFM07C, KFM08A, KFM09A and KFM09B.	5.3, 5.4, 6, 7, 8	
SKB R-00-15. Vilka krav ställer djupförvaret på berget? Geovetenskapliga lämplighetsindikationer och kriterier för lokalisering och platsutvärdering.	Tabell 4-1	
SKB R-01-15. Metodik för geometrisk modellering. Presentation och administration av platsbeskrivande modeller.	3.1	
SKB R-03-07. Geological Site Descriptive Model. A strategy for the model development during site investigations.	2	
SKB R-06-48. Seismically induced slip on rock fractures. Results from dynamic discrete fracture modeling.	6	
SKB R-07-26. Quantifying in situ stress magnitudes and orientations for Forsmark Design Step D2.	complete report	
SKB R-07-45. Geology Forsmark. Site descriptive modeling Forsmark stage 2.2.	1, 2, 3, 5	
SKB R-07-46. Statistical geological discrete fracture network model. Forsmark modeling stage 2.2.	complete report	
SKB TR-97-07. A methodology to estimate earthquake effects on fractures intersecting canister holes.	complete report	

SKB TR-99-03. Calculation of displacements on fractures intersecting canisters induced by earthquakes: Aberg, Berg and Ceberg examples.	complete report
SKB TR-00-08. Evaluation of the conservativeness of the methodology for estimating earthquake-induced movements of fractures intersecting canisters.	complete report
SKB TR-08-05. Site description of Forsmark at completion of the site investigation phase. SDM-Site Forsmark, 2008.	2.2.2, 2.3, 6, 7, 11.3, 11.4
SKB TR-08-11. Effects of large earthquakes on a KBS-3 repository. Evaluation of modelling results and their implications for layout and design.	complete report
SKB TR-09-15. Lund B, Schmidt P, Hieronymus C, 2009. Stress evolution and fault stability during the Weichselian glacial cycle.	complete report
SKB TR-10-23. THM-issues in repository rock. Thermal, mechanical, thermo-mechanical and hydromechanical evolution of the rock at the Forsmark and Laxemar sites.	complete report
SKB TR-10-52. Data report for the safety assessment SR-Site.	6.4
SKB TR-11-01. Long-term safety for the final repository for spent nuclear fuel at Forsmark. Main report of the SR-Site project.	S1-S5, 4.3, 4.4, 4.5, 4.6, 10.2.2, 10.3.5, 10.4.4, 10.4.5 15.5.12

# Description of the Discrete Fracture Network used in this study

*Based on a note by Joel Geier (Clearwater Hardrock Consulting)*

The discrete-fracture network (DFN) approach is based on a conceptual model in which fractures are considered to be representable as a set of planar discontinuities, which can be characterized in terms of statistical distributions for their geometrical attributes. A wide variety of DFN conceptual models have been proposed in the scientific literature. The DFN models used in the present study follow SKB's approach (Fox et al., 2007, SB R-07-46) which makes use of DFN models consisting of disc-shaped fractures as proposed by Baecher et al. (1977), and characterized in terms of independent statistical distributions for the following fracture properties:

- Size (disc radius)
- Orientation (normal or pole vector)
- Transmissivity

Fracture centers are located randomly according to a Poisson process in 3-D space. The intensity of fracturing is characterized in terms of the total fracture area per unit volume,  $P_{32}$ , as defined by Dershowitz and Herda (1992).

Statistical models of this basic form are developed for each of several fracture sets in a given fracture domain. A fracture domain, by SKB's nomenclature, is considered to be a 3-D region of the rock within which the fracturing is homogeneous, in a statistical sense. A fracture set is generally defined (in the scientific literature) to be a set of fractures that have similar properties in terms of geometry as well as geological characteristics, but the fracture sets used in SKB's models are defined primarily based on fracture orientation. Fracture size (disc radius) in SKB's models is described by a power-law (Pareto) distribution, which is parameterized by an exponent  $k_r$  and a minimum radius  $r_0$ . Fracture orientation is described in terms of a Fisher distribution for fracture pole vectors, which is parameterized by the trend and plunge of a mean pole vector, and a parameter  $\kappa$  which is inversely related to the dispersion of fracture poles about the mean pole. Within a given fracture set, size and orientation are assumed to be statistically independent.

SKB's models are considered to apply for fractures (possibly including minor deformation zones as well as single, discrete fractures) with a length scale smaller than 1 km. In terms of disc-shaped fractures, a 1 km x 1 km square fracture has approximately the same surface area as a disc-shaped fracture of radius 564.2 m, so this is used as the upper bound for simulating values of fracture radius.

Fracture intensity ( $P_{32}$ ) has been assessed by SKB mainly on the basis of the frequency of fractures in core-drilled holes. For the rock volume at repository depth, the main source of data is drill holes that are close to vertical, which implies good sampling of fractures that are close to horizontal, but poor sampling of fractures that are close to vertical. Theoretical corrections for this sampling bias have been applied by SKB to produce estimates of the volumetric measure of fracture intensity,  $P_{32}$ . However, for fractures that are close to vertical, these corrections are sensitive to the geometrical assumptions that are implicit to the theoretical corrections (e.g. planar rather than undulating fractures, and equidimensional rather than elongated fractures). For the subset of fractures that conduct water, estimates of  $P_{32}$  by SKB have been derived by calibration of a DFN flow model based on flowmeter logging data. For the present simulations, these estimates of “conductive”  $P_{32}$  are represented by the “hydro [geological]” fracture sets based on data from Selroos and Follin (2009), with the remaining  $P_{32}$  assigned to fracture sets which are assumed to be “tight,” with minimal fracture transmissivity.

For the present study, stochastic realizations of the DFN model are generated by simulation, using a different seed value for the random number generator to produce each realization. Parameters for the fracture sets are taken directly from SKB's Geo-DFN model for Fracture Domain FFM01 ( $r_0$ -fixed variant) as given by Munier (2010, SKB TR 10-21, Appendix 3, Table A3.1). The derivation of this model by SKB is described in detail by Fox et al. (2007). Fracture orientation statistics (trend and plunge of the mean pole vector, and Fisher concentration parameter  $\kappa$ ) are obtained by fitting to data for fracture orientations measured in core-drilled holes, using the hard-sector method of the FracMan code as described by Dershowitz et al. (2004).

For hydrogeomechanical modelling, an initial value of transmissivity for fractures could be required. SKB's Geo-DFN model does not specify transmissivities. Transmissivity distributions are specified for the fracture sets in SKB's Hydro-DFN model. The Hydro-DFN sets are here treated as subsets of the corresponding Geo-DFN sets, representing only a fraction of the fracture intensity ( $P_{32}$ ) of the Geo-DFN sets.

Fracture sets labeled as “hydro” in Table 1 represent the subsets of the respective sets that are considered to have non-negligible transmissivity in SKB's Hydro-DFN model. The remaining fractions of these sets are labelled as “tight.” SKB's definition of the Geo-DFN model does not include hydrogeological parameterization (fracture transmissivity, etc.). For all of the sets labeled as “hydro” in Table A2-1, transmissivity is related to fracture radius according to the “semi-correlated” model for the corresponding fracture set in the Hydro-DFN model (SKB R-09-22 Table 2-2 of Selroos and Follin, 2009), for the case of  $z < -400$  m. The semi correlated model for transmissivity  $T$  vs. fracture radius  $r$  is defined as:

$$T = \exp[\log \bar{y} + b \log r + \sigma N] = \bar{y} r^b 10^{\sigma_{10} N} \quad \text{Eq. (A.1)}$$

where  $b$ ,  $\bar{y}$ , and  $\sigma_{10}$  are correlation parameters representing the logarithmic slope, the intercept value, and scatter about the fitted logarithmic trend, respectively,  $N$  is the truncated normal distribution  $N(0,1)$  on the interval  $[-2,2]$ ,  $\sigma = \sigma_{10} \log(10)$ , and  $\log$  denotes the natural logarithm.

The fracture realizations and extraction of 2-D datasets for the hydrogeomechanical simulations are carried out in a single Linux C-shell script for each calculation case, in the following steps for each realization:

1. Generation of the fracture realization.
2. Conversion of the resulting (thinned) set of hexagonal fractures to disks (not used directly for the production of these datasets, but used to simplify checks of the statistical properties of the fracture population);
3. Identification of fractures that cross a vertical plane striking N35W, using the DFM module dfmslice v. 2.4.1.1.
4. Identification of fractures that cross a vertical plane striking N55E, using the DFM module dfmslice v. 2.4.1.1.
5. Identification of fractures that cross a horizontal plane at  $z = -468$  m and extraction fracture traces on that plane, using the DFM module dfmslice v. 2.4.1.1.
6. Further processing of the 2-D cross-section data to the format requested by SNU.

For the r0-fixed base case these steps are carried out by the following Linux C-shell script:

### run fracgen batch v2

```
run_fracgen_batch_v2
#!/bin/csh -f
#
set STEM = "FFM01geoDFNr0fixed"
foreach N ( 01 02 03 04 05 06 07 08 09 10 )
    set NAME = "${STEM}${N}"
    SRSite_r0fixed_fracgen_v2 $STEM $N
    awk -f hexpanel_disks.awk -v OPT=DIP ${NAME}_fracs.pan > ${NAME}_disks.prn
    dfmslice2411 -p ${NAME}_fracs.pan -x XsectionN35W_50m.pan > ${NAME}_N35W.prn
    dfmslice2411 -p ${NAME}_fracs.pan -x XsectionN55E_50m.pan > ${NAME}_N55E.prn
    dfmslice2411 -p ${NAME}_fracs.pan -x XsectionHZ_50m.pan > ${NAME}_HZ.prn
    awk -f process2dsection.awk ${NAME}_N55E.prn ${NAME}_disks.prn > ${NAME}_N55E2d.prn
    awk -f process2dsection.awk ${NAME}_N35W.prn ${NAME}_disks.prn > ${NAME}_N35W2d.prn
    awk -f process2dsection.awk ${NAME}_HZ.prn ${NAME}_disks.prn > ${NAME}_HZ2d.prn
end
```

For the r0-fixed case with elevated P32 these steps are carried out by a similar script:

### run fracgen batch Pelev v2

```
#!/bin/csh -f
#
set STEM = "FFM01geoDFNr0Pelev"
foreach N ( 01 02 03 04 05 06 07 08 09 10 )
    set NAME = "${STEM}${N}"
    SRSite_r0fixed_fracgen_v2_Pelev $STEM $N
    awk -f hexpanel_disks.awk -v OPT=DIP ${NAME}_fracs.pan > ${NAME}_disks.prn
    dfmslice2411 -p ${NAME}_fracs.pan -x XsectionN35W_50m.pan > ${NAME}_N35W.prn
    dfmslice2411 -p ${NAME}_fracs.pan -x XsectionN55E_50m.pan > ${NAME}_N55E.prn
    dfmslice2411 -p ${NAME}_fracs.pan -x XsectionHZ_50m.pan > ${NAME}_HZ.prn
    awk -f process2dsection.awk ${NAME}_N55E.prn ${NAME}_disks.prn > ${NAME}_N55E2d.prn
    awk -f process2dsection.awk ${NAME}_N35W.prn ${NAME}_disks.prn > ${NAME}_N35W2d.prn
    awk -f process2dsection.awk ${NAME}_HZ.prn ${NAME}_disks.prn > ${NAME}_HZ2d.prn
end
```

The source files for these calculations are contained in the directory:

~/Desktop/modelling/GeoDFNsimulations

An auxiliary directory with identical setup:

~/Desktop/modelling/GeoDFNsimulations2

was used to run some of the realizations for the elevated  $P_{32}$  case in parallel.

Table A2-1. Geometric parameters for generation of fracture sets for the r0-fixed base case for the Geo-DFN simulations for hydrogeomechanical modelling. Note that the specified maximum radius  $r_{max}$  is larger than an effective value which is a function of limited resolution of the simulation algorithm and the specified value of the minimum radius  $r_{min}$ , as discussed later in this memorandum.

FFM01	Mean pole trend (°)	Mean pole plunge (°)	Fisher concent- ration $\kappa$	$r_0$	$k_r$	$P_{32}$ ( $m^2/m^3$ ) (unscaled)	$r_{min}$ (m)	$r_{max}$ (m)
NE global (hydro)	314.9	1.3	20.94	0.039	2.72	0.193	0.3	564.2
NS global (hydro)	270.1	5.3	21.34	0.039	2.75	0.122	0.3	564.2
NW global (hydro)	230.1	4.6	15.70	0.039	2.61	0.100	0.3	564.2
SH global (hydro)	0.8	87.3	17.42	0.039	2.58	0.158	0.3	564.2
EW local (hydro)	0.4	11.9	13.89	0.039	2.93	0.105	0.3	564.2
NE global (tight)	314.9	1.3	20.94	0.039	2.72	1.540	0.3	564.2
NS global (tight)	270.1	5.3	21.34	0.039	2.75	1.170	0.3	564.2
NW global (tight)	230.1	4.6	15.70	0.039	2.61	0.848	0.3	564.2
SH global (tight)	0.8	87.3	17.42	0.039	2.58	0.466	0.3	564.2
ENE local	157.5	3.1	34.11	0.039	2.97	0.256	0.3	564.2
EW local (tight)	0.4	11.9	13.89	0.039	2.93	0.064	0.3	564.2
NNE local	293.8	0.0	21.79	0.039	3.00	0.658	0.3	564.2
SH2 local	164.0	52.6	35.43	0.039	2.61	0.081	0.3	564.2
SH3 local	337.9	52.9	17.08	0.039	2.61	0.067	0.3	564.2

The values of the correlation parameters used for the “hydro” sets in this data delivery are:

$$b = 0.5$$

$$\bar{y} = 5.3e^{-11} m^2/s$$

$$\sigma_{10} = 1.0$$

For the other fracture sets (those not labeled as “hydro” in Table 1), the fracture transmissivity is set to an arbitrary low, constant value:

$$T = 10^{-13} m^2/s$$

In order to consider the variability of connectivity, fracture intensity ( $P_{32}$ ) has been increased by 20% for all fracture sets. This increase is justified based on the recommendation of Fox et al. (2007) to consider  $P_{32}$

As a stochastic variable, distributed as a gamma distribution. Fox et al. (2007, SKB R-07-46) suggested a gamma distribution as a model for variability in  $P_{32}$  for the GeoDFN (on a 30 m scale for most fracture sets).

The quantiles of the gamma distribution with shape parameter  $\alpha$  and scale parameter  $\beta$  can be calculated by solving:

$$P(\alpha, P_{32}/\beta) = p \quad \text{Eq. (A.2)}$$

In terms of  $P_{32}$  for a given quantile  $p$ , and where  $P(\alpha, x)$  is the normalized incomplete gamma function  $\gamma(\alpha, x)/\Gamma(\alpha)$ .

For fracture domain FFM01, using 60th percentile values for each fracture set results in an 18% increase in total  $P_{32}$  compared with the median (50%) values. Thus (using round values), a 20% increase in total  $P_{32}$  is a reasonable variation to consider.

### A2.1 Quality Check 1: Comparison of expected and simulated $P_{32}$ fracture intensity as a function of fracture radius

This quality check is based on the increments of  $P_{32}$ , the fracture intensity per unit volume, for a given range of fracture radii  $[r1, r2]$ . For brevity these increments are referred to as  $P_{32} [r1, r2]$ . It may be noted that the overall fracture intensity  $P_{32} [0, \infty]$  is obtained as a particular case.

The DFN realizations for these calculation cases use selective thinning of fractures outside of sphere of 44 m radius of (0, 0, -468 m), which is the center the 50 m cubical region for which results are provided, bounded by (-25 m, -25 m, -493 m) and (25 m, 25 m, -443 m). The 44 m radius is chosen to be slightly larger than the diagonal distance from the center of the cube to its corners:

$$\sqrt{3} \cdot 25\text{m} \approx 43.3\text{m}$$

Outside of this sphere, smaller fractures are deleted as a function of fracture radius, in order to minimize the number of fractures to be stored, while ensuring that all fractures within the 50 m cubical region are preserved. Therefore the check of  $P_{32} [r1, r2]$  is based only on the volume within this 50 m cube.

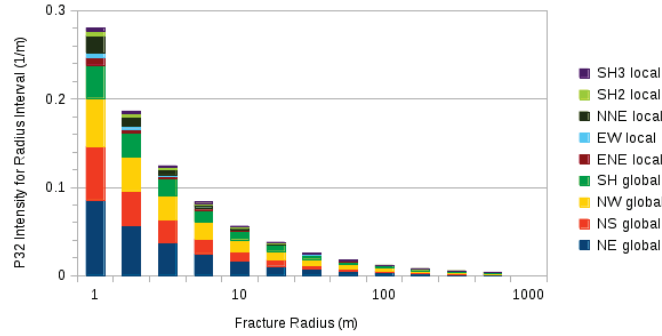
The results for realizations 01-04 of the r0-fixed base case are plotted in Figures 1 and 2, and for the realizations 01-04 of the elevated- $P_{32}$  variant in Figures 3 and 4. In each figure, the top graph shows the expected distribution while the lower two graphs give the simulated results. The bars represent  $P_{32} [r1, r2]$  for increments of a quarter order of magnitude in fracture (equivalent) radius. Note that fractures of  $r < 0.3$  m have been omitted from the stochastic realizations, so only fractures in size ranges beginning with (10-0.25 m, 1 m)  $\approx$  (0.56 m, 1 m) are shown for comparison.

For the fracture sets that are divided into “hydro” and “tight” subsets, the theoretical distribution has been plotted only for the combination of these subsets. This way the same theoretical distribution as calculated for the Geo-DFN model used in other geomechanical calculations can be used. In the plots of simulated data, a lighter shade of the same color is used to distinguish the “tight” subset vs. the “hydro” subset.

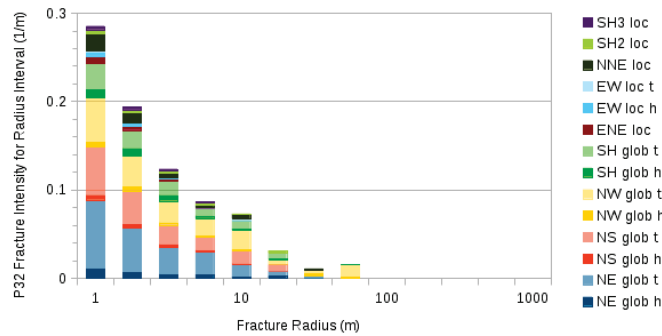
It can be seen that there is visually very good agreement both in terms of total fracture intensity and the fracture intensity for individual fracture sets. The exceptions are (1) for size ranges with approaching the dimension of the 50 m cube, where stochastic effects due to the large impact of individual fractures on the increments of  $P_{32}$  are apparent, and (2) for size ranges with  $r$  larger than 56.2 m, for which no fractures occur in these realizations.

Table 2 gives the numerical values of simulated  $P_{32}$  for each of the fracture radius ranges larger than  $r_{min}$ , compared with the theoretical values of  $P_{32}$  for the same ranges. It can be seen that the average total simulated  $P_{32}$  (the average of the sum over all fracture sets) is slightly higher than the theoretical value for all of the size ranges except for the ranges 10 m to 17.8 m and 17.8 m to 31.6m. However the average total simulated  $P_{32}$  is within one standard deviation of the theoretical value, for all except the smallest size ranges (fracture radius less than 3.16 m).

a) Theoretical distribution



b) Simulated distribution (Realization 01)



c) Simulated distribution (Realization 02)

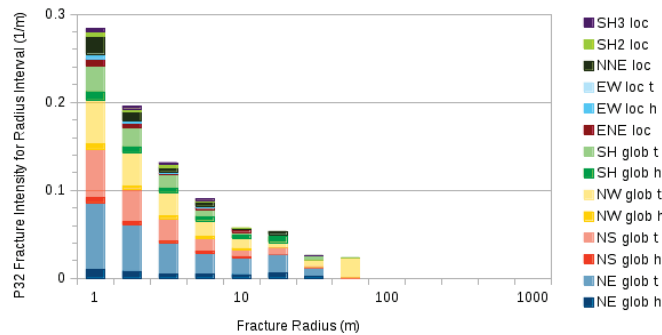
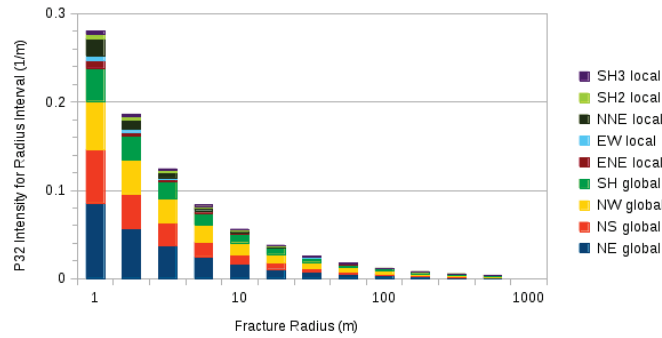
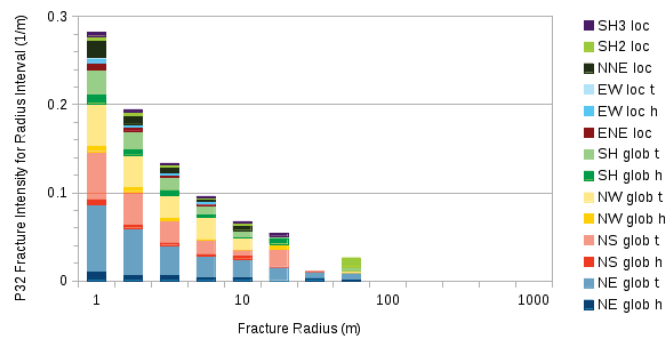


Figure A2-1. Comparison of theoretical and simulated increments of  $P_{32}$  fracture intensity for each of the fracture sets in the r0-fixed base case, for realizations 01 and 02. Abbreviations in the legend are: glob = global, loc = local, h = hydro, and t = tight. Each histogram bar represents  $\frac{1}{4}$  order of magnitude range of fracture radius, and is labeled based on the maximum radius in the interval.

a) Theoretical distribution



b) Simulated distribution (Realization 03)



c) Simulated distribution (Realization 04)

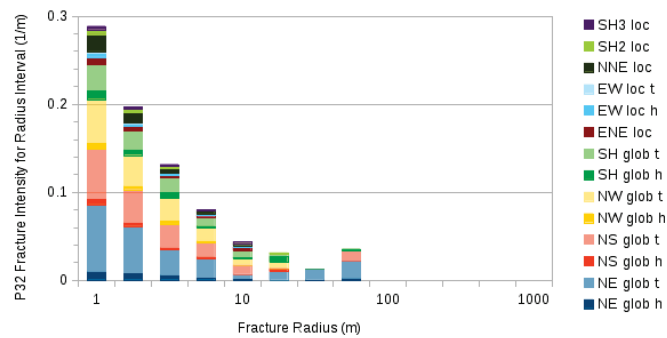
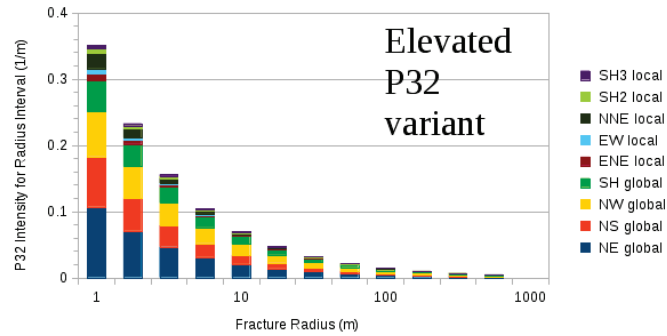
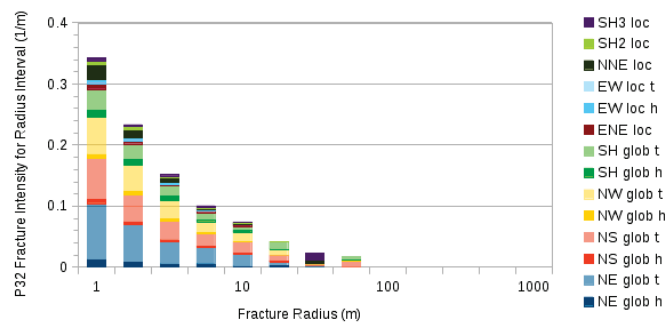


Figure A2-2. Comparison of theoretical and simulated increments of  $P_{32}$  fracture intensity for each of the fracture sets in the r0-fixed base case, for realizations 03 and 04. Abbreviations in the legend are: glob = global, loc = local, h = hydro, and t = tight. Each histogram bar represents  $\frac{1}{4}$  order of magnitude range of fracture radius, and is labeled based on the maximum radius in the interval.

a) Theoretical distribution



b) Simulated distribution (Realization 01)



c) Simulated distribution (Realization 02)

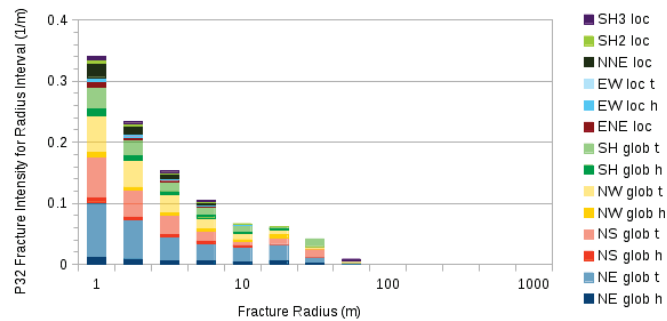
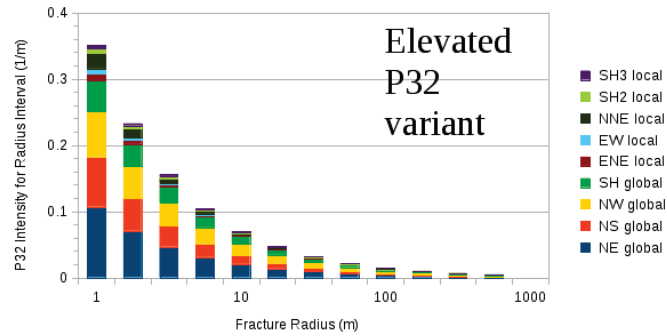
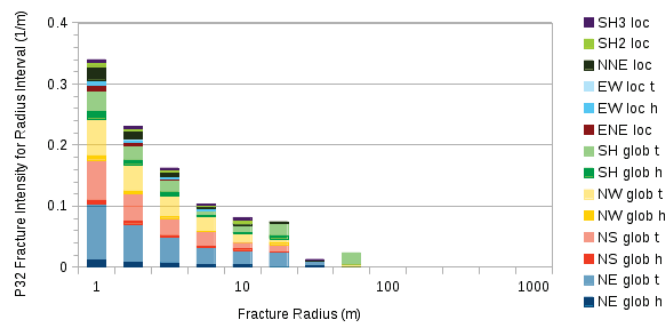


Figure A2-3. Comparison of theoretical and simulated increments of  $P_{32}$  fracture intensity for each of the fracture sets in the elevated- $P_{32}$  variant of the r0-fixed model, for realizations 01 and 02. Abbreviations in the legend are: glob = global, loc = local, h = hydro, and t = tight. Each histogram bar represents  $\frac{1}{4}$  order of magnitude range of fracture radius, and is labeled based on the maximum radius in the interval.

a) Theoretical distribution



b) Simulated distribution (Realization 03)



c) Simulated distribution (Realization 04)

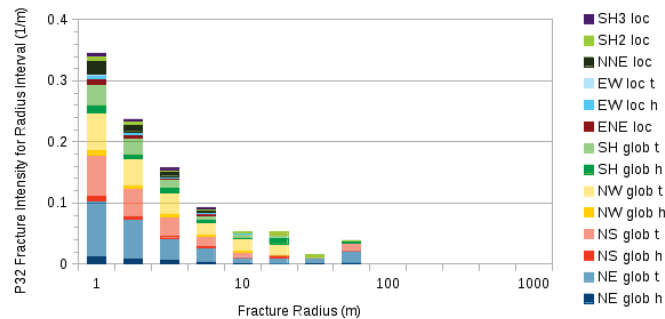


Figure A2-4. Comparison of theoretical and simulated increments of  $P_{32}$  fracture intensity for each of the fracture sets in the elevated- $P_{32}$  variant of the r0-fixed model, for realizations 03 and 04. Abbreviations in the legend are: glob = global, loc = local, h = hydro, and t = tight. Each histogram bar represents  $\frac{1}{4}$  order of magnitude range of fracture radius, and is labeled based on the maximum radius in the interval.

Table A2-2. Theoretical (theo) versus average (avg), standard deviation (std), minimum (min), and maximum (max) values of simulated  $P_{32}$  increments for 10 realizations of the  $r_0$ -fixed base case for fracture radius  $[r_1, r_2]$ . For the largest four ranges of fracture radius, no fractures were generated in any of the 10 realizations, so this is indicated just by listing the zero values for the maximum  $P_{32}$ .

$r_1$ (m)	$r_2$ (m)		Total $P_{32}$ (L/m)	NE global hydro	NS global hydro	NW global hydro	SH global hydro	EW local hydro	NE global tight	NS global tight	NW global tight	SH global tight	ENE local	EW local tight	NNE local	SH2 local	SH3 local
0.3	0.32	theo	0.0488	0.0017	0.0010	0.0009	0.0015	0.0008	0.0132	0.0098	0.0077	0.0043	0.0018	0.0005	0.0044	0.0007	0.0006
		avg	0.0460	0.0016	0.0010	0.0009	0.0014	0.0007	0.0125	0.0092	0.0073	0.0041	0.0017	0.0004	0.0041	0.0007	0.0006
		std	0.0002	0.0001	0.0001	0.0001	0.0001	0.0000	0.0001	0.0002	0.0001	0.0001	0.0001	0.0000	0.0001	0.0000	0.0000
		min	0.0457	0.0014	0.0009	0.0008	0.0013	0.0007	0.0123	0.0089	0.0071	0.0040	0.0016	0.0004	0.0040	0.0007	0.0005
		max	0.0464	0.0017	0.0010	0.0010	0.0015	0.0008	0.0126	0.0095	0.0074	0.0042	0.0017	0.0005	0.0042	0.0007	0.0006
0.32	0.56	theo	0.4276	0.0145	0.0089	0.0083	0.0133	0.0062	0.1158	0.0854	0.0701	0.0393	0.0144	0.0038	0.0355	0.0067	0.0055
		avg	0.4443	0.0151	0.0093	0.0086	0.0139	0.0064	0.1200	0.0889	0.0734	0.0411	0.0146	0.0039	0.0365	0.0070	0.0057
		std	0.0012	0.0002	0.0002	0.0002	0.0003	0.0002	0.0006	0.0005	0.0004	0.0004	0.0004	0.0001	0.0003	0.0002	0.0006
		min	0.4426	0.0148	0.0090	0.0084	0.0134	0.0062	0.1192	0.0880	0.0727	0.0404	0.0139	0.0038	0.0360	0.0067	0.0055
		max	0.4462	0.0154	0.0098	0.0089	0.0143	0.0067	0.1213	0.0897	0.0739	0.0419	0.0153	0.0042	0.0370	0.0072	0.0060
0.56	1	theo	0.2828	0.0096	0.0058	0.0058	0.0095	0.0036	0.0765	0.0554	0.0493	0.0281	0.0082	0.0022	0.0200	0.0047	0.0039
		avg	0.2848	0.0098	0.0057	0.0060	0.0097	0.0037	0.0765	0.0559	0.0497	0.0287	0.0082	0.0022	0.0200	0.0048	0.0040
		std	0.0019	0.0005	0.0002	0.0003	0.0002	0.0002	0.0011	0.0012	0.0006	0.0007	0.0003	0.0002	0.0006	0.0002	0.0057
		min	0.2819	0.0092	0.0054	0.0056	0.0095	0.0033	0.0745	0.0545	0.0488	0.0276	0.0078	0.0020	0.0193	0.0046	0.0037
		max	0.2884	0.0105	0.0062	0.0063	0.0102	0.0041	0.0780	0.0578	0.0504	0.0297	0.0089	0.0026	0.0212	0.0051	0.0042
1	1.78	theo	0.1878	0.0063	0.0038	0.0041	0.0068	0.0021	0.0506	0.0360	0.0347	0.0202	0.0047	0.0013	0.0112	0.0033	0.0027
		avg	0.1953	0.0066	0.0038	0.0042	0.0069	0.0022	0.0526	0.0375	0.0362	0.0213	0.0048	0.0012	0.0115	0.0036	0.0030
		std	0.0021	0.0007	0.0004	0.0006	0.0008	0.0003	0.0014	0.0009	0.0013	0.0005	0.0003	0.0001	0.0007	0.0003	0.0040
		min	0.1924	0.0059	0.0033	0.0033	0.0060	0.0017	0.0505	0.0359	0.0340	0.0204	0.0044	0.0011	0.0107	0.0032	0.0024
		max	0.1987	0.0079	0.0046	0.0053	0.0085	0.0026	0.0545	0.0385	0.0383	0.0219	0.0052	0.0015	0.0130	0.0041	0.0033
1.78	3.16	theo	0.1253	0.0042	0.0024	0.0029	0.0049	0.0013	0.0334	0.0234	0.0244	0.0144	0.0027	0.0008	0.0063	0.0023	0.0019
		avg	0.1314	0.0045	0.0025	0.0029	0.0057	0.0014	0.0333	0.0248	0.0262	0.0157	0.0030	0.0008	0.0063	0.0025	0.0019
		std	0.0053	0.0007	0.0006	0.0007	0.0007	0.0005	0.0030	0.0013	0.0010	0.0009	0.0006	0.0003	0.0010	0.0005	0.0030
		min	0.1212	0.0037	0.0017	0.0020	0.0048	0.0008	0.0276	0.0224	0.0245	0.0141	0.0020	0.0003	0.0050	0.0019	0.0015
		max	0.1381	0.0061	0.0039	0.0041	0.0067	0.0024	0.0367	0.0269	0.0275	0.0168	0.0039	0.0014	0.0082	0.0034	0.0028
3.16	5.62	theo	0.0839	0.0028	0.0016	0.0020	0.0035	0.0007	0.0221	0.0152	0.0172	0.0103	0.0015	0.0005	0.0036	0.0016	0.0014
		avg	0.0860	0.0032	0.0017	0.0018	0.0028	0.0006	0.0240	0.0158	0.0178	0.0098	0.0015	0.0003	0.0035	0.0017	0.0016
		std	0.0053	0.0012	0.0007	0.0009	0.0012	0.0006	0.0012	0.0029	0.0034	0.0019	0.0008	0.0003	0.0011	0.0005	0.0021
		min	0.0769	0.0012	0.0002	0.0005	0.0016	0	0.0223	0.0103	0.0135	0.0059	0.0004	0.0000	0.0025	0.0005	0.0005
		max	0.0957	0.0049	0.0027	0.0032	0.0050	0.0018	0.0258	0.0206	0.0252	0.0127	0.0026	0.0008	0.0061	0.0023	0.0029
5.62	10	theo	0.0564	0.0018	0.0010	0.0014	0.0025	0.0004	0.0146	0.0099	0.0121	0.0074	0.0009	0.0003	0.0020	0.0012	0.0010
		avg	0.0567	0.0018	0.0010	0.0010	0.0017	0.0003	0.0145	0.0103	0.0130	0.0072	0.0011	0.0005	0.0025	0.0008	0.0010
		std	0.0088	0.0012	0.0011	0.0009	0.0017	0.0006	0.0051	0.0033	0.0042	0.0024	0.0016	0.0007	0.0020	0.0007	0.0021
		min	0.0435	0.0005	0	0	0	0	0.0060	0.0067	0.0073	0.0036	0	0	0.0003	0	0
		max	0.0727	0.0040	0.0035	0.0021	0.0055	0.0018	0.0212	0.0170	0.0216	0.0105	0.0039	0.0018	0.0066	0.0021	0.0027
10	17.8	theo	0.0381	0.0012	0.0007	0.0010	0.0018	0.0003	0.0096	0.0064	0.0085	0.0053	0.0005	0.0002	0.0011	0.0008	0.0007
		avg	0.0340	0.0014	0.0011	0.0004	0.0023	0.0001	0.0107	0.0062	0.0065	0.0029	0.0000	0.0003	0.0006	0.0010	0.0006
		std	0.0113	0.0020	0.0024	0.0013	0.0030	0.0002	0.0061	0.0056	0.0035	0.0027	0.0001	0.0009	0.0012	0.0016	0.0018
		min	0.0175	0	0	0	0	0	0.0024	0.0003	0.0024	0	0	0	0	0	0
		max	0.0540	0.0060	0.0073	0.0040	0.0069	0.0007	0.0206	0.0199	0.0150	0.0088	0.0004	0.0028	0.0037	0.0050	0.0035
17.8	31.6	theo	0.0257	0.0008	0.0004	0.0007	0.0013	0.0002	0.0064	0.0042	0.0060	0.0038	0.0003	0.0001	0.0006	0.0006	0.0005
		avg	0.0205	0.0006	0	0.0010	0.0008	0	0.0057	0.0036	0.0043	0.0030	0	0.0002	0.0001	0.0012	0.0000
		std	0.0089	0.0010	0	0.0023	0.0018	0	0.0040	0.0042	0.0062	0.0034	0	0.0005	0.0004	0.0028	0.0013
		min	0.0106	0	0	0	0	0	0	0	0	0	0	0	0	0	0
		max	0.0389	0.0025	0	0.0072	0.0058	0	0.0123	0.0115	0.0173	0.0101	0	0.0015	0.0011	0.0080	0.0002
31.6	56.2	theo	0.0175	0.0005	0.0003	0.0005	0.0009	0.0001	0.0042	0.0027	0.0042	0.0027	0.0002	0.0001	0.0004	0.0004	0.0003
		avg	0.0203	0.0002	0	0.0001	0.0011	0	0.0088	0.0018	0.0054	0.0009	0	0	0	0.0020	0
		std	0.0119	0.0005	0	0.0004	0.0029	0	0.0095	0.0039	0.0073	0.0016	0	0	0	0.0041	0
		min	0	0	0	0	0	0	0	0	0	0	0	0	0	0	0
		max	0.0363	0.0015	0	0.0014	0.0094	0	0.0221	0.0125	0.0221	0.0042	0	0	0	0.0105	0
56.2	100	theo	0.0119	0.0003	0.0002	0.0004	0.0007	0.0001	0.0028	0.0018	0.0030	0.0019	0.0001	0.0000	0.0002	0.0003	0.0002
		max	0	0	0	0	0	0	0	0	0	0	0	0	0	0	0
100	178	theo	0.0081	0.0002	0.0001	0.0002	0.0005	0.0000	0.0018	0.0011	0.0021	0.0014	0.0001	0.0000	0.0001	0.0002	0.0002
		max	0	0	0	0	0	0	0	0	0	0	0	0	0	0	0
178	316	theo	0.0055	0.0002	0.0001	0.0002	0.0003	0.0000	0.0012	0.0007	0.0015	0.0010	0.0000	0.0000	0.0001	0.0001	0.0001
		max	0	0	0	0	0	0	0	0	0	0	0	0	0	0	0
316	562	theo	0.0038	0.0001	0.0001	0.0001	0.0002	0.0000	0.0008	0.0005	0.0010	0.0007	0.0000	0.0000	0.0000	0.0001	0.0001
		max	0	0	0	0	0	0	0	0	0	0	0	0	0	0	0

The absence of a  $P_{32}$  contribution from fractures larger than the range (101.5 m, 101.75 m)  $\approx$  (31.6 m, 56.2 m) is found to be a result of the discrete nature of the pseudo-random number generator that is used for Monte Carlo simulation of the fracture size distribution, in combination with the low minimum radius (0.3 m). The pseudo-random number generator (based on an algorithm given by Press et al., 1986) produces 714025 discrete values on the interval [0, 1). In combination with the algorithm used for generating values of  $r$  from a power-law distribution, this leads to an effective maximum radius:

$$r_{\text{max, eff}} = r_{\text{min}} \cdot \exp[-\log(1 - 1/714025)kr]$$

For the main (global) fracture sets and the subhorizontal local sets which account for 83% of the total  $P_{32}$ , the value of  $r_{max,eff}$  varies from 40.7 m to 55.8 m. In terms of fracture intensity the fractures in these sets with radius  $r$  in the range  $r_{max,eff} < r < r_{max}$  account for 0.0348 m<sup>2</sup>/m<sup>3</sup>. The EW, ENE, and NNE local sets have lower  $r_{max, eff}$  values in the range 26.9 m to 29.9 m, but due to their much lower intensity they account for only 0.00165 m<sup>2</sup>/m<sup>3</sup> of the fracture intensity.

These increments of  $P_{32}$  are a small percentage of the total  $P_{32}$  of 1.330 m<sup>2</sup>/m<sup>3</sup> for fractures in the simulated range ( $r > 0.3$  m). However fractures larger than  $r_{max,eff}$ , if they happen to intersect the 50m block, would tend to be through-cutting features.

The implications of omitting these fractures has been addressed by producing supplementary datasets for fractures in the size range  $r_{max, eff} < r < r_{max}$ , as described in a separate memorandum (dated 28 Mar 2014). When combined with the datasets from this delivery, these fractures cover the full range of sizes from  $r = 0.3$  m to 564.2 m. The total fracture intensity that results from combining the supplementary datasets with the datasets described in this memorandum is about 2.6% higher than the specified value of  $P_{32}$ .

## A2.2 Quality Check 2: Fracture orientation distributions

The simulated fracture orientation distributions have been confirmed both quantitatively by statistical measures, and qualitatively by equal-area stereonet plots for individual fracture sets.

The consistency of the fitted Fisher mean poles (mean pole trend and plunge in degrees, as given in parentheses) and concentration parameters  $\kappa$  in the following listing have been checked against the same parameters for the same 14 sets as listed in Table 1.

The mean pole directions are generally in very close agreement, usually within a fraction of a degree (somewhat larger for the Hydro-DFN sets which represent a smaller sample). It should be noted that for Set 9 (SH global/tight), fitted values for trend and plunge such as (359.34, 87.37) are in close agreement with the specified values (0.8, 87.3) when it is recalled that the azimuth of strike is a cyclic value. Similarly for Set 12, fitted directions such as (113.75, 0.10) are in close agreement with the specified value of (293.8, 0.0) when it is considered that fracture poles are bidirectional so can be represented equivalently by a direction that is 180 degrees opposed.

Values of the Fisher concentration  $\kappa$  in general agree with the specified values within 5%. Supplementary to these quantitative checks, stereonet plots were also produced for graphical comparison. These are shown for Realization 01 of the base case in Figures 5 through 7. Plots were generated for all realizations including both the base case and the elevated- $P_{32}$  variant. Although only plots for realization 01 of the base case are shown here, visual comparison of all plots was done by means of “thumbnail” versions of these plots such as illustrated in Figure 8.

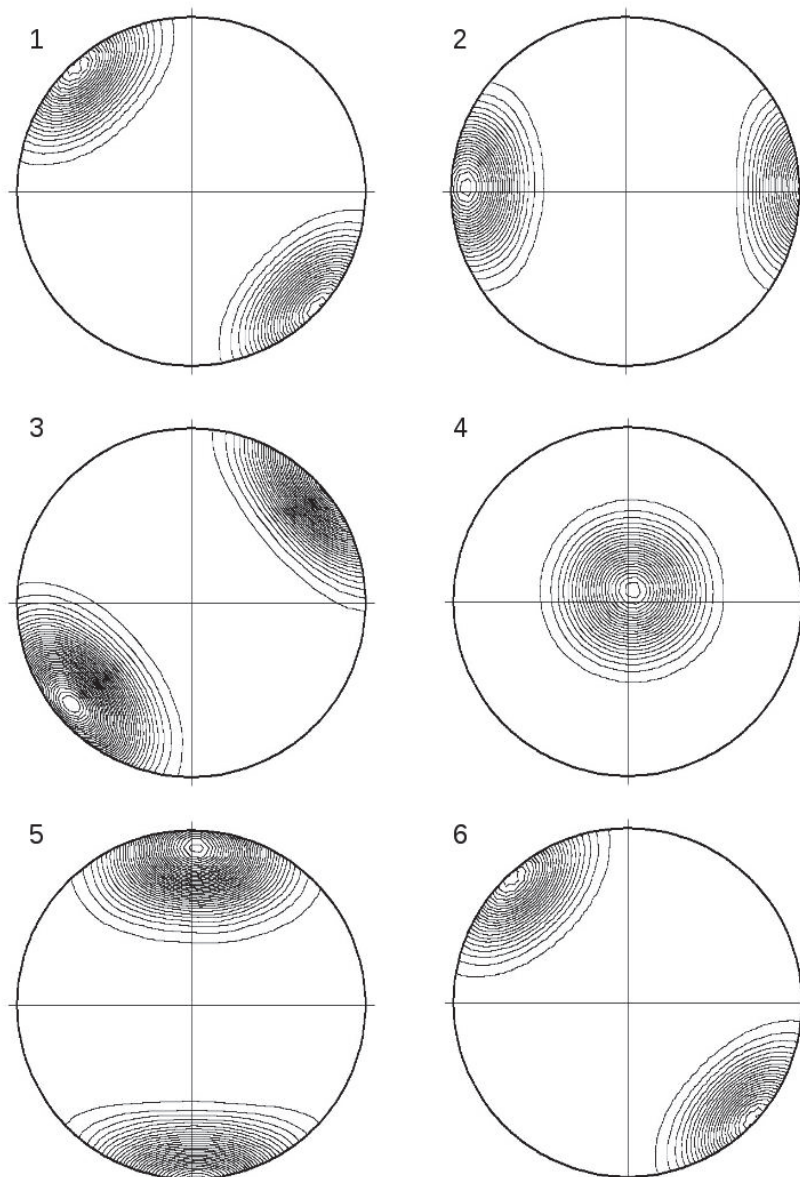


Figure A2-5. Equal-area stereonet plots of simulated fracture pole directions for the first six fracture sets in the r0-fixed base case model:(1) NE global/hydro, (2) NS global/hydro, (3) NW global/hydro, (4) SH global/hydro, (5) EW local, and (6) NE global/tight.

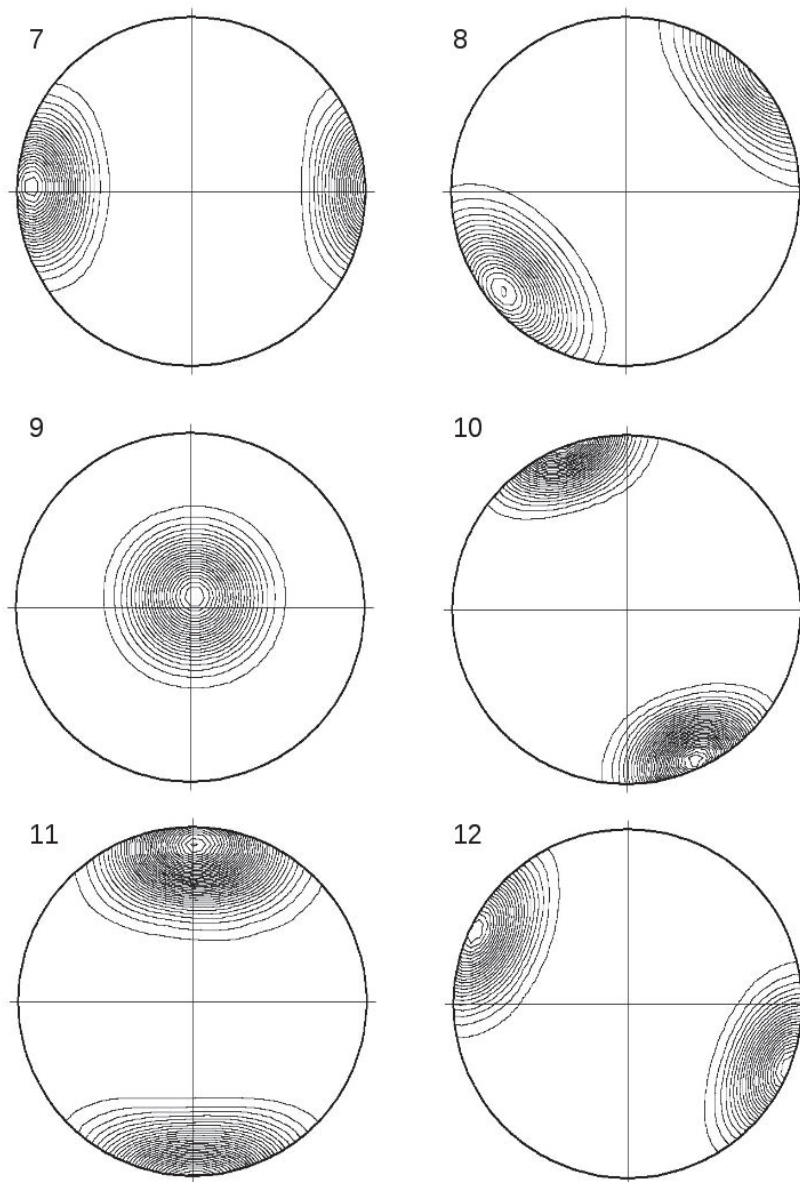


Figure A2-6. Equal-area stereonet plots of simulated fracture pole directions for fracture sets 7 through 12 in the  $r_0$ -fixed base case model: (7) NS global/tight, (8) NW global/tight, (9) SH global/tight, (10) ENE local, (11) EW local/tight, and (12) NNE local.

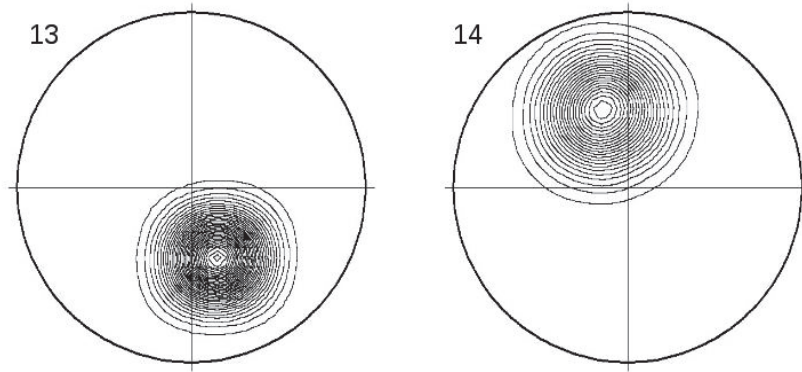


Figure A2-7. Equal-area stereonet plots of simulated fracture pole directions for the last two fracture sets in the r0-fixed base case model: (13) SH2 local, and (14) SH3 local.

### A2.3 Quality Check 3: Comparison of expected and simulated P21 fracture intensity on the sampling plane

The third main check of quality is to compare the observed values of fracture intensity as measured in the same 2-D cross-sections for which data area delivered, in terms of the P21 fracture intensity (trace length per unit area). This can be estimated from the volumetric fracture intensity  $P_{32}$ , after correcting for the effects of truncating the fracture size distribution by thinning out the fractures smaller than 0.3 m radius, and the orientation bias that results from the orientation of sampling planes (either horizontal, vertical with strike N35W, or vertical with strike N55E) relative to the fractures in each fracture set. The orientation bias is quantified by the factor C23 as defined by Wang (2005; see Geier, 2014 for details and method of calculation). The results are listed in Table 3. The expected P21 values for the elevated- $P_{32}$  variant can be calculated simply by scaling the values in Table 3 by a factor of 1.2. The expected  $P_{21}$  values can be compared with the total fracture trace length per unit area of the cross-section. This needs to be taken in the portion of the model within the volume that has been focused on for the repository simulates, to avoid other censoring effects. The results as shown in Table 4 (for the base case) and Table 5 (for the elevated- $P_{32}$  variant) show generally good agreement. For both the base case and the elevated- $P_{32}$  variant, the average simulated P21 over 10 realizations is within about 1% of the expected value, for all three cross-section orientations.

Table A2-3. Parameters for fracture sets for the r0-fixed base case, and resulting values of truncated P32 (for minimum fracture radius of 0.3 m), and corresponding values of the geometric factor C23 and P21.

FFM01	Mean pole trend	Mean pole plunge	Fisher conc. κ	$P_{32}$ (un-scaled)	$P_{32}$ (scaled)	Horizontal			Vertical N35W			Vertical N55E		
						$\rho$	$1/C_{23}$	$P_{21}$	$\rho$	$1/C_{23}$	$P_{21}$	$\rho$	$1/C_{23}$	$P_{21}$
NE global (hydro)	314.9	1.3	20.94	0.193	0.0434	88.7	0.98	0.0423	79.9	0.96	0.0417	10.2	0.31	0.0134
NS global (hydro)	270.1	5.3	21.34	0.122	0.0258	84.7	0.97	0.0251	35.4	0.60	0.0154	55.1	0.81	0.0209
NW global (hydro)	230.1	4.6	15.70	0.100	0.0280	85.4	0.97	0.0270	6.7	0.32	0.0090	85.1	0.97	0.0270
SH global (hydro)	0.8	87.3	17.42	0.158	0.0469	2.7	0.30	0.0139	88.4	0.97	0.0455	87.8	0.97	0.0455
EW local (hydro)	0.4	11.9	13.89	0.105	0.0154	78.1	0.94	0.0145	55.5	0.81	0.0124	37.1	0.62	0.0095
NE global (tight)	314.9	1.3	20.94	1.540	0.3461	88.7	0.98	0.3378	79.9	0.96	0.3329	10.2	0.31	0.1064
NS global (tight)	270.1	5.3	21.34	1.170	0.2474	84.7	0.97	0.2407	35.4	0.59	0.1470	55.1	0.81	0.2004
NW global (tight)	230.1	4.6	15.70	0.848	0.2374	85.4	0.97	0.2293	6.7	0.32	0.0766	85.1	0.97	0.2292
SH global (tight)	0.8	87.3	17.42	0.466	0.1383	2.7	0.30	0.0411	88.4	0.97	0.1344	87.8	0.97	0.1343
ENE local	157.5	3.1	34.11	0.256	0.0345	86.9	0.98	0.0339	77.5	0.96	0.0332	12.9	0.29	0.0101
EW local (tight)	0.4	11.9	13.89	0.064	0.0094	78.1	0.95	0.0088	55.5	0.81	0.0076	37.1	0.62	0.0058
NNE local	293.8	0.0	21.79	0.658	0.0833	90	0.98	0.0814	58.8	0.84	0.0703	31.2	0.54	0.0451
SH2 local	164.0	52.6	35.43	0.081	0.0227	37.4	0.61	0.0139	78.6	0.97	0.0219	55.0	0.81	0.0184
SH3 local	337.9	52.9	17.08	0.067	0.0188	37.1	0.62	0.0116	82.3	0.96	0.0181	54.0	0.80	0.0150
Total				5.828	1.2971			1.1215			0.9660			0.8811

Table A2-4. Comparison of expected and simulated values of P21 for the r0-fixed base case.

Realization	Horizontal Section $P_{21}$	Vertical N35W $P_{21}$	Vertical N55E $P_{21}$
01	1.1033	0.9419	0.8871
02	1.1618	0.9794	0.9268
03	1.1131	0.9844	0.9478
04	1.0964	0.9165	0.8710
05	1.1596	0.9840	0.9057
06	1.1220	0.9958	0.8690
07	1.1268	0.9298	0.8947
08	1.1100	0.9425	0.8673
09	1.1632	0.9732	0.8704
10	1.1261	0.9946	0.8531
Expected	1.1215	0.9660	0.8811
Average	1.1282	0.9642	0.8893
Ratio	1.0060	0.9981	1.0093

Table A2-5. Comparison of expected and simulated values of P21 for for the r0-fixed, elevated-P32 case.

Realization	Horizontal Section $P_{21}$	Vertical N35W $P_{21}$	Vertical N55E $P_{21}$
01	1.3293	1.1672	1.0707
02	1.3665	1.1765	1.0838
03	1.3174	1.1766	1.1269
04	1.3372	1.1073	1.0570
05	1.3853	1.1910	1.1434
06	1.3510	1.2099	1.0562
07	1.3681	1.1028	1.0583
08	1.3025	1.1433	1.0427
09	1.3835	1.1866	1.0415
10	1.3460	1.1819	1.0059
Expected	1.3458	1.1592	1.0573
Average	1.3487	1.1643	1.0686
Ratio	1.0021	1.0044	1.0107

## A2.3 References

Baecher GB, Lanney NA, Einstein HH (1977) Statistical description of rock properties and sampling. In: Proceedings of the 18th U.S. Symposium on Rock Mechanics, American Institute of Mining Engineers, 5C1-8.

Dershowitz WS, Herda H (1992) Interpretation of fracture spacing and intensity. In: Proceedings, 32nd US rock mechanics symposium, Santa Fe, New Mexico

Dershowitz W, Lee G, Geier J, Foxford T, LaPointe P, Thomas A (2004) FracMan, interactive discrete feature data analysis, geometric modelling, and exploration simulation. User documentation. Golder Associates Inc, Seattle, Washington

Fox A, La Pointe P, Hermanson J and Öhman, J (2007). Statistical geological discrete fracture network model. Forsmark modelling stage 2.2. SKB R-07-46 Svensk Kärnbränslehantering AB.

# Discrete fracture network realisations

A set of DFN realisations according to the SKB specifications have been provided by J. Geier on SSM's request as 2D cross sections that were derived from ten 3D DFN blocks (Min et al., 2013; see also Appendix 2). The 2D sections lie in the planes of the principal stress axes, i.e. in the vertical plane subject to SH-SV (N35W samples), in the vertical plane Sh-SV (N55E samples), and in the horizontal plane SH-Sh (HZ samples). That makes a total of 30 different sections that are shown in the following.

The DFN realisations have some 40,000 fractures, which is too many for computational reasons. Due to numerical constraints, the fracture sets were limited to fractures larger than 3 m. As from a fracture mechanical perspective longer fractures are more prone to extension, this simplification is motivated. The DFN models used for the simulations are depicted in Figure A2.3 to A2.32.



Figure A2.3. DFN realisation FFM01geoDFNr0fixed01\_HZ2d.prn. 107 fractures larger than 3 m were extracted from the large data set. The horizontal cross section faces in direction of Sv.



Figure A2.4. DFN realisation FFM01geoDFNr0fixed01\_N35W2d.prn. 102 fractures larger than 3 m were extracted from the large data set. The vertical cross section faces NE in direction of Sh.

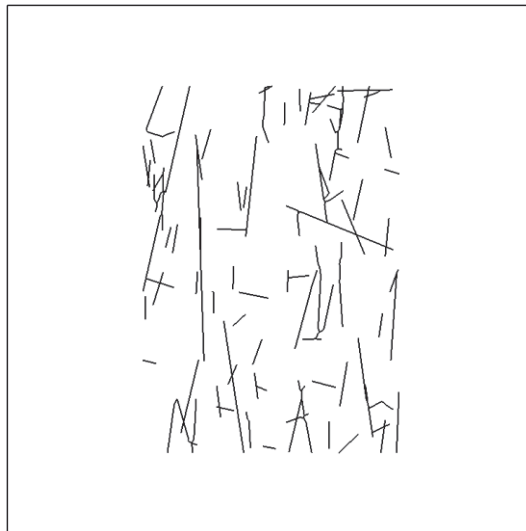


Figure A2.5. DFN realisation FFM01geoDFNr0fixed01\_N55E2d.prn. 102 fractures larger than 3 m were extracted from the large data set. The vertical cross section faces SE in direction of SH.



Figure A2.6. DFN realisation FFM01geoDFNr0fixed02\_HZ2d.prn. 107 fractures larger than 3 m were extracted from the large data set. The horizontal cross section faces in direction of Sv.



Figure A2.7. DFN realisation FFM01geoDFNr0fixed02\_N35W2d.prn. 135 fractures larger than 3 m were extracted from the large data set. The vertical cross section faces NE in direction of Sh.

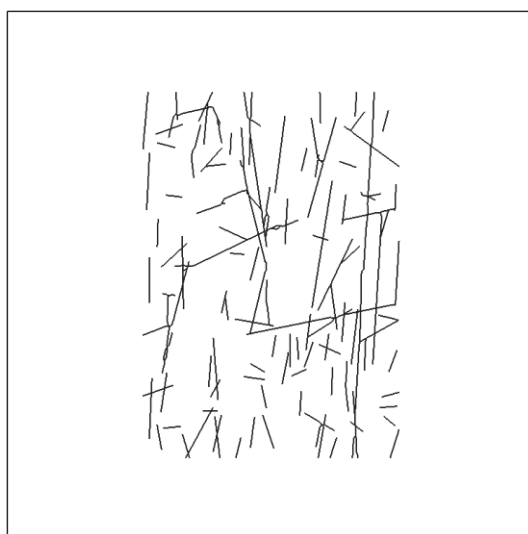


Figure A2.8. DFN realisation FFM01geoDFNr0fixed02\_N55E2d.prn. 129 fractures larger than 3 m were extracted from the large data set. The vertical cross section faces SE in direction of SH.

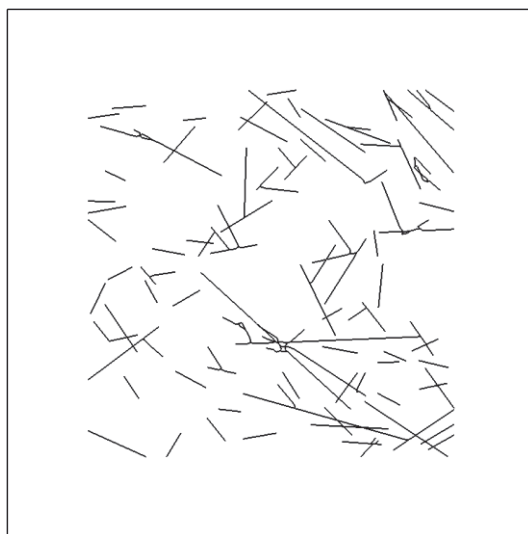


Figure A2.9. DFN realisation FFM01geoDFNr0fixed03\_HZ2d.prn. 111 fractures larger than 3 m were extracted from the large data set. The horizontal cross section faces in direction of Sv.



Figure A2.10. DFN realisation FFM01geoDFNr0fixed03\_N35W2d.prn. 125 fractures larger than 3 m were extracted from the large data set. The vertical cross section faces NE in direction of Sh.

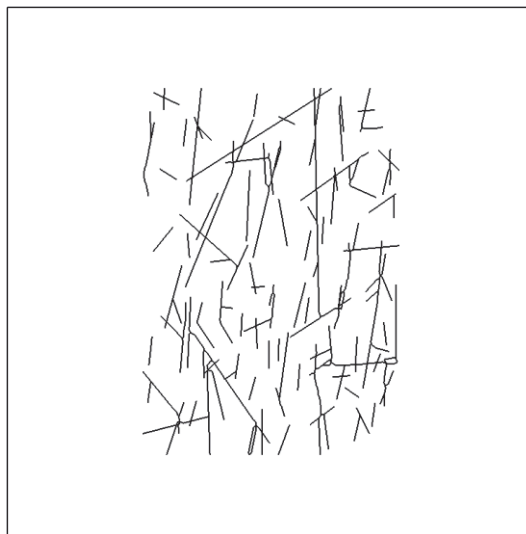


Figure A2.11. DFN realisation FFM01geoDFNr0fixed03\_N55E2d.prn. 133 fractures larger than 3 m were extracted from the large data set. The vertical cross section faces SE in direction of SH.



Figure A2.12. DFN realisation FFM01geoDFNr0fixed04\_HZ2d.prn. 88 fractures larger than 3 m were extracted from the large data set. The horizontal cross section faces in direction of Sv.



Figure A2.13. DFN realisation FFM01geoDFNr0fixed04\_N35W2d.prn. 96 fractures larger than 3 m were extracted from the large data set. The vertical cross section faces NE in direction of Sh.



Figure A2.14. DFN realisation FFM01geoDFNr0fixed04\_N55E2d.prn. 103 fractures larger than 3 m were extracted from the large data set. The vertical cross section faces SE in direction of SH.

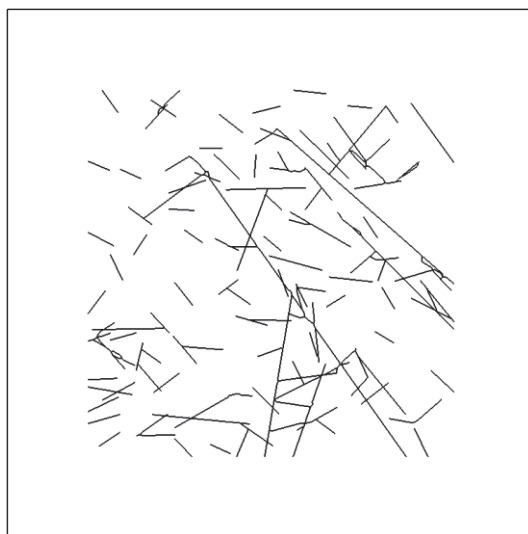


Figure A2.15. DFN realisation FFM01geoDFNr0fixed05\_HZ2d.prn. 131 fractures larger than 3 m were extracted from the large data set. The horizontal cross section faces in direction of Sv.

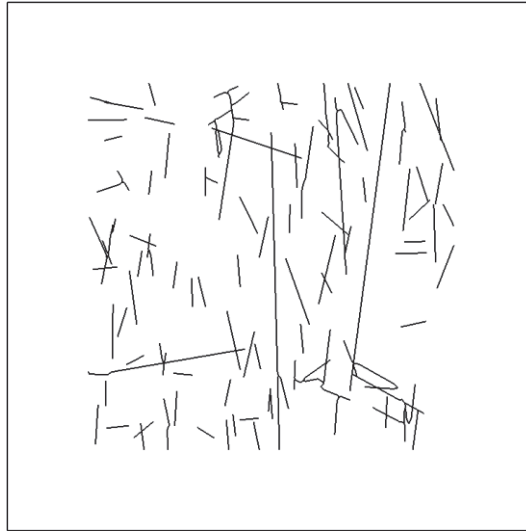


Figure A2.16. DFN realisation FFM01geoDFNr0fixed05\_N35W2d.prn. 119 fractures larger than 3 m were extracted from the large data set. The vertical cross section faces NE in direction of Sh.

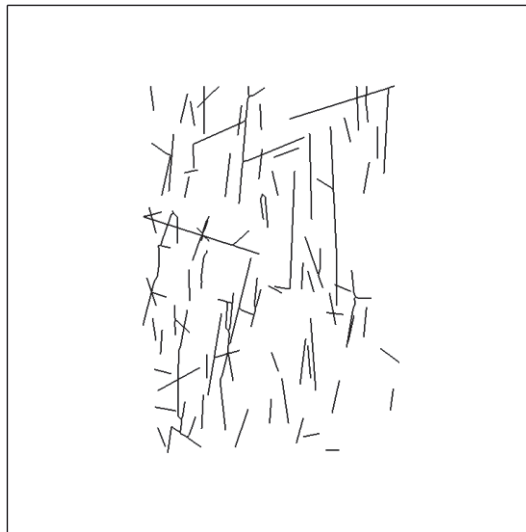


Figure A2.17. DFN realisation FFM01geoDFNr0fixed05\_N55E2d.prn. 108 fractures larger than 3 m were extracted from the large data set. The vertical cross section faces SE in direction of SH.

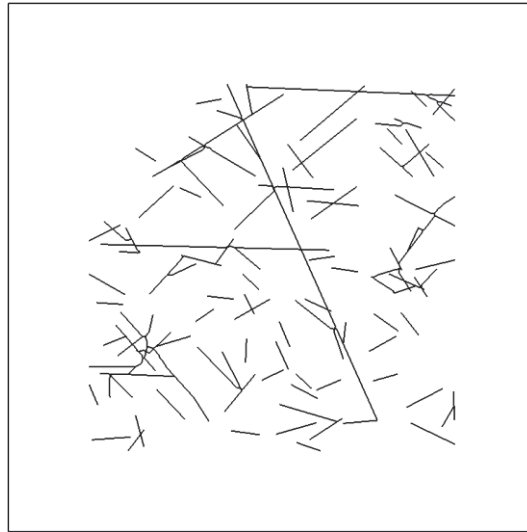


Figure A2.18. DFN realisation FFM01geoDFNr0fixed06\_HZ2d.prn. 111 fractures larger than 3 m were extracted from the large data set. The horizontal cross section faces in direction of Sv.

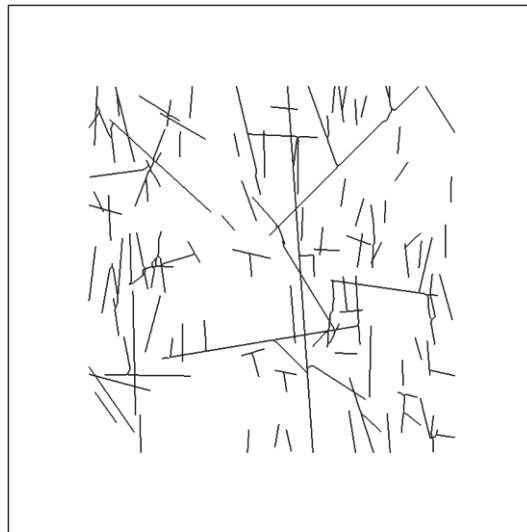


Figure A2.19. DFN realization FFM01geoDFNr0fixed06\_N35W2d.prn. 133 fractures larger than 3 m were extracted from the large data set. The vertical cross section faces NE in direction of Sh.



Figure A2.20. DFN realisation FFM01geoDFNr0fixed06\_N55E2d.prn. 99 fractures larger than 3 m were extracted from the large data set. The vertical cross section faces SE in direction of SH.

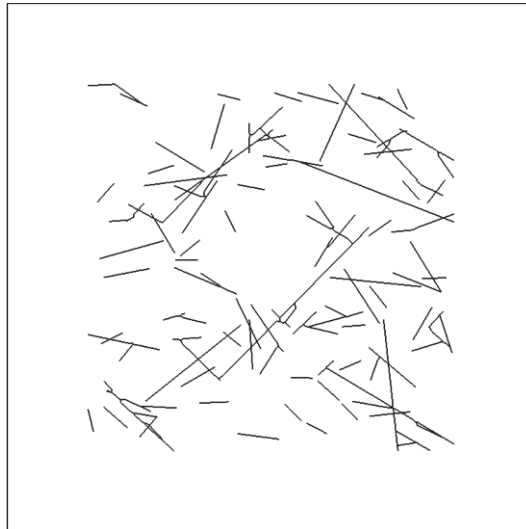


Figure A2.21. DFN realisation FFM01geoDFNr0fixed07\_HZ2d.prn. 116 fractures larger than 3 m were extracted from the large data set. The horizontal cross section faces in direction of Sv.

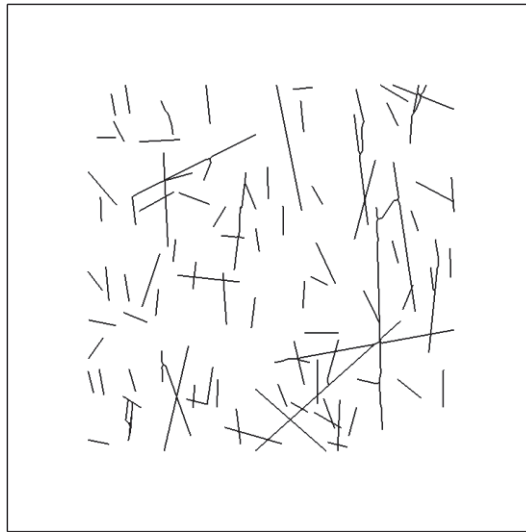


Figure A2.22. DFN realisation FFM01geoDFNr0fixed07\_N35W2d.prn. 105 fractures larger than 3 m were extracted from the large data set. The vertical cross section faces NE in direction of Sh.

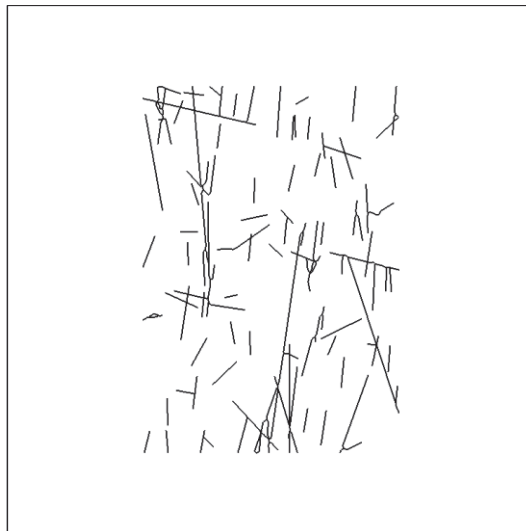


Figure A2.23. DFN realisation FFM01geoDFNr0fixed07\_N55E2d.prn. 111 fractures larger than 3 m were extracted from the large data set. The vertical cross section faces SE in direction of SH.

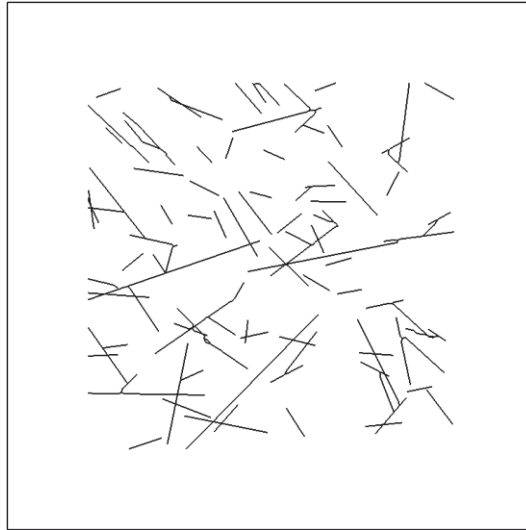


Figure A2.24. DFN realisation FFM01geoDFNr0fixed08\_HZ2d.prn. 105 fractures larger than 3 m were extracted from the large data set. The horizontal cross section faces in direction of Sv.

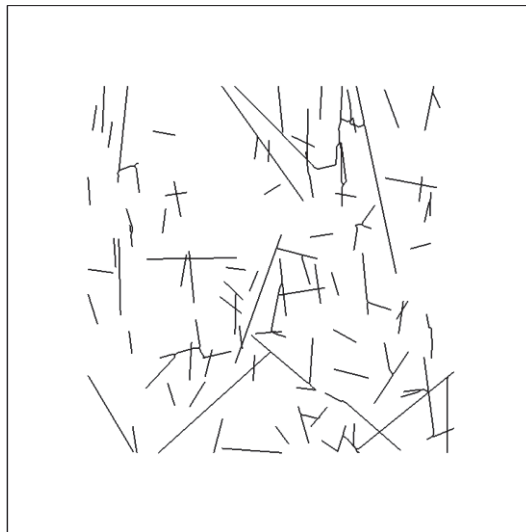


Figure A2.25. DFN realisation FFM01geoDFNr0fixed08\_N35W2d.prn. 112 fractures larger than 3 m were extracted from the large data set. The vertical cross section faces NE in direction of Sh.



Figure A2.26. DFN realisation FFM01geoDFNr0fixed08\_N55E2d.prn. 117 fractures larger than 3 m were extracted from the large data set. The vertical cross section faces SE in direction of SH.



Figure A2.27. DFN realisation FFM01geoDFNr0fixed09\_HZ2d.prn. 135 fractures larger than 3 m were extracted from the large data set. The horizontal cross section faces in direction of Sv.

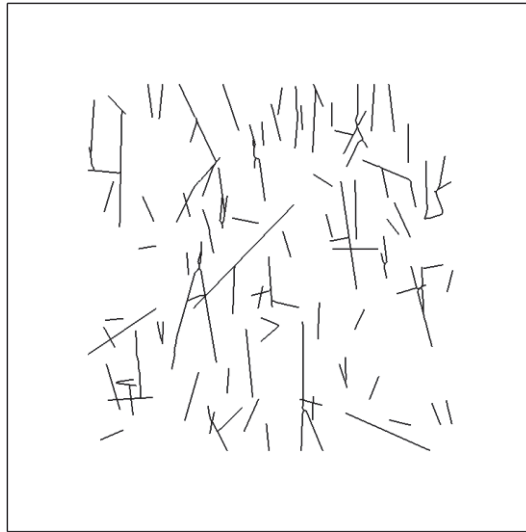


Figure A2.28. DFN realisation FFM01geoDFNr0fixed09\_N35W2d.prn. 118 fractures larger than 3 m were extracted from the large data set. The vertical cross section faces NE in direction of Sh.

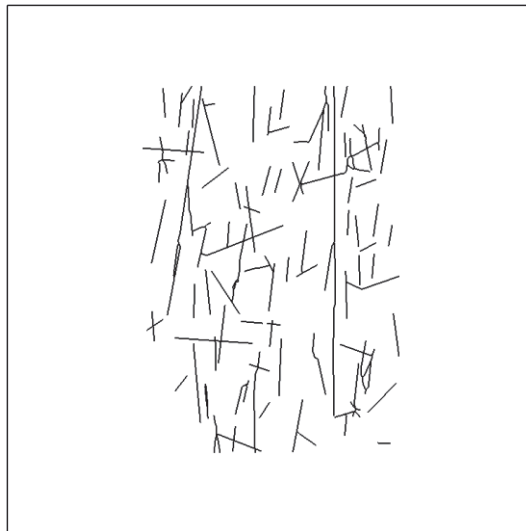


Figure A2.29. DFN realisation FFM01geoDFNr0fixed09\_N55E2d.prn. 117 fractures larger than 3 m were extracted from the large data set. The vertical cross section faces SE in direction of SH.

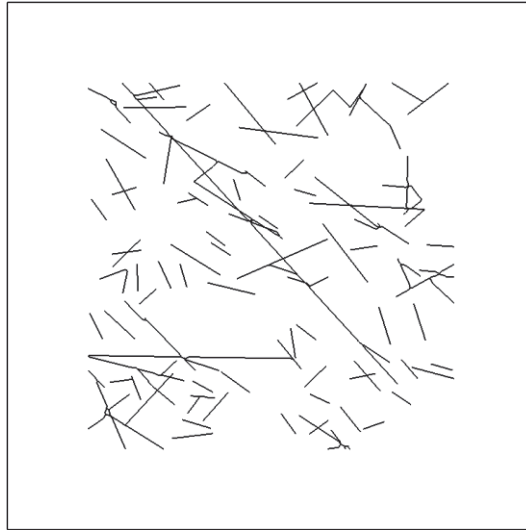


Figure A2.30. DFN realisation FFM01geoDFNr0fixed10\_HZ2d.prn. 116 fractures larger than 3 m were extracted from the large data set. The horizontal cross section faces in direction of Sv.

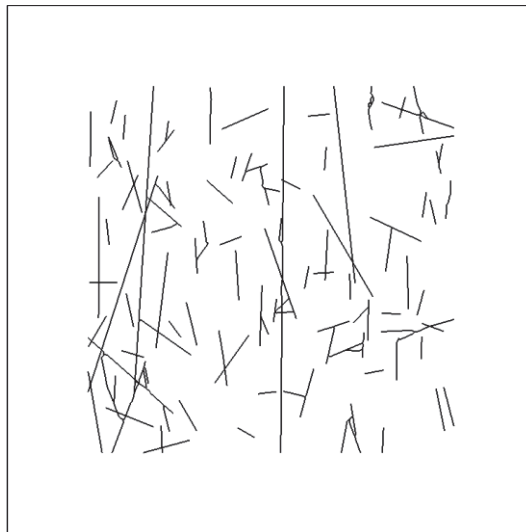


Figure A2.31. DFN realisation FFM01geoDFNr0fixed10\_N35W2d.prn. 119 fractures larger than 3 m were extracted from the large data set. The vertical cross section faces NE in direction of Sh.

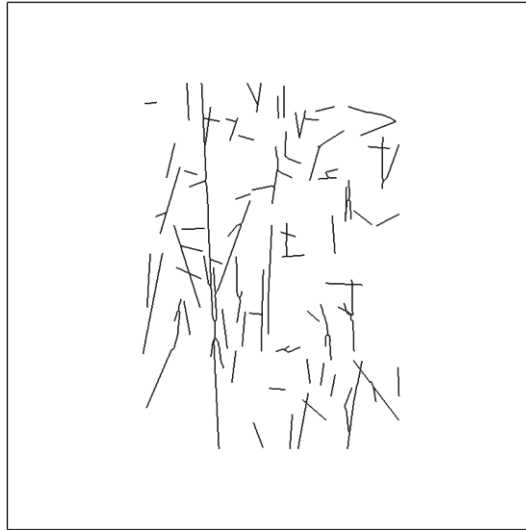


Figure A2.32. DFN realisation FFM01geoDFNr0fixed10\_N55E2d.prn. 102 fractures larger than 3 m were extracted from the large data set. The vertical cross section faces SE in direction of SH.

# Numerical approach and models

The simulation of fracture growth requires the employed numerical code to be able to handle discontinuities and the related strain and structural changes involved in the propagation of fractures. While standard commercial codes are usually not capable of simulating fracture growth, there are a few that are in principle suitable for that purpose. These are Fracod2d, Ycode, PFC and roxol. Each code has its advantages, but also limitations for the application to the current issues. This has been discussed in Backers (2010).

It was decided to use roxol in the context of this study. roxol ([www.roxol.de](http://www.roxol.de)) is based on the finite element method (FEM) with improved meshing for adaptability to fracture propagation and special shape functions for modelling of fractures. Geo-mechanical tasks are generally of high geometrical complexity, and there are a vast number of publications on numerical modelling applications in rock engineering using finite element models. The FEM is widely applied because of its flexibility in handling material heterogeneity, anisotropy, boundary conditions, and non-linear material behaviour. Many commercial software packages are available, and almost any physical law can be implemented in such code with a limited amount of effort.

However, when applied to the simulation of fracture propagation, the finite element approach has the limitation that crack propagation requires a doubling of the edges and subsequent adaptive redefinition of the underlying finite element mesh. Also, because the crack tip causes a singularity in the stress field, the mesh density in the vicinity of the crack tip has to be increased. Consequently, the numerical implementation effort and computing time are greatly increased, and yet the fracture propagation path remains mesh-dependent. The extended finite element method (XFEM) is an approach that has the capacity of resolving the limitation of the FEM above (e.g. Sukumar and Prévost, 2003; Budyn et al., 2004). The XFEM not only removes the necessity of re-meshing, but locally improves the accuracy of the numerical solution by introducing a priori knowledge about the stress and displacement fields near the crack tip (Schroeder, 2008).

roxol is based on XFEM and hence has all the advantages of being able to simulate physical processes by dedicated equations. The fractures are simulated by some added shape functions on the FEM framework, and hence almost any model of rock and fracture behaviour can be simulated.

roxol is capable of simulating a sufficient number of fractures. In addition to the aforementioned arguments, roxol allows the geomecon consultants free development of the software or direct access to certain source code blocks. A need for this was evident due to the fact that existing DFNs were to be analysed. Hence, a dedicated import function for the data provided by SSM had to be developed and implemented

into roxol. Further, additional statistical post-processing algorithms were implemented in the context of this work. The roxol server and client versions used for simulations in this report are 2259 and 2259\_1.

#### A4.1 The fracture network evolution simulator roxol™

geomecon GmbH is developing a software named roxol that can simulate fracture growth and related fracture network evolution in rock. The development is based on fracture mechanics principles. For this purpose the basis was developed in recent years and the feasibility of the methodology was proven in numerical campaigns.

At this point the mathematical basis is laid out and combined into an XFEM (extended finite element model) core software. The fundamental geomechanical models are adopted and implemented. The architecture of the code is based on a modular structure.

Currently the following functionalities are available:

- . linear elastic materials
- . orthotropic compliance matrix
- . varying material parameters
- . multiple material regions
- . two dimensional with quasi 3D out-of plane stress integration
- . stress boundaries (Neumann)
- . displacement boundaries (Dirichlet)
- . combination of stress and displacement boundaries
- . (fluid-) pressure on fractures
- . variable stress on fractures and boundaries
- . tensile fractures
- . fractures under compression with contact and Coulomb friction
- . fracture initiation criteria (Mohr-Coulomb, Mogi, Hoek-Brown, mean stress, deviatoric stress)
- . definition of fracture initiation length and fracture initiation distances
- . pre-existing fractures
- . statistical fracture generation wizard
- . fracture activation
- . stress and stress intensity factor based fracture propagation criteria and combinations thereof (circumferential stress, principal stress, maximum shear stress, linear  $K_{IC}$  -  $K_{IIC}$  mixed mode criterion, quadratic  $K_{IC}$  -  $K_{IIC}$  mixed mode criterion)
- . fracture interaction and coalescence
- . simple fracture geometry export and import functions

roxol has been recently used in several projects, e.g. for Central European Petroleum (Germany), GeoEnergy Suisse (Switzerland), Nagra (Switzerland) and Ruhr University Bochum (Germany). Publications include: Backers and Moeck (2014), Backers and Gruehser (2012), Backers et al. (2012), Mischo and Backers (2012), Backers and Stephansson (2011), Backers (2009) and Byfut et al. (2009). Additional verification examples may be found at [www.roxol.de](http://www.roxol.de).

## A4.2. Geomechanical models

The material law used in the simulations in this report is isotropic linear elastic, defined by the Young's moduli and Poisson's ratios.

The fractures are included in the geometrical model and fracture strength is modelled by Coulomb friction. The extension of fractures, hence fracture growth, is modelled by a combination of minimum tangential stress and maximum shear stress criterion. For a discussion of the model see Whittaker et al. (1992).

The critical values  $\sigma$  for tensile and shear fracture growth relate to fracture toughness with:

$$\sigma = K_C / \sqrt{2\pi r} \quad \text{Eq. (A2-1)}$$

where  $K_C$  is the respective fracture toughness and  $r$  is the evaluation radius at the fracture tip. Hence, with  $K_{IC} = 3.8 \text{ MPa}\sqrt{\text{m}}$ ,  $K_{IIC} = 5.1 \text{ MPa}\sqrt{\text{m}}$ , and an evaluation radius of  $r = 0.5 \text{ m}$  the critical values are  $\sigma_{CI} = 2.2 \text{ MPa}$  and  $\sigma_{CII} = 32 \text{ MPa}$ . Fracture initiation or activation is not considered in this report but can be simulated with roxol; it is anticipated that existing fractures will propagate.

## A4.3 Numerical model

The numerical model makes use of the geomechanical models described in the previous section. The geometrical model consists of a domain of  $72 \text{ m} \times 72 \text{ m}$ , of which the DFN model is allowed to populate the central area of  $52 \text{ m} \times 52 \text{ m}$  (Figure A2.2).

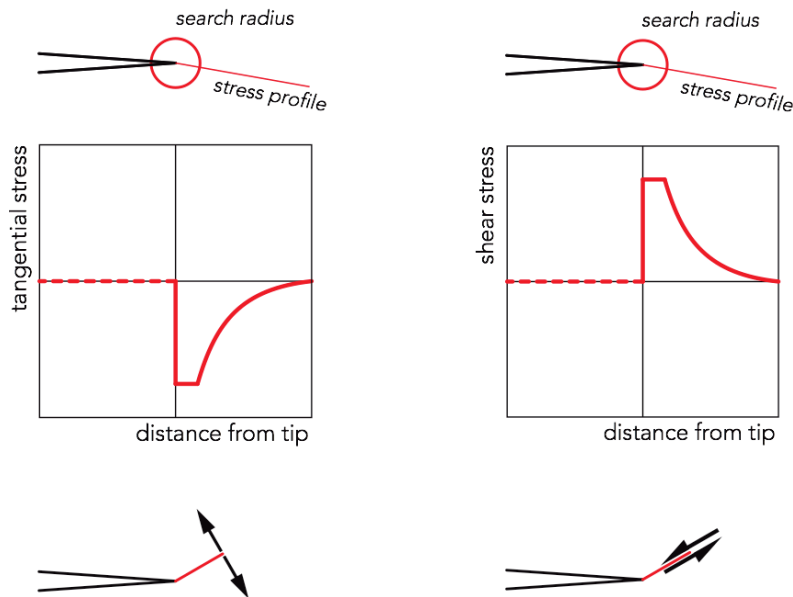


Figure A2.1. Schematic representation of the fracture propagation criterion. Fracture extension either takes place if the local minimum tangential stress at the tip is smaller than a critical value related to  $K_{IC}$ , or if the local maximum shear stress is larger than a critical value related to  $K_{IIC}$ .

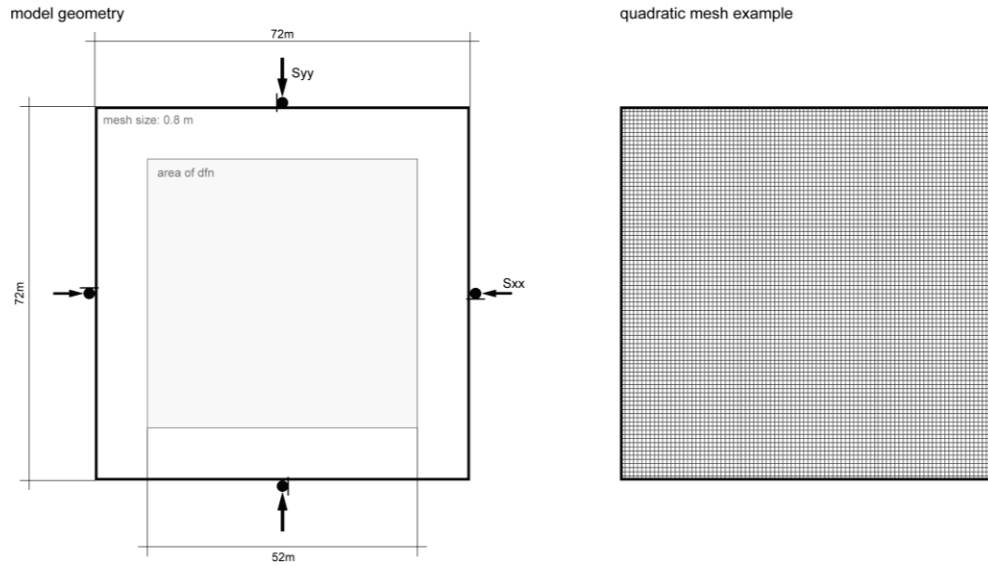


Figure A2.2. Model setup, boundary conditions (left) and mesh (right) used for the simulations of fracture propagation. The quadratic graded mesh consists of 8,100 elements.

#### A4.5 Confirmation of the stability of the DFNs at present

The different DFN realisations as discussed in the previous section appear to be stable at current days conditions, hence the assigned properties and the given in situ stress field model should lead to no significant fracture growth in the simulations. The simulations with the base case properties have been run and showed not more than four fractures propagating in one simulation step. Of a total number of over hundred fractures this is considered negligible. Therefore, the model is assumed to be valid.

#### A4.6 Results of roxol simulations

The simulation results are summarised in Tables A2.1 to A.11.

## A4.7 References

- Backers T, 2010. Applications of fracture mechanics numerical modelling in rock engineering. first break. Volume 28, issue 3, pages 13 - 22.
- Budyn E, Zi G, Moes N, Belytschko T, 2004. A method for multiple crack growth in brittle materials without remeshing. International Journal for Numerical Methods in Engineering, 61, 1741-1770.
- Schroeder A, 2008. Constraints coefficients in hp – fem. In: Kunisch K, Of G, Steinbach O (Eds.) Numerical Mathematics and Advanced Applications. Springer, Berlin, 183–190.
- Sukumar N, Prévost J-H, 2003. Modeling quasi-static crack growth with the extended finite element method Part I: Computer implementation. International Journal of Solids and Structures, 40, 7513–7537.
- Whittaker BN, Singh RN, Sun G, 1992. Rock Fracture Mechanics - Principles, Design and Applications, volume 72 of Developements of Geotechnical Engineering. Elsevier, Amsterdam - London - New York Tokyo, 1992.



# Numerical results

## A5.1 Results of the thermal analyses

Thermal phase (Simulation 3, stresses: SH 62.5, Sh 36.3, SV 13.3, Pp 5.0)	Section	Block	total length of new cracks	relative crack length increase	average propagation angle	average Mode I	average Mode II	propagation steps
			[m]	[%]	[°]	[%]	[%]	[-]
Hz		Block 1	0	0.0	-	-	-	0
		Block 2	1	0.1	6	0	100	1
		Block 3	1	0.2	30	0	100	1
		Block 4	2	0.4	29	67	33	1
		Block 5	8	1.1	36			2
		Block 6	0	0.0	-	-	-	0
		Block 7	4	0.5	64	0	100	1
		Block 8	3	0.5	53		67	3
		Block 9	1	0.1	21	0	100	1
		Block 10	3	0.4	44	0	100	3
			2	0.3	36			1.3
N35W		Block 1	132	23.5	25	14	86	10
		Block 2	222	27.8	32	22	78	10
		Block 3	126	17.5	30	22	78	10
		Block 4	75	14.1	24	10	90	10
		Block 5	51	7.6	23	9	91	10
		Block 6	187	23.2	30	23	77	10
		Block 7	140	22.9	31	22	78	10
		Block 8	160	25.4	29	19	81	10
		Block 9	121	20.3	26	21	79	10
		Block 10	136	19.3	30	23	77	10
			135	20.2	28	19	81	10
N55E		Block 1	0	0.0	71	100	0	1
		Block 2	0	0.0	-	-	-	0
		Block 3	0	0.0	-	-	-	0
		Block 4	0	0.1	71	100	0	1
		Block 5	0	0.0	-	-	-	0
		Block 6	0	0.0	-	-	-	0
		Block 7	0	0.0	-	-	-	0
		Block 8	0	0.0	-	-	-	0
		Block 9	0	0.0	-	-	-	0
		Block 10	0	0.0	-	-	-	0
			0	0.0	71	100	0	0.2

## A5.2 Results of the thermal analyses with increased $K_{IIC}$ .

Thermal phase (Simulation 3, stresses: SH 62.5, Sh 36.3, SV 13.3, Pp 5.0)	Section	Block	total length of new cracks	relative crack length increase	average propagation angle	average Mode I	average Mode II	propagation steps
			[m]	[%]	[°]	[%]	[%]	[-]
	N35W	Block 1	30	5.3	29	26	74	10
		Block 2	72.7	9.1	25.8	32.1	67.9	10.0
		Block 3	56.0	7.7	28.8	42.7	57.3	10.0
		Block 4	15	2.7	28	16	84	6
		Block 5	12	1.7	23	21	79	4
		Block 6	52	6.5	28	52	48	10
		Block 7	56	9.1	30	27	73	10
		Block 8	58	9.2	34	30	70	10
		Block 9	37	6.2	25	48	52	10
		Block 10	60	8.4	37	32	68	10
			45	6.6	29	33	67	9

### A5.3 Results of the thermal analyses with deposition holes.

Thermal phase (Simulation 3, stresses: SH 62.5, Sh 36.3, SV 13.3, Pp 5.0)	Section	Block	total length of new cracks	relative crack length increase	average propagation angle	average Mode I	average Mode II	propagation steps
			[m]	[%]	[°]	[%]	[%]	[-]
	Hz	Block 1	0	0.0	-	-	-	0
		Block 2	10	1.2	33	9	91	3
		Block 3	5	0.8	63	0	100	2
		Block 4	0	0.0	-	-	-	0
		Block 5	6	0.8	57	44	56	2
		Block 6	12	1.7	18	31	69	5
		Block 7	0	0.0	-	-	-	0
		Block 8	3	0.4	21	0	100	2
		Block 9	3	0.4	58	25	75	2
		Block 10	8	1.1	37	20	80	5
			5	0.7	41	18	82	2.1

## A5.4 Results of the analyses of glaciation stage T1.

Glaciation T1 (Simulation 4, stress: SH 51.5, Sh 27.3, SV 31.3, Pp 14.0)	Section	Block	total length of new cracks	relative crack length increase	average propagation angle	average Mode I	average Mode II	propagation steps
			m	%	°	%	%	-
	Hz	Block 1	0	0.0	-	-	-	0
		Block 2	1	0.1	17	0	100	2
		Block 3	1	0.2	15	0	100	2
		Block 4	2	0.3	31	100	0	1
		Block 5	7	0.9	33	33	67	5
		Block 6	0	0.0	-	-	-	0
		Block 7	3	0.4	44	50	50	3
		Block 8	3	0.5	56	50	50	2
		Block 9	0	0.0	-	-	-	0
		Block 10	2	0.3	36	0	100	2
			2	0.3	33	33	67	1.7
	N35W	Block 1	0	0.0	-	-	-	0
		Block 2	0	0.0	-	-	-	0
		Block 3	0	0.0	-	-	-	0
		Block 4	1	0.1	63	0	100	1
		Block 5	1	0.1	8	0	100	1
		Block 6	1	0.2	40	50	50	3
		Block 7	0	0.0	-	-	-	0
		Block 8	0	0.0	-	-	-	0
		Block 9	0	0.0	-	-	-	0
		Block 10	0	0.0	-	-	-	0
			0	0.0	37	17	83	0.5
	N55E	Block 1	0	0.0	71	0	100	1
		Block 2	0	0.1	38	100	0	1
		Block 3	0	0.0	-	-	-	0
		Block 4	0	0.0	-	-	-	0
		Block 5	0	0.0	-	-	-	0
		Block 6	0	0.0	-	-	-	0
		Block 7	0	0.0	-	-	-	0
		Block 8	0	0.0	-	-	-	0
		Block 9	0	0.0	-	-	-	0
		Block 10	0	0.0	-	-	-	0
			0	0.0	54	50	50	0.2

## A5.5 Results of the analyses of glaciation stage T2.

Glaciation T2 (Simulation 5, stresses: SH 43, Sh 18.3, SV 13.3, Pp 5.0)	Section	Block	total length of new cracks	relative crack length increase	average propagation angle	average Mode I	average Mode II	propagation steps
			m	%	°	%	%	
Hz	Block 1	Block 1	0	0.0	-	-	-	0
		Block 2	0	0.1	29	0	100	1
		Block 3	1	0.1	29	0	100	1
		Block 4	2	0.3	31	100	0	1
		Block 5	1	0.2	71	100	0	1
		Block 6	0	0.0	-	-	-	0
		Block 7	3	0.4	67	50	50	1
		Block 8	0	0.0	-	-	-	0
		Block 9	0	0.0	-	-	-	0
		Block 10	4	0.6	46	60	40	2
	Block 1	Block 1	1	0.2	46	52	48	0.7
		Block 1	0	0.0	-	-	-	0
		Block 2	4	0.5	68	88	13	3
		Block 3	3	0.4	48	100	0	2
		Block 4	0	0.1	59	100	0	1
		Block 5	0	0.0	-	-	-	0
		Block 6	17	2.1	27	92	8	8
		Block 7	0	0.0	-	-	-	0
		Block 8	1	0.1	46	100	0	1
		Block 9	2	0.3	52	100	0	3
		Block 10	0	0.0	17	0	100	1
		Block 1	3	0.3	45	83	17	1.9
N35W	Block 1	Block 1	0	0.0	71	100	0	1
		Block 2	0	0.1	38	100	0	1
		Block 3	0	0.0	-	-	-	0
		Block 4	0	0.0	-	-	-	0
		Block 5	0	0.0	-	-	-	0
		Block 6	0	0.0	-	-	-	0
		Block 7	0	0.0	-	-	-	0
		Block 8	0	0.0	-	-	-	0
		Block 9	0	0.0	-	-	-	0
		Block 10	0	0.0	-	-	-	0
		Block 1	0	0.0	54	100	0	0.2
N55E	Block 1	Block 1	0	0.0	71	100	0	1
		Block 2	0	0.1	38	100	0	1
		Block 3	0	0.0	-	-	-	0
		Block 4	0	0.0	-	-	-	0
		Block 5	0	0.0	-	-	-	0
		Block 6	0	0.0	-	-	-	0
		Block 7	0	0.0	-	-	-	0
		Block 8	0	0.0	-	-	-	0
		Block 9	0	0.0	-	-	-	0
		Block 10	0	0.0	-	-	-	0

## A5.6 Results of the analyses of glaciation stage T3.

Glaciation T3 (Simulation 6, stress: SH35.5, Sh 8.3, SV 13.3, Pp 5.0)	Section	Block	total length of new cracks	relative crack length increase	average propagation angle	average Mode I	average Mode II	propagation steps
			m	%	°	%	%	
Hz		Block 1	52	8.3	20	96	4	10
		Block 2	100	12.8	23	87	13	10
		Block 3	16	2.4	44	88	13	5
		Block 4	59	10.8	21	99	1	10
		Block 5	87	11.5	21	96	4	10
		Block 6	36	5.4	28	98	2	10
		Block 7	52	7.5	21	94	6	10
		Block 8	70	10.9	22	92	8	10
		Block 9	38	5.2	16	100	0	10
		Block 10	81	12.0	21	94	6	10
			59	8.7	24	94	6	9.5
N35W		Block 1	0	0.0	-	-	-	1
		Block 2	1	0.1	61	100	0	2
		Block 3	3	0.5	38	100	0	2
		Block 4	0	0.0	-	-	-	0
		Block 5	0	0.0	-	-	-	0
		Block 6	3	0.4	36	67	33	3
		Block 7	0	0.0	-	-	-	0
		Block 8	0	0.0	-	-	-	0
		Block 9	1	0.2	72	100	0	1
		Block 10	0	0.0	-	-	-	0
			1	0.1	52	92	8	0.9
N55E		Block 1	0	0.0	-	-	-	0
		Block 2	0	0.1	38	100	0	1
		Block 3	0	0.0	-	-	-	0
		Block 4	0	0.0	-	-	-	0
		Block 5	0	0.0	-	-	-	0
		Block 6	0	0.0	-	-	-	0
		Block 7	0	0.0	71	100	0	1
		Block 8	0	0.0	-	-	-	0
		Block 9	0	0.0	-	-	-	0
		Block 10	0	0.0	-	-	-	0
			0	0.0	54	100	0	0.2

## A5.7 Results of the analyses of glaciation stage T4.

Glaciation T4 (Simulation 7, stresses: SH 64.5, Sh 40.3, SV 44.3, Pp 19.0)	Section	Block	total length of new cracks	relative crack length increase	average propagation angle	average Mode I	average Mode II	propagation steps
			m	%	°	%	%	-
Hz		Block 1	1	0.1	59	0	100	1
		Block 2	2	0.2	21	0	100	1
		Block 3	1	0.2	29	0	100	1
		Block 4	2	0.4	29	67	33	1
		Block 5	8	1.1	37	14	86	3
		Block 6	0	0.0	-	-	-	0
		Block 7	4	0.6	32	0	100	2
		Block 8	2	0.4	50	0	100	1
		Block 9	1	0.1	21	0	100	1
		Block 10	2	0.4	36	0	100	2
			2	0.3	35	9	91	1.3
N35W		Block 1	0	0.0	-	-	-	0
		Block 2	0	0.0	-	-	-	0
		Block 3	1	0.1	0	0	100	2
		Block 4	1	0.1	50	0	100	2
		Block 5	1	0.1	8	0	100	1
		Block 6	2	0.2	64	0	100	3
		Block 7	0	0.0	-	-	-	0
		Block 8	1	0.2	25	0	100	1
		Block 9	0	0.0	-	-	-	0
		Block 10	0	0.0	-	-	-	0
			1	0.1	30	0	100	0.9
N55E		Block 1	0	0.0	71	100	0	1
		Block 2	0	0.1	38	100	0	1
		Block 3	0	0.0	-	-	-	0
		Block 4	0	0.0	-	-	-	0
		Block 5	0	0.0	-	-	-	0
		Block 6	0	0.0	-	-	-	0
		Block 7	0	0.0	-	-	-	0
		Block 8	0	0.0	-	-	-	0
		Block 9	0	0.0	-	-	-	0
		Block 10	1	0.1	71	0	100	1
			0	0.0	60	67	33	0.3

## A5.8 Results of the analyses of glaciation stage T5.

Glaciation T5 (Simulation 8, stresses: SH 48, Sh 22.3, SV 13.3, Pp 5.0)	Section	Block	total length of new cracks	relative crack length increase	average propagation angle	average Mode I	average Mode II	propagation steps
			m	%	°	%	%	
Hz		Block 1	0	0.0	-	-	-	0
		Block 2	1	0.1	44	0	100	1
		Block 3	1	0.2	15	0	100	2
		Block 4	2	0.3	31	100	0	1
		Block 5	4	0.5	60	67	33	3
		Block 6	0	0.0	-	-	-	0
		Block 7	4	0.6	44	33	67	3
		Block 8	0	0.0	-	-	-	0
		Block 9	0	0.0	-	-	-	0
		Block 10	2	0.3	33	25	75	2
			1	0.2	38	38	63	1.2
N35W		Block 1	3	0.6	28	50	50	4
		Block 2	27	3.4	30	60	40	10
		Block 3	9	1.3	58	92	8	5
		Block 4	1	0.2	57	50	50	1
		Block 5	1	0.2	23	100	0	2
		Block 6	18	2.3	35	81	19	10
		Block 7	10	1.7	42	40	60	6
		Block 8	3	0.6	30	67	33	2
		Block 9	17	2.8	31	80	20	10
		Block 10	3	0.4	50	86	14	4
			9	1.3	38	71	29	5.4
N55E		Block 1	0	0.0	71	100	0	1
		Block 2	1	0.1	54	100	0	1
		Block 3	0	0.0	-	-	-	0
		Block 4	0	0.0	-	-	-	0
		Block 5	0	0.1	36	100	0	2
		Block 6	0	0.0	-	-	-	0
		Block 7	0	0.0	-	-	-	0
		Block 8	0	0.0	-	-	-	0
		Block 9	0	0.0	-	-	-	0
		Block 10	0	0.0	-	-	-	0
			0	0.0	54	100	0	0.4

## A5.9 Results of the analyses of earthquake scenario with magnitude 6.0.

Earthquake M6 (Simulation9, stresses: SH 36.6, Sh 12.6, SV 13.4, Pp 5.0)	Section	Block	total length of new cracks	relative crack length increase	average propagation angle	average Mode I	average Mode II	propagation steps
			m	%	°	%	%	-
	Hz	Block 1	1	0.1	50	100	0	1
		Block 2	9	1.2	14	87	13	8
		Block 3	1	0.2	47	100	0	1
		Block 4	4	0.8	47	100	0	2
		Block 5	12	1.6	46	94	6	4
		Block 6	0	0.0	-	-	-	0
		Block 7	6	0.8	63	86	14	3
		Block 8	0	0.0	-	-	-	0
		Block 9	2	0.2	38	100	0	1
		Block 10	6	1.0	30	88	13	3
			4	0.6	42	94	6	2.3
	N35W	Block 1	0	0.0	-	-	-	0
		Block 2	0	0.0	-	-	-	0
		Block 3	1	0.1	42	100	0	1
		Block 4	0	0.0	-	-	-	0
		Block 5	1	0.2	72	100	0	1
		Block 6	3	0.4	44	67	33	3
		Block 7	0	0.0	-	-	-	0
		Block 8	0	0.1	71	100	0	1
		Block 9	0	0.0	-	-	-	0
		Block 10	0	0.1	17	0	100	1
			1	0.1	49	73	27	0.7
	N55E	Block 1	1	0.2	36	100	0	2
		Block 2	0	0.1	38	100	0	1
		Block 3	0	0.0	-	-	-	0
		Block 4	0	0.0	-	-	-	0
		Block 5	0	0.0	-	-	-	0
		Block 6	0	0.0	-	-	-	0
		Block 7	0	0.0	-	-	-	0
		Block 8	0	0.0	-	-	-	0
		Block 9	0	0.0	-	-	-	0
		Block 10	0	0.0	-	-	-	0
			0	0.0	37	100	0	0.3

## A5.10 Results of the analyses of earthquake scenario with magnitude 7.0.

Earthquake M7 (Simulation 10, stresses: SH 43.2, Sh -0.4, SV 13.3, Pp 5.0)	Section	Block	total length of new cracks	relative crack length increase	average propagation angle	average Mode I	average Mode II	propagation steps
			m	%	°	%	%	-
Hz		Block 1	491	79.3	19	87	13	10
		Block 2	456	58.7	21	84	16	10
		Block 3	489	73.3	18	86	14	10
		Block 4	406	74.6	17	89	11	10
		Block 5	490	65.0	22	80	20	10
		Block 6	482	71.4	20	84	16	10
		Block 7	372	53.2	21	86	14	7
		Block 8	436	68.5	21	83	17	10
		Block 9	520	70.2	19	86	14	10
		Block 10	529	78.0	25	84	16	10
N35W			467	69.2	20	85	15	9.7
		Block 1	0	0.0	-	-	-	0
		Block 2	5	0.7	63	89	11	4
		Block 3	9	1.2	47	100	0	4
		Block 4	0	0.1	59	100	0	1
		Block 5	0	0.0	-	-	-	0
		Block 6	17	2.1	36	86	14	10
		Block 7	0	0.0	-	-	-	0
		Block 8	3	0.5	22	50	50	4
		Block 9	2	0.3	60	100	0	3
N55E		Block 10	0	0.0	38	100	0	1
			4	0.5	46	89	11	2.7
		Block 1	226	42.4	22	95	5	10
		Block 2	194	27.8	13	99	1	10
		Block 3	145	20.0	14	100	0	7
		Block 4	173	35.5	14	100	0	10
		Block 5	208	38.5	14	100	0	10
		Block 6	191	37.3	14	99	1	10
		Block 7	251	44.5	13	100	0	10
		Block 8	175	29.2	11	99	1	10
		Block 9	174	29.4	12	100	0	10
		Block 10	143	29.8	12	100	0	10
			188	33.4	14	99	1	9.7

## A5.11 Results of the analyses of fault jump.

Earthquake M7 (Simulation 10, stresses: SH 43.2, Sh -0.4, SV 13.3, Pp 5.0)	Section	Block	total length of new cracks	relative crack length increase	average propagation angle	average Mode I	average Mode II	propagation steps
			m	%	°	%	%	-
	Hz	Block 1	2	0.1	46	100	0	1
		Block 2	1	0.1	50	100	0	1
		Block 3	0	0.0	-	-	-	0
		Block 4	5	0.3	39	100	0	2
		Block 5	1	0.1	46	100	0	2
		Block 6	0	0.0	-	-	-	0
		Block 7	0	0.0	-	-	-	0
		Block 8	1	0.1	61	100	0	1
		Block 9	1	0.1	61	100	0	2
		Block 10	3	0.2	46	100	0	2
			1	0.1	50	100	0	1.1





2015:30

The Swedish Radiation Safety Authority has a comprehensive responsibility to ensure that society is safe from the effects of radiation. The Authority works to achieve radiation safety in a number of areas: nuclear power, medical care as well as commercial products and services. The Authority also works to achieve protection from natural radiation and to increase the level of radiation safety internationally.

The Swedish Radiation Safety Authority works proactively and preventively to protect people and the environment from the harmful effects of radiation, now and in the future. The Authority issues regulations and supervises compliance, while also supporting research, providing training and information, and issuing advice. Often, activities involving radiation require licences issued by the Authority. The Swedish Radiation Safety Authority maintains emergency preparedness around the clock with the aim of limiting the aftermath of radiation accidents and the unintentional spreading of radioactive substances. The Authority participates in international co-operation in order to promote radiation safety and finances projects aiming to raise the level of radiation safety in certain Eastern European countries.

The Authority reports to the Ministry of the Environment and has around 300 employees with competencies in the fields of engineering, natural and behavioural sciences, law, economics and communications. We have received quality, environmental and working environment certification.

**Strålsäkerhetsmyndigheten**  
**Swedish Radiation Safety Authority**

SE-171 16 Stockholm  
Solna strandväg 96

**Tel:** +46 8 799 40 00  
**Fax:** +46 8 799 40 10

**E-mail:** [registrator@ssm.se](mailto:registrator@ssm.se)  
**Web:** [stralsakerhetsmyndigheten.se](http://stralsakerhetsmyndigheten.se)